2021-09

Tomographic Approach to Human Hydration Assessment: Proof of Concept

Besler, Brendon Chisholm Brian

UNIVERSITY OF CALGARY

Tomographic Approach to Human Hydration Assessment:

Proof of Concept

by

Brendon Chisholm Brian Besler

A THESIS
SUBMITTED TO THE FACULTY OF GRADUATE STUDIES
IN PARTIAL FULFILLMENT OF THE REQUIREMENTS FOR THE
DEGREE OF MASTER OF SCIENCE

GRADUATE PROGRAM IN ELECTRICAL ENGINEERING

CALGARY, ALBERTA
SEPTEMBER, 2021

Abstract

Hydration is important to human health as water is a vital nutrient used in many physiological functions within the body. While there are many conventional hydration assessment techniques, there is no non-invasive clinical gold standard. This thesis provides a proof of concept for applying standard microwave tomography techniques to assess clinically relevant changes in hydration. A practical and effective tomographic system is designed in simulation for hydration assessment. To improve blind inversions of high contrast objects, a novel regularization parameter selection procedure is introduced. The tomographic hydration assessment technique is validated *in silico* using realistic forearm models and the effect of measurement noise and positioning is analyzed. Microwave hydration assessment is evaluated in a group of fasting volunteers. This thesis provides promising results for an emerging technique of hydration assessment based on the estimation of changes in permittivity and a practical application of microwave tomography.

Preface

Some of the work presented in this thesis has been published in conference proceedings. Portions of Chapter 3 appear in "Human Hydration Monitoring using Microwaves: System Assessment Using Fasting Volunteers," by BC Besler, DC Garrett, S Thorson, and EC Fear. BC Besler, DC Garrett, and S Thorson were involved in experimental work. BC Besler analyzed the bulk of the results and wrote the manuscript. Portions of Chapter 5 appear in "Tomographic Approach to Human Hydration Assessment: In Silico Proof-of-Concept" by BC Besler and EC Fear. BC Besler performed the experiments and wrote the manuscript.

Acknowledgements

First, I would like to thank my supervisor Prof. Elise Fear for her guidance and support in completing this project. Her keen interest in her students' projects, determined mentorship, and technical skills enabled this project in so many ways.

I have been fortunate to work with many great people at the Applied Electromagnetics Group. Specifically, I would like to thank Jeremie Bourqui, Katrin Smith, Shengkai Gao, Felix Daou, Ishani DasGupta, Anita Garland, and Carina Butterworth for their discussions and help along the way.

I would like to thank David Garrett for his work organizing the Ramadan study. I would also like to thank Sarah Thorson and Danielle Deustcher for their help running the study and the University of Calgary Muslim Students' Association and all the volunteers for their participation.

NSERC and Alberta Innovates are thanked for providing funding during my degree.

I am also thankful for my family. My parents, Brian and Nora, have encouraged and enabled my educational pursuits since I was young. My brothers Bryce and Laidan were a source of welcome distractions.

Finally, I would like to thank Charlotte Rush for her constant support and understanding especially during these crazy times. It was a joy to complete much of this work while in lockdown with her.

Table of Contents

Abstract ii

Preface iii

Acknowledgements iv

Table of Contents v

List of Figures and Illustrations viii

List of Tables xi

List of Symbols, Abbreviations and Nomenclature xii

1 Introduction 1
- 1.1 Motivation . . . 1
- 1.2 Objectives . . . 2
- 1.3 Thesis Outline . . . 3

2 Human Hydration Assessment: Clinical Relevance and Microwave Techniques 4
- 2.1 Chapter Introduction . . . 4
- 2.2 Overview of Hydration . . . 5
- 2.3 Conventional Hydration Assessment Methods . . . 6
- 2.4 Electromagnetic Approaches to Hydration Assessment . . . 7
  - 2.4.1 Bioimpedance Analysis . . . 7
  - 2.4.2 Radio Frequency Techniques . . . 8
  - 2.4.3 Time Delay Spectroscopy . . . 9
- 2.5 Microwave Tomography . . . 10
  - 2.5.1 Imaging Extremities . . . 11
- 2.6 Chapter Conclusion . . . 13

3 Pilot Study with Fasting Volunteers 14
- 3.1 Chapter Introduction . . . 14
- 3.2 Ramadan Fast and Hydration . . . 15
- 3.3 Study Design . . . 16

3.3.1 Time Delay Spectroscopy . . . 16
3.3.2 Study Protocol . . . 17
3.4 Results . . . 19
3.4.1 Connection Issue . . . 19
3.4.2 Change in Hydration . . . 21
3.5 Discussion . . . 27
3.6 Chapter Conclusion . . . 28

4 Two-Dimensional Microwave Scattering in Biomedical Applications 30
4.1 Chapter Introduction . . . 30
4.2 Forward Problem . . . 31
4.2.1 Incident Fields . . . 33
4.2.2 Total Fields . . . 34
4.2.3 Validation . . . 38
4.3 Inverse Problem . . . 43
4.3.1 Singular Value Decomposition . . . 46
4.3.2 Direct Inversion and Singular Values . . . 47
4.4 Chapter Conclusion . . . 49

5 Microwave Tomography for Hydration Assessment 50
5.1 Chapter Introduction . . . 50
5.2 Non-linear Inversion . . . 51
5.2.1 Distorted Born Iterative Method . . . 51
5.2.2 Change Detection . . . 55
5.3 Regularization . . . 56
5.3.1 Tikhonov Regularization . . . 57
5.3.2 Tikhonov Regularization and Non-linear Inversion . . . 58
5.3.3 L-Curve . . . 59
5.3.4 Proposed Regularization Scheme . . . 60
5.3.5 Validating Non-Linear Inversion . . . 62
5.4 Forearm Models . . . 65
5.5 System Design . . . 66
5.5.1 System Setup . . . 66
5.5.2 Permittivity Metrics . . . 68
5.5.3 System Optimization . . . 68
5.6 Chapter Conclusion . . . 82

6 In Silico Validation of Tomographic Hydration Assessment 83
6.1 Hydration Model . . . 83
6.2 Change Detection . . . 86
6.2.1 Noiseless Measurements . . . 88
6.2.2 Noise Analysis . . . 90
6.2.3 Position Analysis . . . 93
6.3 Conclusion . . . 97

7 Conclusion **99**
7.1 Contributions 100
7.2 Limitations and Future Work 101

Bibliography **104**

A Fast Fourier Transform - Conjugate Gradient Method **121**

B Scattered Field from a Dielectric Cylinder **124**

C Forearm Image Segmentation **127**

List of Figures and Illustrations

2.1 Dielectric properties of select tissues in microwave frequency range. Data from [25]. 9

3.1 Time delay spectroscopy measurement setup. From [7]. 17
3.2 Measured signals for Volunteer A on fasting day 1. 20
3.3 Measured S_{21} signals through water with and without connection issue. . . . 21
3.4 Measured S_{11} signals with various connection qualities. 22
3.5 Relative weight change in pilot study volunteers while fasting and at baseline. 22
3.6 Measured S_{21} signals for Volunteer B on fasting day 3. 24
3.7 Estimated permittivity for Volunteer B on fasting day 3. 25
3.8 Estimated permittivity of Volunteers B, C, G, and I while fasting (F) and not fasting (NF) on select measurement days. Bars indicate median measurement session value and error bars indicate minimum and maximum values. 25
3.9 Estimated change in permittivity versus change in weight of fasting and baseline volunteers. Dots are measurement session medians and error bars are minimum and maximum values. 26
3.10 Estimated change in permittivity over time of fasting and baseline volunteers. Dots are measurement session medians and error bars are minimum and maximum values. 27

4.1 Tomographic setup with 12 receivers and 12 transmitters showing imaging domain $\mathcal{D}$, simulation domain $\mathcal{B}$, and measurement surface $\mathcal{S}$ 32
4.2 Homogeneous cylinders used for analytic solutions. 39
4.3 Scattered fields from lossless homogeneous cylinder in free space. 40
4.4 Total fields inside lossless cylinder in free space. 40
4.5 Scattered fields from lossy homogeneous cylinder in background medium. . . 41
4.6 Total fields inside lossy homogeneous cylinder in background medium. 41
4.7 Scattered fields from PEC cylinder in background medium. 42
4.8 Total fields inside PEC cylinder in background medium. 42
4.9 Tomographic setup for imaging homogeneous elliptical cylinder. 47
4.10 Singular values for a homogeneous elliptical cylinder. 48
4.11 Results from inversion of homogeneous cylinder without regularization. . . . 49

5.1 Homogeneous elliptic cylinder in free space. 62
5.2 Reconstructed homogeneous elliptic cylinder. 63

5.3 L-curve and associated curvature for first iteration of homogeneous elliptic cylinder inversion. 64
5.4 Regularization parameters from L-Curve, decaying series, and hybrid method. 64
5.5 2D cross section of Duke and Ella forearm models. The blue, dark red, and yellow voxels represent veins, arteries, and interstitial fat, respectively. Images not to scale. 65
5.6 Duke forearm permittivity model in tomographic system with free space background. 67
5.7 Mean square error of Duke forearm reconstructions with various background media. 71
5.8 Histograms of mean square error for Duke forearm reconstructions with various background media. 71
5.9 Reconstructed forearm in optimum background medium using standard L-curve method. 72
5.10 Reconstructed forearm in optimum background medium using adaptive method. 73
5.11 Cross-section of reconstructed forearm permittivity in optimum background medium at 500 MHz compared to actual values. 73
5.12 Cross-section of reconstructed forearm conductivity in optimum background medium at 500 MHz compared to actual values. 74
5.13 MSE in reconstructed complex permittivity and relative residual error of scattered fields for Duke forearm in optimum medium vs frequency. 75
5.14 Reconstructed forearm properties for Duke model in optimum background medium at 1.2 GHz using standard L-curve technique. 76
5.15 Reconstructed forearm properties for Duke model in optimum background medium at 1.2 GHz using adaptive technique. 76
5.16 Cross-section of reconstructed forearm permittivity in optimum background medium at 1.2 GHz using adaptive technique compared to actual values. . . 77
5.17 Cross-section of reconstructed forearm conductivity in optimum background medium at 1.2 GHz using adaptive technique compared to actual values. . . 77
5.18 Mean square error in reconstructed complex permittivity and relative residual error of scattered fields for Duke forearm at 1.2 GHz using adaptive technique with different noise levels and number of receivers. Error bars denote the minimum and maximum values 79
5.19 Permittivity estimates ε_{avg} and $\varepsilon_{\text{bulk}}$ with different number of receivers and noise levels. Error bars denote minimum and maximum values. 80
5.20 Reconstructed Duke forearm model with optimized design and 5% noise. . . 81
5.21 Segmented image for Duke forearm in optimized design and 5% noise. 81

6.1 Forearm tissue properties. Literature values (solid) [122] and Debye fit (dashed). 85
6.2 Debye parameters as a linear function of water content with linear regression. 85
6.3 Permittivity of Duke forearm model at baseline and 2% dehydration. 87
6.4 Permittivity of Ella forearm model at baseline and 2% dehydration. 87
6.5 Estimated change in permittivity due to dehydration using blind inversions. Dashed lines represent linear regression and solid lines represent input model values. 89

6.6 Estimated change in permittivity due to dehydration using *a priori* inversions. Dashed lines represent linear regression and solid lines represent input model values. . . . 89
6.7 Estimated change in permittivity for Duke model undergoing 2% weight loss using blind inversions at various noise levels. Dots represent sample median, error bars represent minimum and maximum, and dotted lines are linear regressions. . . . 91
6.8 Estimated change in permittivity for Duke model undergoing 2% weight loss using *a priori* inversions at various noise levels. Dots represent sample median, error bars represent minimum and maximum, and dotted lines are linear regressions. . . . 91
6.9 Measured changes in permittivity at $\Delta W = 2\%$ at various noise levels using blind inversions. Dots represent samples, 'x' represents noiseless result, and squares represent sample median. . . . 92
6.10 Measured changes in permittivity at $\Delta W = 2\%$ at various noise levels using *a priori* inversions. Dots represent samples, 'x' represents noiseless result, and squares represent sample median. . . . 92
6.11 Duke forearm model displaced by 10 mm in x and y. . . . 94
6.12 Relative residual error at $\Delta W = 0, 0.5, 1.0, 1.5, 2.0$ with forearm at various locations. . . . 95
6.13 Absolute bulk permittivity estimates at $\Delta W = 0, 0.5, 1.0, 1.5, 2.0\%$ with forearm at various locations. . . . 95
6.14 Absolute average permittivity estimates at $\Delta W = 0, 0.5, 1.0, 1.5, 2.0\%$ with forearm at various locations. . . . 96
6.15 Estimated change in bulk permittivity at $\Delta W = 2.0\%$ with errors in baseline and difference forearm locations. . . . 96
6.16 Estimated change in average permittivity at $\Delta W = 2.0\%$ with errors in baseline and difference forearm locations. . . . 97

C.1 Reconstructed Duke forearm model with optimized design and 10% noise. . . . 128
C.2 Segmented image for Duke forearm in optimized design and 10% noise. . . . 128
C.3 Reconstructed Duke forearm model with $N_{rx} = 32$ and 5% noise. . . . 128
C.4 Segmented image for Duke forearm in $N_{rx} = 32$ and 5% noise. . . . 129

List of Tables

2.1 Nominal water content of select tissues. Data from [24]. 8

3.1 Summary of Volunteer Details for Fasting Study 18

4.1 Relative residual error for test objects. 40

5.1 Demographic information for realistic models. 65
5.2 Nominal dielectric properties for Duke model at 500 MHz. 66
5.3 Statistics on matching medium parameter sweep with Duke forearm. 72

6.1 Water content of forearm tissue [24], Debye parameters of fit and mean sum squared error between Debye and Cole-Cole models. 85
6.2 Slopes for linear fit of tissue Debye parameters vs water content and R^2 values. 86
6.3 Linear regression parameters for changes in permittivity due to dehydration for Duke and Ella models. 90
6.4 Measured noise levels from the literature. 90
6.5 Linear regression slopes for change in permittivity due to weight loss. 93

List of Symbols, Abbreviations and Nomenclature

Symbol	Definition
c_0	Speed of light in vacuum
k	Complex wavenumber
p	Empirical regularization constant
r	Pearson correlation coefficient
s_i	i^{th} singular value
ε	Dielectric permittivity
χ	Normalized dielectric contrast
σ	Dielectric conductivity
ω	Angular frequency
$G(\cdot)$	Green's function
$\|\cdot\|$	L-2 norm
R^2	Coefficient of determination
$\mathcal{S}$	Measurement surface
$\mathcal{B}$	Simulation domain
$\mathcal{D}$	Image domain
ΔW	Change in weight
U_{sg}	Urine specific gravity
$\boldsymbol{u}_i$	i^{th} left singular vector
$\boldsymbol{v}_i$	i^{th} right singular vector
$\hat{\boldsymbol{x}}$	Unit vector in x direction
$\boldsymbol{r}$	2-D spatial vector
$\boldsymbol{L}$	Regularization matrix
$\boldsymbol{M}$	Inverse matrix

Abbreviation	Definition
BIM	Born Iterative Method
CSI	Contrast Source Inversion
DBIM	Distorted Born Iterative Method
FDTD	Finite-Difference Time-Domain
FEM	Finite Element Method
FFT-CGM	Fast Fourier Transform - Conjguate Gradient Method
GN	Gauss-Newton
LM	Levenberg-Marquardt
MoM	Method of Moments
MSE	Mean square error
MWT	Microwave tomography
OUT	Object under test
PEC	Perfect electric conductor
RRE	Relative residual error
SVD	Singular value decomposition
TBW	Total body water
TDS	Time delay spectroscopy
THA	Tomographic hydration assessment
TM	Transverse magnetic
VNA	Vector network analyzer

Chapter 1

Introduction

1.1 Motivation

Water is a vital nutrient used in many physiological functions within the body. As such hydration is an important aspect of human health with water loss as little as 2% of body weight impacting cognition and athletic performance [1, 2]. Thirst is often not adequate for maintaining hydration as it develops after dehydration has occurred and is satiated before hydration is restored [3]. While healthy adults can typically maintain hydration by drinking water at the onset of symptoms, certain at-risk populations such as athletes and older persons may experience dehydration more frequently [4]. Older persons experience a decrease in the thirst response [5] which may lead to chronic dehydration that has been associated with negative health outcomes such as increased mortality [6]. Thus, hydration has important clinical implications necessitating its accurate and convenient assessment.

Recently at the University of Calgary, tissue permittivity has been proposed as new method for assessing changes in hydration [7, 8]. The physiological basis for this technique is the close relationship between tissue water content and dielectric properties [9]. This technique was validated through a theoretical model, simulations [7], and a pilot study of varsity athletes undergoing acute water loss during practice [8]. This initial validation relied

on a simple estimate of permittivity from the time of flight of microwave pulses that is susceptible to errors due to sensor placement and multipath [7].

To improve the sensitivity of microwave hydration assessment, microwave tomography (MWT) is investigated here. MWT uses models of electromagnetic scattering to provide quantitative images of the permittivity and conductivity of the object under test (OUT). Typical applications for MWT include imaging the breast [10] or extremities [11]. While MWT has been the subject of intense research, its clinical and commercial application has remained limited. Because hydration relates to the bulk properties of tissues, microwave hydration assessment presents a simpler problem in which high resolution images are not required. This makes microwave hydration assessment a promising application for the practical use of MWT technology. As an initial proof of concept, this work focuses on applying standard tomographic approaches to realistic forearm models in simulation.

1.2 Objectives

The goal for this work is to assess the feasibility of using conventional microwave tomography techniques to monitor clinically relevant changes in hydration. As a preliminary step, a study is conducted using microwave hydration assessment techniques to develop a better understanding of the limitations of the method. The rest of this work focuses on the analysis of a practical MWT approach to assessing human hydration. In pursuit of this goal the following objectives are set out:

1. **Evaluate the efficacy of microwave hydration assessment techniques in a sedentary population.** A previously developed microwave hydration assessment technique is evaluated on a group of fasting volunteers to characterize the technique on subjects undergoing subtle dehydration.

2. **Develop a robust method of regularization without the need for *a priori* information.** A simple method of selecting the regularization parameter combining a

well-known heuristic approach with an adaptive empirical method is developed. This technique allows blind inversions of high contrast objects.

3. **Design a tomographic system for microwave hydration assessment in simulation.** A systematic analysis of the key design parameters for a tomographic system is performed to develop a system optimized for hydration assessment. This *in silico* analysis yields a system that is readily implemented in practice.

4. **Validate microwave tomography for hydration assessment *in silico*.** The tomography hydration assessment technique is validated with various realistic forearm models and the effect of measurement noise and positioning errors are analyzed.

1.3 Thesis Outline

In Chapter 2, a brief overview of hydration, conventional and emerging hydration assessment techniques, as well as MWT for permittivity estimation is presented. Next, in Chapter 3 a previously developed microwave hydration assessment technique is applied in a study of fasting volunteers and results are presented. This study motivates the improvement of the microwave hydration technique by applying MWT. In Chapter 4, the forward and inverse microwave scattering problems are explored as the basis for MWT. Next, in Chapter 5 the tomographic hydration assessment technique is presented using standard non-linear inversion with Tikhonov regularization for change detection. A novel method for selecting the regularization parameter and a systematic design of the tomography system is developed. Finally, the tomographic hydration assessment technique is validated in Chapter 6 using clinically relevant changes in hydration and the effect of measurement noise and position errors is analyzed.

Chapter 2

Human Hydration Assessment: Clinical Relevance and Microwave Techniques

2.1 Chapter Introduction

In this chapter an overview of hydration, its assessment, and emerging electromagnetic assessment techniques are provided. The lack of a clinical gold standard for non-invasive hydration assessment among conventional techniques has motivated the development of novel methods. Electromagnetic approaches have been proposed as an alternative due to their non-invasive nature, low cost, and sensitivity to water content, however previous methods have often failed to use physiologically meaningful parameters [4]. Recent work [7, 8] has shown that changes in tissue permittivity have the potential to be an accurate and sensitive measure of changes in hydration. MWT as a biomedical imaging modality used to estimate the dielectric properties of objects is introduced and its application to hydration assessment is discussed. The techniques applied for tomographic hydration assessment (THA) will be discussed in more detail in the methods chapters.

2.2 Overview of Hydration

Hydration is an important aspect of human health as water is a vital nutrient used in many physiological functions including nutrient and waste transportation, temperature regulation, and metabolic functions among others [12]. Hydration is defined in terms of the total body water (TBW) found in both intracellular and extracellular fluids. Water comprises 50-70% of the human body by weight, varying with age and gender. The human body typically maintains a state of euhydration, water balance or normal TBW, within 0.2 % of body weight on a day-to-day basis [12]. Dehydration, or hypohydration, is thus defined as the state of TBW less than the normal baseline value. The severity of dehydration is often defined in terms of TBW with decreases of 3-5% of body weight indicating severe dehydration, however mild dehydration can occur with a little as 1-2% [13].

Severe dehydration can lead to a myriad of symptoms including sunken features, delirium, muscle spasms, and difficulty swallowing [13]. Mild dehydration can result in fatigue, headaches, and heat intolerance among other symptoms [13]. With water loss $< 2\%$ body weight there is evidence of decrease cognitive function and changes in mood [1].

Typically, dehydration can be easily remedied by drinking fluids at the onset of symptoms, however, a number of at-risk populations have been identified [4]. During strenuous exercise athletes, military personnel, and workers lose body water via sweat and evaporation through the skin, increasing the risk of dehydration. Dehydrated athletes are at risk of exertional heat stroke, increased cardiac strain, and fatigue [4]. Older persons have lower baseline TBW and experience a general decrease in the thirst response which can lead to chronic states of mild dehydration [5]. In 2010, over 100,000 older adults were admitted to hospital in the United States with dehydration as the primary reason [14]. In one study from the United Kingdom analyzing at hospital admissions from 2011-2013, older adults admitted to hospital with dehydration as the primary cause had a 17% 30-day mortality compared to a 7% rate with those admitted without dehydration [6].

Effective hydration assessment techniques should have high enough sensitivity to detect

changes in TBW of at minimum 3% [4] as this is when measurable performance impacts occur in healthy adults. However, if the target population is certain at-risk populations such as older adults this sensitivity may need to be improved [4].

2.3 Conventional Hydration Assessment Methods

An overview of the commonly used hydration assessment techniques will be provided here. For a more comprehensive look at hydration assessment technology see [4, 15].

Thirst is the simplest clinical manifestation of dehydration, however it can be inadequate for detecting mild dehydration. The thirst response can be triggered after clinically relevant changes in hydration have occurred and can be satiated before hydration is restored [3]. This is especially true in athletes while exercising [16] and older adults [5].

Weight change can be an accurate estimate of changes in total body water for short time periods provided the measurements are controlled for spurious weight from personal effects, and weight changes due to eating, drinking, and voiding [17]. The physiological basis for this technique is simply that the body is predominately composed of water and most short-term changes in weight can be attributed to changes in body water content. For example, in [18], a day-to-day change in weight of 2.5% indicated a 95% probability of dehydration.

Urine concentration is another commonly used technique. The simplest method for assessing urine concentration is by color with paler colors indicating euhydration and darker yellow colors indicating dehydration. A scale has been developed to standardize urine color determinations [19]. Urine concentration can also be estimated using handheld refractometers to determine the urine specific gravity, U_{sg}. Specific gravity is a measure of the density of a fluid with 1.0 being the density of water and values > 1 being denser than water. Generally, a $U_{sg} > 1.02$ is used as the threshold for dehydration [15, 20]. An important aspect of urine concentration is that while the bladder is emptied intermittently, the bladder is filled continuously throughout the day. This means that urine concentration provides as estimate

of the hydration levels since the last voiding [15]. The first morning urine is considered the most accurate [21].

Blood indices provide another technique of determining hydration status. Plasma osmolality is the current clinical standard for hydration assessment [4]. Osmolality is a measurement of the osmoles of solute per unit volume. When dehydration occurs, the plasma osmolality increases. Plasma osmolality plays a key role in the maintenance of euhydration as it governs the release of antidiuretic hormone [18]. While an accurate measure of hydration, this technique is inherently invasive and requires laboratory analysis increasing the cost and limiting the applicability to frequent monitoring of hydration. Another common blood metric is the hematocrit (concentration of red blood cells) level. This technique requires a smaller sample and less expensive analysis, making it more applicable to long term monitoring than plasma osmolality [4]. There is some evidence that blood biomarkers are less sensitive to changes in hydration than other methods such as urine indices [22].

2.4 Electromagnetic Approaches to Hydration Assessment

The limitations and drawbacks of conventional hydration assessment techniques has motivated the search for alternative methods. A wide array of methods including optical, electromagnetic, chemical and acoustic have been proposed to varying degrees of success [7]. An overview of proposed electromagnetic techniques will be provided here as this is the focus of this work, but an in-depth discussion of other emerging techniques can be found in [4].

2.4.1 Bioimpedance Analysis

Bioimpedance analysis uses alternating current applied to the body using electrodes to measure electrical impedance [17]. The technique can provide an indication of TBW but is generally considered a poor indicator of hydration status [20]. Bioimpedance analysis mea-

surements are sensitive to electrode placement, sweat, skin temperature, and posture [18] thus its applicability outside the laboratory setting is limited.

2.4.2 Radio Frequency Techniques

Numerous radio frequency (RF) techniques have been proposed for measuring hydration. These techniques utilize the dielectric properties of tissues due to water content to estimate hydration related parameters.

The dielectric properties of biological tissues in the radio and microwave frequency range are predominantly determined by their water content [9]. Fig. 2.1 shows the measured relative permittivity for common tissues [23] in the microwave frequency range and Table 2.1. shows the associated water content [24].

Table 2.1: Nominal water content of select tissues. Data from [24].

Tissue	Water Content [%]
Blood	80.0
Muscle	74.1
Skin	65.3
Bone (Cortical)	23.0
Bone (Cancellous)	15.0
Fat	21.2

In [26] the resonant cavity perturbation technique is proposed as a method of measuring TBW. In this method a room-sized metallic chamber is used to set up resonant modes. The subject then lies down inside the chamber and the resonant modes, due to the dielectric properties of the body, shift slightly. While this method has been validated *in vivo* [27], it requires a large room, specialized training, and is sensitive to body positioning and size.

In [28] the attenuation of RF signals through the forearm is used to estimate the change in hydration before and after a session of physical exercise. While an empirical model was fit to correlate the frequency dependent attenuation and changes in weight due to water

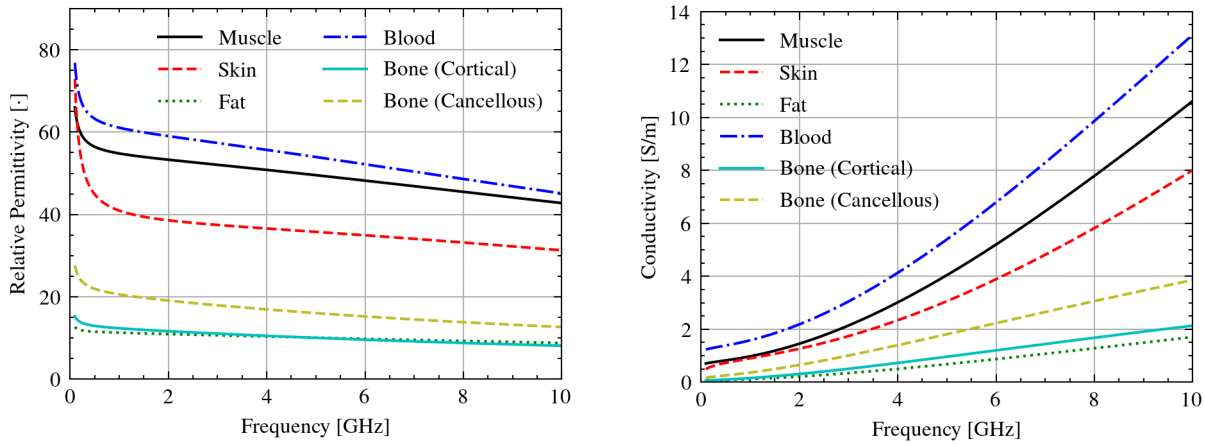

Figure 2.1: Dielectric properties of select tissues in microwave frequency range. Data from [25].

loss, a physiological interpretation of the model is not provided and application to other populations not tested.

In a similar vein, in [29] a patch antenna is used to measure changes in hydration related to the properties of the skin. This technique was validated using skin-mimicking phantoms manufactured to imitate different hydration levels. The patch is designed to operate in contact with the skin and the resonance frequency is then sensitive to the properties of the skin.

2.4.3 Time Delay Spectroscopy

In [7], the author proposes the use of bulk permittivity estimates for hydration assessment. A linear model for changes in the Debye parameters of tissue as a function of tissue water content is generated. Applying this model with clinically relevant changes in hydration to realistic forearm models, it is shown that the forearm permittivity is twice as sensitive to changes in hydration than the tissue conductivity. The details of this theoretical model will be discussed in Chapter 5 as part of the *in silico* validation used in this work.

In [7], the time delay spectroscopy (TDS) method is applied on the realistic forearm models. In TDS, the time delay of a microwave pulse travelling through the tissue is used

to estimate the relative permittivity. The theoretical model showed good agreement with simulation results. This technique was then validated *in vivo* using a group of wrestlers undergoing water loss during practice [8]. The technique showed a strong relationship between the weight changes before and after practice and the estimated change in permittivity.

While this technique shows potential, there are a number of practical drawbacks. First, the technique as implemented relies on ultrawideband pulses in the 2 - 10 GHz range. This places large demands on the measurement devices and sensor designs. Second, the technique is sensitive to the placement of the antennas as poor contact significantly impacts the pulse propagation and resulting permittivity estimation. Third, as the technique relies on a simple model of plane wave propagation, any deviation can severely impact the permittivity estimate. In the wrestler study, subjects with large forearms were removed from the analysis due to large multipaths through the forearm [7]. Further limitations will be discussed in Chapter 3 as part of a follow-up study.

2.5 Microwave Tomography

MWT is an imaging technique based on microwave scattering in which the dielectric properties of the OUT are estimated. Applying the physics of microwave scattering, the dielectric properties of objects can be reconstructed quantitatively. The technique has been the subject of intense research for over 30 years as the computing technology and microwave hardware required to accurately solve the inverse scattering problem has become more accessible. A large class of problems such as ground penetrating radar [30], microwave breast imaging [31], and non-destructive testing [32] can be formulated as a microwave inverse scattering problem. These problems are of great practical importance as MWT provides a method to interrogate the extent and/or properties of optically opaque objects without costly or impractical excision. However, the technique has had little commercial or clinical application in the medical field as it suffers from relatively low resolution, demanding hardware

requirements, and complicated formulations [33].

While there are many technical challenges with MWT, the technique has the potential to fill important niches in the medical imaging field [11]. Compared to x-ray techniques, MWT has the benefit of non-ionizing radiation, enabling its use for long term or frequent monitoring. MWT systems have the potential to image soft tissues with much less cost than magnetic resonance imaging, though at much lower resolution. Since water content is the main contrast mechanism in biomedical applications of MWT, it also has the potential to better differentiate certain soft tissue than ultrasound technology.

MWT technology has been suggested for a wide variety of biomedical applications such as imaging the breast [10], brain [34], bones [35], and heart [36]. Typically, these applications require maximizing the image resolution. The pursuit of maximizing image resolution places large demands on the measurement hardware and computational requirements that preclude simple solutions. In comparison to the typical application of MWT, hydration assessment involves estimating the bulk properties of tissues. This relaxes the need for high resolution imaging which can simplify both the measurement hardware and the computational requirements.

In a typical microwave tomography setup, the OUT is surrounded by sensors which transmit fields to interrogate the OUT. Often a matching medium is used to better transmit fields into the OUT. By recording the scattered fields from the object and applying a model of microwave scattering, the unknown properties can be recovered. The details of the microwave scattering problem will be discussed in further detail in Chapter 4.

2.5.1 Imaging Extremities

The extremities provide a useful OUT as they can be easily accessed, surrounded by sensors, and immersed in matching fluid as needed. The extremities provide a high contrast object as the structure alternates from the high permittivity and conductivities of the skin, to the lower properties of subcutaneous adipose tissue, the high properties of the muscle, and

finally the low properties of the bones. This can make reconstructing the properties of the soft tissue more difficult [37]. The extremities also provide a useful OUT for testing MWT algorithms as the geometry and composition of the extremities is well known, i.e. there are bones, muscle, and skin and fat layers.

In [38], a cylindrical MWT system is validated using a synthetic forearm model and an *in vivo* forearm measurement. The qualitative image formed accurately localized the subcutaneous fat layer, bones, and muscle region. This experimental forearm data was used to validate non-linear algorithms in [39, 40, 41]

A number of authors have used synthetic extremities to test microwave tomography algorithms *in silico*. Initially these tests were generally restricted to crude forearm models with realistic properties assigned, e.g. [42]. More recently, realistic extremity models have been applied to validate non-linear inversion techniques such as a synthetic leg model in [43].

MWT extremity imaging has been proposed as a method to monitor the soft tissue damage accompanying fractures and to measure pressure build up in the extremities called compartment syndrome [37, 44, 36]. In [37] the authors image excised porcine legs and explore the effect of reduced blood flow on MWT images.

In [11], a system consisting of 24 dipoles operating around 1 GHz is used to image the forearm of five volunteers. No immediate application for the forearm imaging technique is given, but the authors suggest that it could be used to monitor soft tissue damage. In all images the forearm outline was accurately retrieved however the bones were not localized for cases with larger subcutaneous fat layers. They then use an *ad hoc* method to estimate the subcutaneous fat layer to segment the forearm into a subcutaneous fat layer and muscle interior to improve the reconstructions.

2.6 Chapter Conclusion

Hydration is important to human health with severe dehydration causing serious health concerns and mild dehydration impacting athletic performance and cognition. While there are many conventional techniques for measuring changes in hydration, there is currently no clinical gold standard of non-invasive hydration assessment. This motivates the development of alternative techniques that can be used to accurately monitor hydration and better enable intervention before serious health or performance impacts occur. Among other emerging techniques, electromagnetic methods have been proposed, the most promising of which are based on permittivity estimation.

MWT is a well-developed technique used for imaging the dielectric properties of tissue. The technique has been applied for imaging many structures in the body with various degrees of success. MWT has been applied to successfully image the extremities by multiple authors. Applying MWT to imaging extremities should provide a robust and accurate method of detecting changes in permittivity due to changes in hydration.

Chapter 3

Pilot Study with Fasting Volunteers

3.1 Chapter Introduction

Microwave hydration assessment has previously been explored in models derived from the water content of tissues [7] and a group of wrestlers undergoing acute water loss during practice [8]. While the correlation between the weight loss and change in permittivity before and after practice provided promising results for microwave hydration assessment technology, this acute change in body water content may not be representative of the longer-term changes in hydration that occur in more sedentary populations. The long term hypohydration that can occur with certain at-risk population such as older adults or those with pre-existing conditions can have significant impact on clinical outcomes such as increased mortality [6].

To further examine the microwave hydration assessment technique, it is applied to a group of fasting volunteers. The aim of this chapter is to explore whether the previously developed microwave frequency approach is capable of detecting subtle changes in dehydration occurring throughout the day. This chapter will introduce the previously designed microwave hydration assessment technique using TDS, outline the present study procedure, and provide the study results.

3.2 Ramadan Fast and Hydration

Ramadan is an Islamic holy month in which observers fast for a period of 29 - 30 days. A typical Ramadan fast includes abstaining from food and drink from sunrise to sunset. In addition to forgoing food and drink, participants may give up caffeine and tobacco as part of their fast. Because Ramadan occurs 11 days earlier than the previous year [45] it can occur in any season. In Canada, this means that when Ramadan falls in the summer months there is a markedly warmer climate, and the days are much longer than when Ramadan occurs in the winter months.

The effects of the Ramadan fast on body composition and hydration can be highly variable depending on environmental factors, subject's level of exertion, and ability to replenish liquids and energy each day [46, 47]. Because of the wide variation in fasting conditions, the intermittent hypohydration occurring before the fast is broken each day and the possible chronic dehydration that could occur over the month of fasting are difficult to discuss in general [46].

Athletes have been a common population for studies of hydration during Ramadan [48, 47, 49, 50, 51]. These studies use body mass, urine concentration, and blood biomarkers to estimate changes in hydration relevant to athletic performance. Due to the variations in fasting conditions and methodological differences, these studies provide inconclusive results on the extent of intraday dehydration occurring and whether dehydration occurs throughout Ramadan [48]. However, athletes are at risk of acute dehydration of over 3% total body water during the day, especially in warmer climates [52].

Ramadan hydration studies have also focused on at-risk populations such as those with chronic kidney disease [53] or workers in warm climates [54, 55]. These studies use changes in weight, urine concentration, and blood components to estimate changes in hydration status.

Investigations of hydration during Ramadan for sedentary healthy adults has been more limited. These studies have used weight changes, urine concentration, and blood indices to analyze the hydration of disparate populations [46, 56, 57]. However, it is generally accepted

that healthy, sedentary adults are able to fully replenish water losses each night and are not at risk of long term dehydration through Ramadan [51, 46].

It is estimated that fasting individuals experience 800 mL of net total body water loss over 12 hours [47]. These losses include daily respiratory water loss, evaporation through the skin, amounts voided through urine and feces, and considers the amount produced in the body through metabolic processes. For an 80 kg male, this would translate to 1% of body mass and about 2% of total body water content. This amount will increase based on level of exercise and environmental factors such as heat and humidity.

3.3 Study Design

The study design will be presented as follows: the measurement system is described, then the TDS technique is introduced as a simple method of tracking changes in permittivity. This is followed by details on volunteer recruitment and finally the measurement schedule is discussed.

3.3.1 Time Delay Spectroscopy

A measurement setup, as seen in Fig. 3.1, consisting of two ultrawideband antennas, a forearm holder, and vector network analyzer (VNA) was previously developed [8]. The ultrawideband antennas, dubbed Nahannis, are dielectric loaded with a high permittivity ceramic to enable operation in direct contact with skin [58]. The antenna pair is positioned at the midpoint of the forearm and placed in contact with the skin. The antennas radiate from 1.8 - 20 GHz, however signals above 7 GHz are attenuated beyond the dynamic range of the measurement device due to the properties of the forearm. Both antennas are connected to a VNA (Agilent N5230-A PNA-L) to record the complex scattering parameters from 10 MHz to 10 GHz in 10 MHz increments. An intermediate frequency bandwidth of 100 Hz and signal strength of 0 dBm is used. The separation distance between the antennas is recorded

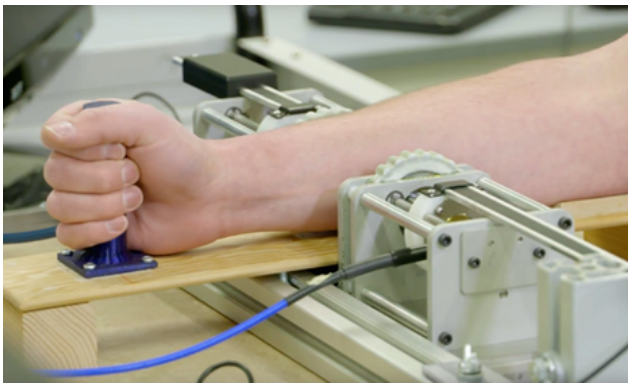

Figure 3.1: Time delay spectroscopy measurement setup. From [7].

using a digital caliper to 0.1 mm accuracy.

The TDS technique is applied to estimate changes in bulk permittivity due to changes in hydration. The measured transmission (S_{21}) signals are transformed from the frequency domain into the time domain using the inverse chirp-z transform [59]. The time domain signal is generated with a time step of 2 ps. The time of arrival is determined from the maximum of the pulse envelope. Using the measured separation distance, d, time of arrival with the forearm in place, t_1, and the arrival time through free space, t_2, the relative permittivity of the forearm can be found from eq. (3.1) [60].

$$\varepsilon_r = \left(1 + \frac{(t_1 - t_2)c_0}{d}\right)^2 \tag{3.1}$$

where c_0 is the speed of light in free space.

3.3.2 Study Protocol

Volunteers were measured on three days while fasting during Ramadan and three days after Ramadan while not fasting. After Ramadan, participants ate and drank *ad libitum* with no special instructions. Each measurement day consisted of three measurement sessions: morning, afternoon, and evening. Five microwave measurements were taken at the forearm midpoint during each measurement session. The midpoint of the forearm was determined by measuring the distance from the ulnar head and lateral condyle of the humerus. The fore-

arm was removed from the setup and antenna repositioned to the same separation distance between each measurement. The measurements without the arm, dubbed the antenna only, were taken once a day.

Ten volunteers were recruited (eight male, two female). Volunteers were recruited through the University of Calgary Muslim Students' Association. This study was approved by the University of Calgary Conjoint Health Research Ethics Board (CHREB ID: REB18-0700). Table 3.1 provides the demographics details for the recruited population. The study was undertaken during Ramadan 2018 which began on the evening of May 15 and finished on the evening of June 15. In 2018, Ramadan fasting in Calgary was approximately 18 to 19 hours long. Volunteers were predominately university students.

Table 3.1: Summary of Volunteer Details for Fasting Study

Demographic Details	
Height, cm	178.0 (157.8 - 194.3)
Weight on first fasting measurement day, kg	74.9 (61.2 - 108.9)
Weight on first baseline measurement day, kg	76.7 (59.2 - 109.3)
Forearm circumference, cm	22.4 (20.0 - 25.1)
Protocol Details	
Fasting intraday weight change, %	-0.95 (-2.37 - -0.27)
Baseline intraday weight change, %	0.21 (-0.74 - 1.20)
Fasting U_{sg},	1.022 (1.009 - 1.034)
Baseline U_{sg},	1.017 (1.003 - 1.030)
Antenna separation distance, mm	55.1 (46.4 - 61.5)

In addition to microwave measurements, weight and urine specific gravity were measured. Weight was measured using a conventional scale with volunteers' pockets emptied of personal effects. Urine specific gravity was measured with a handheld light refractometer (Atago PAL-10S). Measurement days and sessions were scheduled according to volunteer availability. Measurement days were selected throughout the Ramadan fast. The earliest measurement sessions were scheduled for 8:30 and the latest at 19:00, however most measurements were done between the late morning (10:00 - 12:00) and late afternoon (15:00 - 17:00). While

fasting, volunteers' last food and drink was in the very early morning (i.e. 4:00) so all food and drink would have been absorbed before the first measurement. The absorption rate of pure water is about 300 mL in 90 minutes [61] and the majority of solid foods are emptied from the stomach into the small intestine within 2 hours [62] where fluids are absorbed within 5 minutes [61].

While the long term, interday changes during the Ramadan fast are important for assessing potential health impacts, the analysis here is restricted to intraday changes. It is assumed that the volunteers reach euhydration each night and are dehydrating throughout the day which generally agrees with the literature [46, 47].

3.4 Results

3.4.1 Connection Issue

After completion of the study, it was found that one of the connectors on the measurement device was loose. This connector came loose after repeated strains due to repositioning the antennas. The connection issue led to a noticeable bias in the frequency domain measurements. Specifically, the reflection, $S_{11}(f)$, at the affected antenna is quite different indicating a large change in the impedance match between the cable and antenna. This lead to a noticeable change in the characteristic response of the transmission data, $S_{21}(f)$. Fig. 3.2 shows the measured $S_{11}(f)$ and $S_{21}(f)$ signals for Volunteer A on the first measurement day during Ramadan. The connection issue is most noticeable between the S_{11} signals for morning and evening. The morning signal has $S_{11} \approx -10$ dB for $f > 2$ GHz indicating a good match whereas the evening signal generally has $S_{11}(f)$ 5 dB higher indicating a significant change in impedance. This leads to a small, but noticeable, change on $|S_{21}(f)|$ around 2 GHz. By comparing this change to the expected change from [8], this small change has the potential to overshadow the changes associated with hydration.

To better understand the errors introduced by the poor connection, measurements of

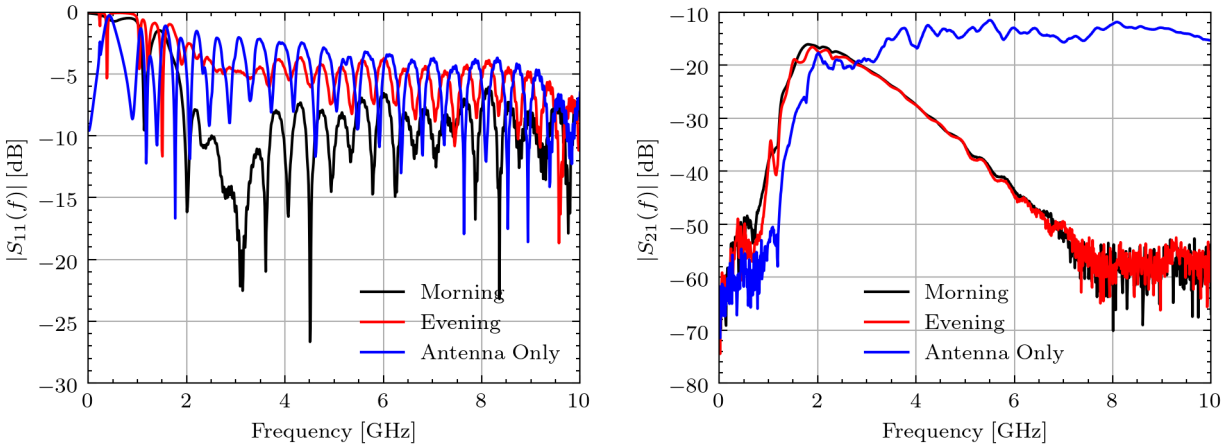

(a) (b)

Figure 3.2: Measured signals for Volunteer A on fasting day 1.

known materials (water and glycerin) were taken with the loose connection and tightened connection. The liquids were placed inside thin plastic bags and placed in contact with the sensors. In a similar manner to the study measurements, 5 measurements were taken with the object under test removed from the setup and repositioned between each measurement. Unlike the actual measurements the antennas were not moved after each measurement. Fig. 3.3 shows a representative phase response and time domain signal through water with good and bad connections. As can be seen, the effect on the phase is minimal. The time domain pulses show similar arrival time but lower magnitude with the connection issue. Applying TDS to the signals yields 1.6% and 2.5% differences between the permittivity with good and bad connections for water and glycerin, respectively. While this error introduced by the connection issue is small, it is on the same order of magnitude as the expected permittivity changes of 2% [8].

To control for the connection issue, only signals that have similar connection quality are compared on each day. To quantify the connection issue in the measurement data, the $S_{11}(f)$ signals below the radiation frequency, 1.2 GHz, can be used because the effect of the object under test will be minimal. Specifically, the correlation coefficient between the linear magnitude of two reflection signals $S_{11,i}(f)$ and $S_{11,j}(f)$ will be used. This can be defined

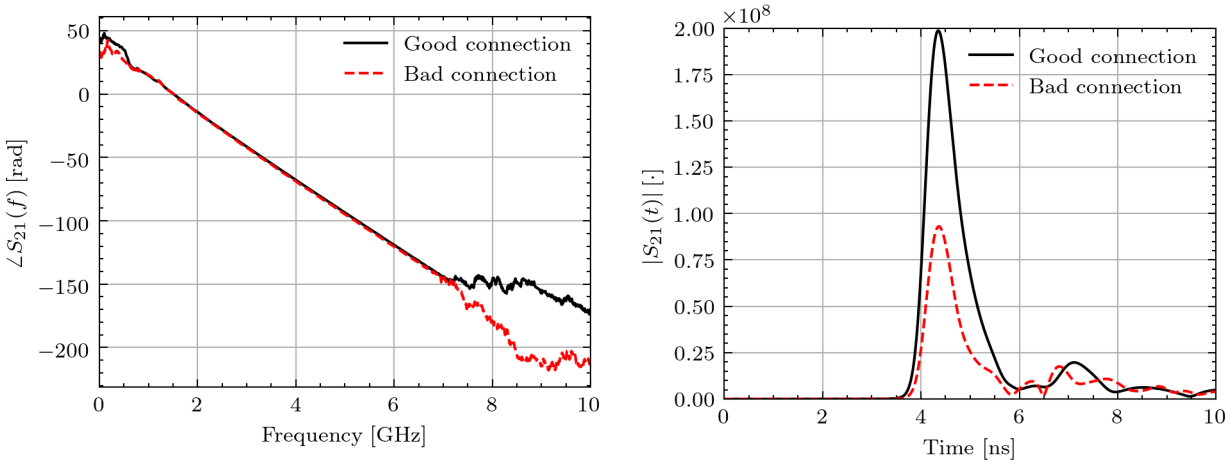

(a) (b)

Figure 3.3: Measured S_{21} signals through water with and without connection issue.

using the covariance and standard deviation of the signals as:

$$r_{i,j} = \frac{\text{cov}(|S_{11,i}(f)|, |S_{11,j}(f)|)}{\text{std}(|S_{11,i}(f)|) \cdot \text{std}(|S_{11,j}(f)|)}, \; f \leq 1.2 \text{ GHz} \tag{3.2}$$

Fig. 3.4 shows the measurements from the morning and evening sessions as well as the antenna only measurement for Volunteer A while fasting. These signals have various connection qualities with correlation coefficients between the morning and evening measurements $r_{\text{morn,eve}} = 0.45$ and between the morning and antenna only measurements of $r_{\text{morn,ant}} = 0.01$.

A correlation coefficient of $r = 0.8$ is defined as the threshold at which signals are of similar enough quality to compare to each other. This threshold was determined using the experimental data as adequately grouping signals with like $S_{11}(f)$.

3.4.2 Change in Hydration

Standard Methods

During Ramadan, all volunteers showed decreases in weight between each measurement session. The average weight loss across all volunteers was 0.10 kg/hour with the smallest intraday weight loss of 0.27% and largest of 2.4%. After Ramadan the weights fluctuated

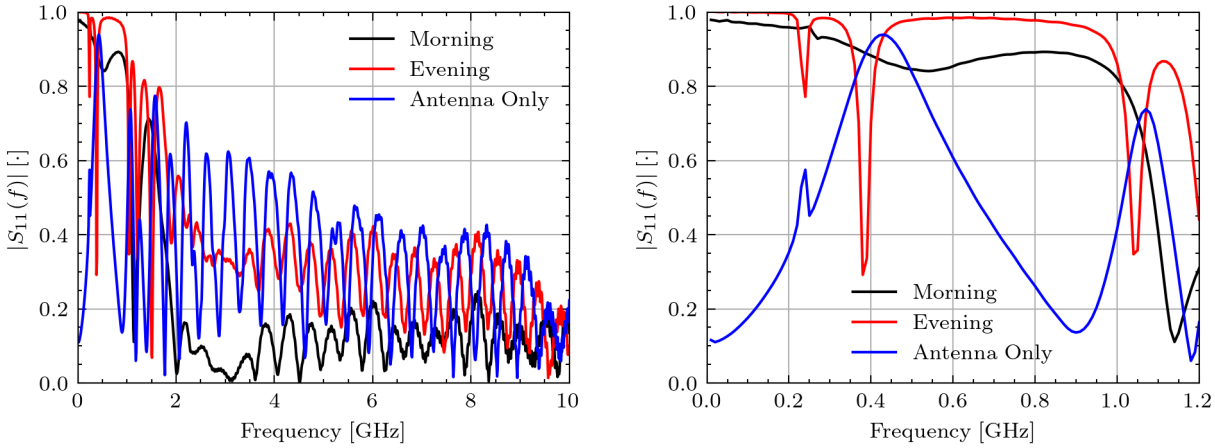

Figure 3.4: Measured S_{11} signals with various connection qualities.

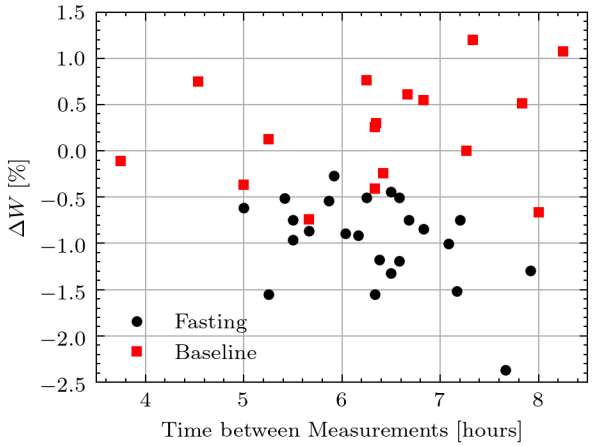

Figure 3.5: Relative weight change in pilot study volunteers while fasting and at baseline.

more as volunteers went about their typical days. The average weight change was 0.02 kg/hour with the largest intraday decrease of 0.74% and the largest intraday increase of 1.20%. The relative weight change normalized to the morning weight on each day is defined by eq. (3.3). Fig. 3.5 shows the relative weight changes while fasting and not fasting for all measurement days including those with bad measurements.

$$\Delta W = \frac{W_{\text{eve}} - W_{\text{morn}}}{W_{\text{morn}}} \cdot 100\% \tag{3.3}$$

where W_{eve}, W_{morn} are the weights in the evening and morning respectively.

The urine specific gravity was less reliable as an indicator of hydration status than changes in weight during Ramadan. The average specific gravity measured in the evening is 1.022 with the largest intraday decrease of 0.58%, average change of 0.25%, and largest increase of 1.3%. A decrease in urine specific gravity is related to an increase in hydration which is not possible while the volunteers are fasting. As discussed in Chapter 2, the urine specific gravity is not a reliable measure of hydration throughout the day. After Ramadan, the urine specific gravities are similar with the largest intraday decrease of 0.69%, average change of -0.24%, and largest increase of 0.20%. The average specific gravity measured in the evening was 1.017.

From the weight and urine specific gravity changes it can be seen that the changes in hydration are modest, therefore the permittivity will be compared between the morning and evening measurements to isolate the largest possible change. The change in permittivity is analyzed as a function of weight and as a function of time. Because weight change is an accurate measurement of changes in hydration if food, drink and voiding are accounted for it is expected that permittivity will decrease as weight decreases during Ramadan. Since no attempt is made to account for voiding, the changes in weight can be viewed as an upper limit on the changes in total body water. While the volunteers are fasting, it is assumed that they are undergoing some amount of dehydration so permittivity should decrease over time. After Ramadan it is assumed volunteers maintain a state of euhydration as they are able to eat and drink *ad libitum* so no correlation between permittivity and either weight or time is expected.

Change in Permittivity

The correlation coefficient threshold is applied using the morning measurement data. The correlation coefficient is applied between all 5 morning measurements and any signals with outlier connection quality ($r < 0.8$) are not analyzed further. The morning measurement with the highest correlation to the remaining signals is then used as the prototype signal

to compare to all others. Any antenna only or evening signals that are uncorrelated with the prototype signal are discarded. If more than 2 signals from any measurement set are uncorrelated the whole day is discarded. Before considering the connection issue, there were 24 complete measurement days before Ramadan and 18 complete measurement days after Ramadan. Applying the correlation coefficient threshold to control for the connection issue reduces the number to 15 measurement days during Ramadan and 16 afterwards.

To better contextualize the aggregate permittivity change data, select measurement sessions will be examined in more detail. Fig. 3.6 shows $|S_{21}(f)|$ and $S_{21}(t)$ for Volunteer B in the morning and evening while fasting. Fig. 3.7 shows the associated permittivity estimates. This data was collected with the connection issue as determined by the $S_{11}(f)$. The signals are consistent within and between each measurement session resulting in consistent permittivity estimates.

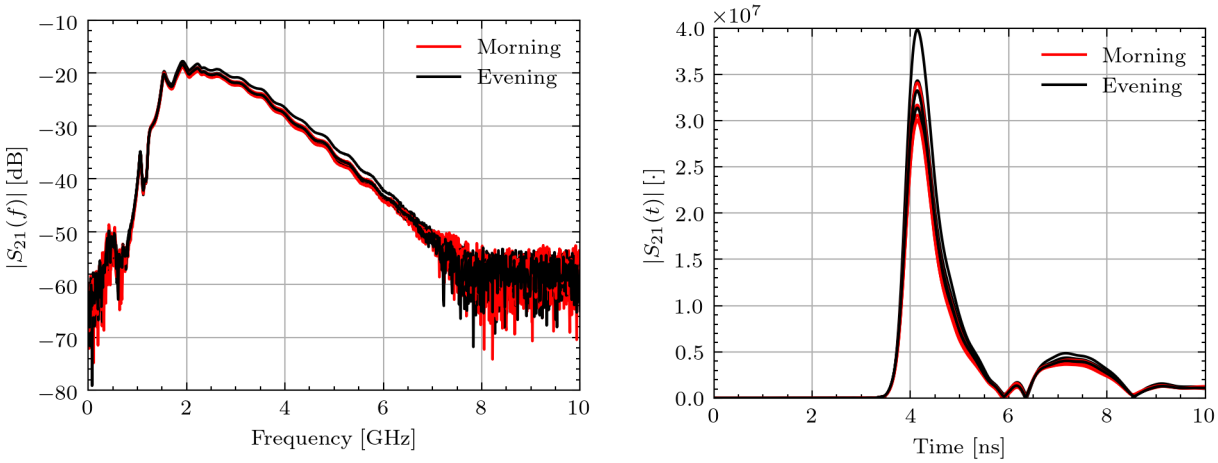

(a) (b)

Figure 3.6: Measured S_{21} signals for Volunteer B on fasting day 3.

Fig. 3.8 shows the absolute permittivity estimates for select volunteers (B, C, G, and I) in the morning and evening while fasting (F) and while not fasting (NF). The absolute permittivity estimates agree with the literature values [25] for muscle tissue and the wrestler study [8].

The relative change in permittivity is defined in a similar manner as eq. (3.3) using

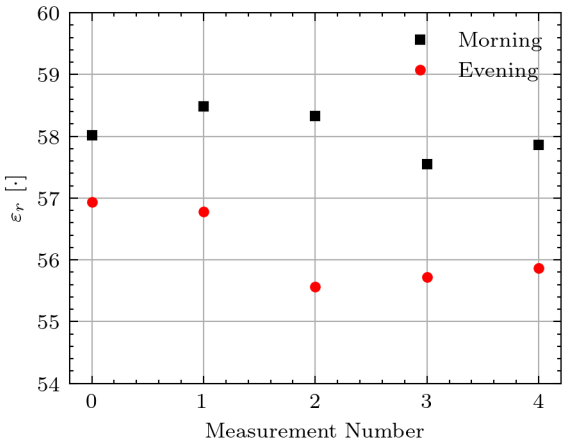

Figure 3.7: Estimated permittivity for Volunteer B on fasting day 3.

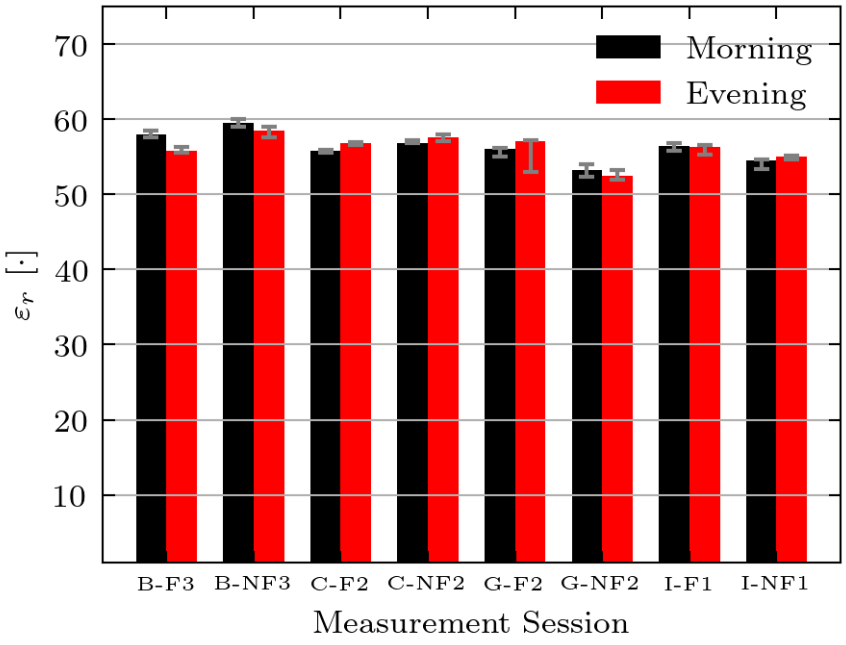

Figure 3.8: Estimated permittivity of Volunteers B, C, G, and I while fasting (F) and not fasting (NF) on select measurement days. Bars indicate median measurement session value and error bars indicate minimum and maximum values.

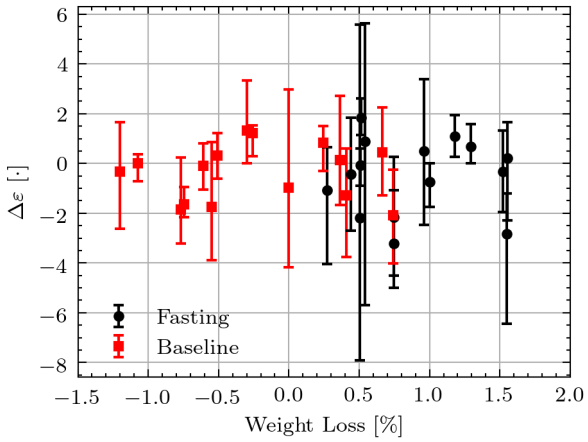

Figure 3.9: Estimated change in permittivity versus change in weight of fasting and baseline volunteers. Dots are measurement session medians and error bars are minimum and maximum values.

samples from the morning and evening. Every combination between the two sets of five samples from each measurement session are calculated and the minimum, maximum and median are reported.

Fig. 3.9 shows the change in permittivity as a function of changes in weight during Ramadan and after Ramadan. As can be seen there is no clear relationship between the changes in permittivity and changes in weight. Applying a linear regression to the fasting data yields a coefficient of determination $R^2 = 6 \cdot 10^{-5}$ indicating essentially no linear relationship. There is no obvious difference in the change in permittivity while fasting or the baseline.

Fig. 3.10 shows the change in permittivity as a function of time during Ramadan and after Ramadan. As can be seen there is also no clear relationship. Again, applying a linear regression yields a very weak relationship with $R^2 = 0.02$. There is no obvious difference between the fasting and baseline measurements.

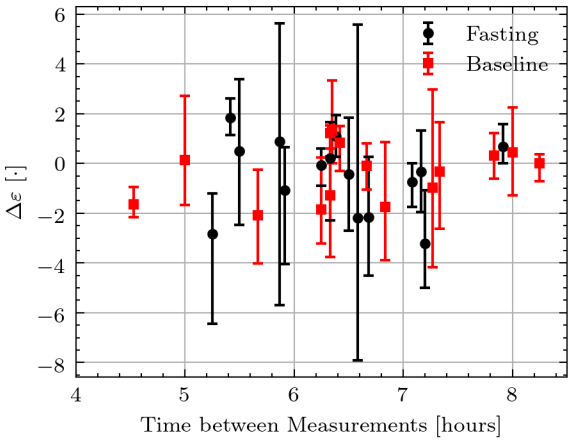

Figure 3.10: Estimated change in permittivity over time of fasting and baseline volunteers. Dots are measurement session medians and error bars are minimum and maximum values.

3.5 Discussion

Weight was consistently lost by all volunteers on all Ramadan fasting days. Only one volunteer reached the commonly defined threshold for clinically relevant changes of 2% body weight (approximately 3% of total body water). However, the actual total body water lost while fasting is even less, as some weight change would be due to voiding. While the changes seen while fasting were on a similar scale as those seen in the wrestlers [8], they occurred over a much longer time period (5 to 9 hours versus 1.5 hours).

The average urine specific gravities during and after Ramadan were close to the commonly defined threshold for dehydration ($U_{sg} > 1.020$) [63]. The urine specific gravity gave no indication that volunteers were undergoing dehydration above their baseline. Note that the first morning urine is considered the most accurate time to measure urine concentration as the processes involved have had time to stabilize overnight [17]. However, in the context of Ramadan the first morning urine would not be an accurate determination of intraday changes in hydration during the fast as participants break their fast overnight. It would be recommended to measure the morning urine to observe interday changes and the urine specific gravity just before the volunteers break their fast to maximize the effect of dehydration.

No clear relationship between the estimated permittivity and changes in hydration were detected here. It is hypothesized this is because the measurement technique is not sensitive enough. Considering both the weight change and urine specific gravity together, the intraday hydration changes were modest. It should be noted that while participants were fasting for upwards of 18 hours, the actual measurement days were between 5-9 hours long. It is possible that if measurements were taken later in the evening larger changes would have been detected.

While a connection issue introduced further complication, the impact was minimized by comparing signals with similar connection quality. Gathering more data with the issue resolved was planned for Ramadan 2020 or Ramadan 2021, but the COVID-19 pandemic made this unfeasible.

3.6 Chapter Conclusion

The Ramadan fast, with no food or drink from sunrise to sunset, provides an interesting scenario for testing hydration assessment technology. However, in sedentary populations the changes in hydration may be too small for useful validation unless measurements are taken over a long fasting period. Care should be taken to utilize the entire fasting period each day, isolate differences between intermittent hypohydration during each fasting day and the chronic changes in hydration throughout the month. laboratory techniques should be used to establish a ground truth. Urine specific gravity failed to accurately detect changes in the fasting population.

The results of this study illustrate the difficulty of accurately assessing the subtle changes in hydration found in healthy, sedentary populations. The TDS method is conceptually simple but provides limited information. This chapter provides motivation for applying tomographic techniques to microwave hydration assessment with the goal of improving technique robustness and increasing sensitivity of the permittivity estimates with respect to changes

in hydration.

Chapter 4

Two-Dimensional Microwave Scattering in Biomedical Applications

4.1 Chapter Introduction

The foundation of MWT techniques is the microwave scattering problem. While the propagation of microwaves in a homogeneous medium may be represented as solutions to the wave equation, often with closed-form analytic expressions [64], the introduction of an object with dissimilar electrical properties (i.e. a scatterer) complicates the solutions. For certain canonical objects, such as infinite cylinders or infinite half planes, an analytical solution can be formed [64]. Analytical solutions can be extended to structured media such as layered elliptical cylinders [65] or half-spaces [66] through techniques like eigenmode expansion. However, biomedical applications rarely fall into these canonical, closed-form solutions so numerical methods must be applied.

The microwave scattering problem consists of two closely related problems: the forward problem and the inverse problem. The forward problem represents the simulation problem where the source field and OUT are known, and the goal is to find the scattered fields. This presents a well-posed problem that can be solved using any of the many computational

electromagnetics techniques such as Finite-Difference Time-Domain (FDTD), Method of Moments (MoM), or Finite Element Method (FEM). With the inverse problem, the source field and scattered field are known (within some measurement error) and the goal is to characterize the unknown OUT. The inverse scattering problem is an ill-posed problem that requires care to generate useful results.

The analysis of the scattering problem will be restricted to the 2D transverse magnetic (TM) case. While the scattering problem can be solved for arbitrary 3D waves [40, 67], restricting to a 2D case greatly simplifies the formulation and resulting computations. Many biomedical scattering problems have made use of this approximation including imaging extremities [11, 37] and 3D breast volumes by creating a series of 2D cross-sections [31, 67].

This chapter will focus on solutions to the forward microwave scattering problem and an introduction to the inverse scattering problem. The MoM with point matching technique is first derived and explored as one method of solving the forward problem. The theory is developed, and the implementation used here is validated. Next, the general inverse microwave scattering problem is introduced. The ill-posedness of the inverse problem is explored through the singular value decomposition (SVD) and the need for additional processing such as iterative solutions and regularization is illustrated.

4.2 Forward Problem

While MWT requires solving the inverse microwave scattering problem, the forward problem proves useful in both formulating and solving the inverse problem. In this work bold typeface lowercase letters will be used to denote vectors and bold typeface uppercase letters will denote matrices.

Consider a typical MWT setup as shown in Fig. 4.1. An object with inhomogeneous dielectric properties defined by eq. (4.1) is placed inside an imaging domain $\mathcal{D}$ with non-magnetic homogeneous background medium with $\varepsilon = \varepsilon_b$.

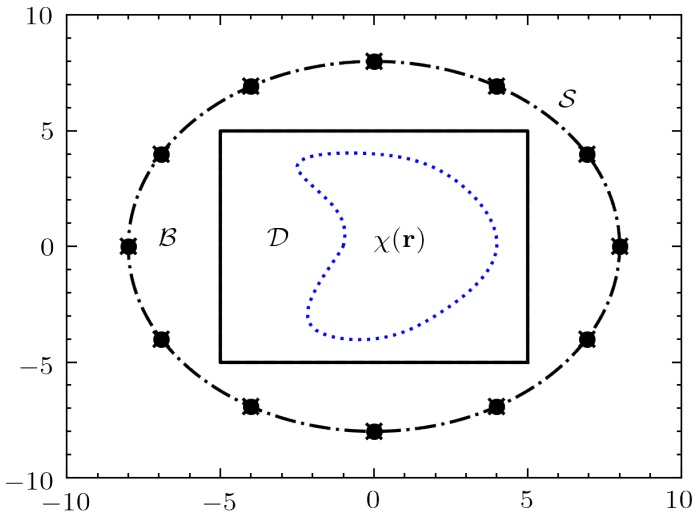

Figure 4.1: Tomographic setup with 12 receivers and 12 transmitters showing imaging domain $\mathcal{D}$, simulation domain $\mathcal{B}$, and measurement surface $\mathcal{S}$

.

$$\varepsilon_r(\boldsymbol{r}) = \varepsilon_r'(\boldsymbol{r}) - j\varepsilon_r''(\boldsymbol{r}) = \varepsilon_r'(\boldsymbol{r}) + \frac{\sigma(\boldsymbol{r})}{j\omega\varepsilon_0} \tag{4.1}$$

where $\boldsymbol{r} = x\hat{\boldsymbol{x}} + y\hat{\boldsymbol{y}}$ is the 2D spatial vector, $\varepsilon_r'(\boldsymbol{r})$ and $\varepsilon_r''(\boldsymbol{r})$ represent the real and imaginary components of complex relative permittivity, respectively, and $\sigma(\boldsymbol{r})$ is the conductivity. Generally, $\varepsilon_r(\boldsymbol{r})$ is also a function of frequency, but a single frequency is assumed for this discussion.

$\mathcal{D}$ is a subdomain of the larger simulation domain $\mathcal{B}$ that also has the properties of the background medium and includes N_{rx} receivers and N_{tx} transmitters with each set equidistant around the imaging domain on surface $\mathcal{S}$.

A normalized contrast function is defined to quantify the difference between the object and the background medium:

$$\chi(\boldsymbol{r}) = \frac{\varepsilon_r(\boldsymbol{r}) - \varepsilon_{r,b}}{\varepsilon_{r,b}} \tag{4.2}$$

Using the above definition, it is easy to see that $\chi(\boldsymbol{r}) = 0, \boldsymbol{r} \notin \mathcal{D}$. In practice, this means the object must fit entirely within $\mathcal{D}$.

The microwave scattering forward problem can be decomposed into two parts: finding the incident fields $\boldsymbol{E}^i(\boldsymbol{r})$ without the object and finding the scattered fields generated by an object of non-zero contrast $\boldsymbol{E}^s(\boldsymbol{r})$. Once both the scattered fields and incident fields are determined the total fields, $\boldsymbol{E}(\boldsymbol{r})$, with the object can be found:

$$\boldsymbol{E}(\boldsymbol{r}) = \boldsymbol{E}^i(\boldsymbol{r}) + \boldsymbol{E}^s(\boldsymbol{r}) \tag{4.3}$$

4.2.1 Incident Fields

The vector wave equation for the electric fields (E-fields) in a charge-free, non-magnetic background medium is given by:

$$\nabla^2 \boldsymbol{E}(\boldsymbol{r}, t) - \mu_0 \varepsilon_b(\boldsymbol{r}) \frac{\partial^2}{\partial t^2} \boldsymbol{E}(\boldsymbol{r}, t) = \mu_0 \frac{\partial}{\partial t} \boldsymbol{J}(\boldsymbol{r}, t) \tag{4.4}$$

Assuming a line current source aligned in the +z-direction with time-harmonic dependence $e^{j\omega t}$, the wave equation reduces to the scalar Helmholtz equation [68]:

$$(\nabla^2 + k_b^2(\boldsymbol{r})) E_z(\boldsymbol{r}) = j\omega\mu_0 J_z(\boldsymbol{r}) \tag{4.5}$$

where $k_b(\boldsymbol{r}) = \omega\sqrt{\varepsilon_b(\boldsymbol{r})\mu_b}$ is the complex wavenumber. The z subscript for all E-fields and currents will be assumed and omitted for the rest of this discussion.

Assuming an ideal line source at location $\boldsymbol{r}_{tx}$, $J(\boldsymbol{r}) = I\delta(\boldsymbol{r_{tx}})\hat{\boldsymbol{z}}$, and applying the Sommerfeld radiation condition, the solution to the above equation for a homogeneous background, $\varepsilon_b(\boldsymbol{r}) = \varepsilon_b$, is the scaled 2D Green's function [64]:

$$E^i(\boldsymbol{r}) = j\omega\mu_0 I G_{2D}(\boldsymbol{r}, \boldsymbol{r}_{tx}) = \frac{-\omega\mu_0 I}{4} H_0^{(2)}(k_b|\boldsymbol{r} - \boldsymbol{r}_{tx}|) \tag{4.6}$$

where I is the complex current phasor and $H_0^{(2)}(x) = J_0(x) - jY_0(x)$ is the 0^{th} order Hankel function of the second kind and $J_0(x)$, $Y_0(x)$ are 0^{th} order Bessel functions of the first and second kinds, respectively.

Eq. (4.6) is an accurate description for ideal current sources in the near-field [68]. The far-field description is readily available from this equation by using the asymptotic expression of the Hankel function for large arguments. The incident field can be calculated easily for other transmitters such as magnetic line sources or plane waves. Extension to 3D can be made, in the case of a line source, by a Fourier transform in z and more generally by defining a set of vector potentials [64].

To most accurately implement a line source within a narrow frequency band a dipole with balun should be used, e.g. [69]. However, if a larger bandwidth is required for use in a multi-frequency application the line source approximation has been applied to a number of linearly polarized antennas with sufficiently low cross-polarization [68]. The antenna should have a large beamwidth in the $x - y$ plane and a small beamwidth in the z direction to ensure constant illumination across the object [68]. A calibration process can be used to reduce the errors between the modelled line source approximation and the actual near-field pattern [70].

4.2.2 Total Fields

While the incident fields have closed form expressions as discussed above, unless simple geometries are involved, the total fields usually must be calculated through any of the computational electromagnetics techniques available in the literature. Two of the most popular methods for solving complex full wave problems in biomedical applications are the FDTD method and FEM. FDTD has a relatively simple formulation that accurately solves complex geometries given cells are sufficiently small to meet the Courant-Friedrichs-Lewy condition [71]. The FDTD method has the benefit of being a time-domain technique, thus allowing for solving multiple frequencies with a single forward solve. However, the entire domain $\mathcal{B}$ must be simulated making the applicability to tomographic techniques less appealing (especially if only one frequency point is required). The FEM represents the current state-of-the-art in frequency domain solvers. The irregular triangular mesh coupled with linear basis functions

allows for highly accurate representations of complex geometries [72]. However, the FEM is quite complicated in implementation.

Here, the point matching MoM technique has been selected. This frequency domain, integral technique has a relatively simple implementation that has been shown to provide accurate solutions for TM configurations [73]. The forward solution will be derived here as it is also the basis of the inverse solver.

Using the equivalence principle, the scattered fields induced by the object can be viewed as an equivalent current density generating a new field [68]. This current density is related to the contrast and electric field through:

$$J_{eq}(\boldsymbol{r}) = j\omega\varepsilon_b\chi(\boldsymbol{r})E(\boldsymbol{r}) \tag{4.7}$$

By finding the field due to each equivalent current filament, the scattered field can be found as:

$$E^s(\boldsymbol{r}) = -\frac{jk_b^2}{4}\iint\limits_{\mathcal{D}} \chi(\boldsymbol{r}')E(\boldsymbol{r}')H_0^{(2)}(k_b|\boldsymbol{r}-\boldsymbol{r}'|)d\boldsymbol{r}' \tag{4.8}$$

Thus, the total field is:

$$E(\boldsymbol{r}) = E^i(\boldsymbol{r}) - \frac{jk_b^2}{4}\iint\limits_{\mathcal{D}} \chi(\boldsymbol{r}')E(\boldsymbol{r}')H_0^{(2)}(k_b|\boldsymbol{r}-\boldsymbol{r}'|)d\boldsymbol{r}' \tag{4.9}$$

The above equation is linear, well-posed, and essentially involves applying a convolution operator.

To solve numerically, the contrast and fields are expanded using a set of basis functions $f_{ij}(\boldsymbol{r})$ such that:

$$\chi(\boldsymbol{r}) = \sum_{i=1}^{N_x}\sum_{j=1}^{N_y}\chi_{ij}f_{ij}(\boldsymbol{r}) \qquad\qquad E(\boldsymbol{r}) = \sum_{i=1}^{N_x}\sum_{j=1}^{N_y}E_{ij}f_{ij}(\boldsymbol{r}) \tag{4.10}$$

where $\mathcal{D}$ is divided into N_x, N_y cells in the x and y directions, respectively.

A series of pulses will be used as basis functions.

$$f_{ij}(\boldsymbol{r}) = \begin{cases} 1, & \text{if } \boldsymbol{r} \in \mathcal{D}_{ij} \\ 0, & \text{otherwise} \end{cases} \tag{4.11}$$

where $\mathcal{D}_{ij}$ is the ijth cell of the imaging domain such that $\bigcup_{ij} \mathcal{D}_{ij} = \mathcal{D}$. This discretization assumes that the subdomains are sufficiently small such that the contrast and E-fields are constant over the subdomains. While more complicated bases such as piecewise triangular functions can be used to provide more accurate solutions for the same number of basis functions [74] this provides a simple formulation.

Next, an inner product of complex functions is defined over the imaging domain as:

$$< u(\boldsymbol{r}), v(\boldsymbol{r}) >= \int_{\mathcal{D}} u(\boldsymbol{r}) v^*(\boldsymbol{r}) d\boldsymbol{r} \tag{4.12}$$

where $u(\boldsymbol{r})$, $v(\boldsymbol{r})$ are some complex functions and $(\cdot)^*$ denotes the complex conjugate.

Using this inner product and a pulse testing function defined by eq. (4.13) the output field is enforced at the center of the cells.

$$w(\boldsymbol{r}) = \delta(\boldsymbol{r} - \boldsymbol{r}') \tag{4.13}$$

resulting in the final discretized equation:

$$E^i_{ij} = E_{ij} + \frac{jk_b^2}{4} \sum_{m=1}^{N_y} \sum_{n=1}^{N_x} \chi_{nm} E_{nm} \cdot \iint_{\mathcal{D}_{nm}} H_0^{(2)}(k_b |r_{ij} - \boldsymbol{r}|) d\boldsymbol{r} \tag{4.14}$$

where i, j are the indices of the output fields and n, m are the indices of the equivalent sources.

This is the commonly used MoM technique with point matching [75]. The point matching method is often selected for its simplicity, specifically with the simple evaluation of eq. (4.12).

Other common techniques such as Galerkin's method where $f = w$ can provide more accurate results, but point matching is generally quite accurate [75].

To solve this equation, the Hankel function response can be solved analytically by approximating the square cells as circles of equal area [76]:

$$\iint\limits_{\mathcal{D}_{nm}} H_0^{(2)}(k_b|r_{ij} - \boldsymbol{r}|)d\boldsymbol{r} = \int\limits_0^{2\pi}\int\limits_0^{a_{nm}} H_0^{(2)}(k_b|r_{ij} - \boldsymbol{r}'|)dr'd\phi'$$

$$\int_0^{2\pi}\int_0^{a_{nm}} H_0^{(2)}(k_b|r_{ij} - \boldsymbol{r}|)d\boldsymbol{r}d\phi = \begin{cases} \frac{j}{2}(\pi k_b a H_1^{(2)}(k_b a_{nm}) - 2j), & \text{if } i,j = m,n \\ \frac{j\pi k_b a_{nm}}{2} J_1(k_b a_{nm}) H_0^{(2)}(k_b|r_{ij} - r_{mn}|), & \text{if } i,j \neq m,n \end{cases} \tag{4.15}$$

where $a_{nm} = \sqrt{\frac{\Delta x \Delta y}{\pi}}$ is the radius of a circle with area equal to that of cell D_{nm} and $\phi = \tan^{-1}(\frac{r_y}{r_x})$. Note that when the output field (indices i, j) is colocated with the equivalent source (indices m, n) the analytic solution manages the singularity associated with the imaginary component of the Hankel function [76].

The discretized system can be solved by finding the solution to the linear equation:

$$\boldsymbol{e^i} = \boldsymbol{C}\boldsymbol{e} \tag{4.16}$$

where $\boldsymbol{e^i}$, $\boldsymbol{e}$ are $N^2 \times 1$ column vectors with entries E_{ij}^i, and E_{ij} respectively. $\boldsymbol{C}$ is an $N^2 \times N^2$ matrix with entries:

$$C_{ij,nm} = \delta_{ij,nm} + \frac{jk_b^2}{4}\chi_{ij,nm}\iint_{\mathcal{D}_{nm}} H_0^{(2)} k_b|\boldsymbol{r}_{ij} - \boldsymbol{r}|d\boldsymbol{r} \tag{4.17}$$

Eq. (4.16) can be solved straightforwardly by calculating $\boldsymbol{C}^{-1}$. Note that $\boldsymbol{C}$ is only a function of the problem geometry so $\boldsymbol{C}^{-1}$ can be solved for once and applied to any incident field (i.e. from different transmitters) in that geometry.

Once the total fields inside the domain have been calculated, the scattered fields inside

the domain can be trivially found through eq. (4.3). Using the fact that $\chi(\boldsymbol{r}) = 0, \boldsymbol{r} \notin \mathcal{D}$ the scattered fields can be found at any point outside the domain using eq. (4.8) including at the receivers. In practice, the domain is not of infinite extent, so there will be some boundary condition that will contribute to the model errors.

While this solution is conceptually simple, the computational complexity and memory requirements are prohibitive for large $N = N_x \cdot N_y$. The computational complexity is on the order of N^3 with memory requirements of N^2 [73]. However, by making use of the convolutional nature of the problem, k-space techniques can be applied to greatly reduce the computation complexity. The fast Fourier transform, conjugate gradient method (FFT-CGM) reduces the computational complexity to $N \log N$ [73, 77].

The complete details of the FFT-CGM algorithm can be found in Appendix A based on the method outlined in [78]. The technique utilizes a standard CGM implementation for non-square, non-symmetric matrices. The summation is cast a linear operator and its Hermitian which can be efficiently evaluated as a convolution using the FFT.

4.2.3 Validation

The MoM results will be validated using the analytic solution of the scattered field due to a homogeneous cylinder. The scattered fields at any point inside or outside the cylinder due to a source at position $\boldsymbol{r}_{tx}$ can be found by considering the boundary value problem and applying a Bessel series as outlined in [64]. The derivation for scattered fields due to a line source is provided in Appendix B.

Three problem sets are used to validate the MoM solver: a lossless dielectric cylinder with $\varepsilon_{r,d} = 2$ placed in free space, a lossy dielectric cylinder with $\varepsilon_{r,d} = 64 + j18$ placed in a lossless background medium $\varepsilon_{r,b} = 36$, and a perfect electric conductor (PEC) cylinder ($\varepsilon_{r,d} = 10^9$) in the lossless background medium. For all scenarios the cylinder size is restricted to about two wavelengths in the background medium at 1 GHz. The scattered fields will be compared at 32 locations around the cylinder on a circle of radius four wavelengths and through the

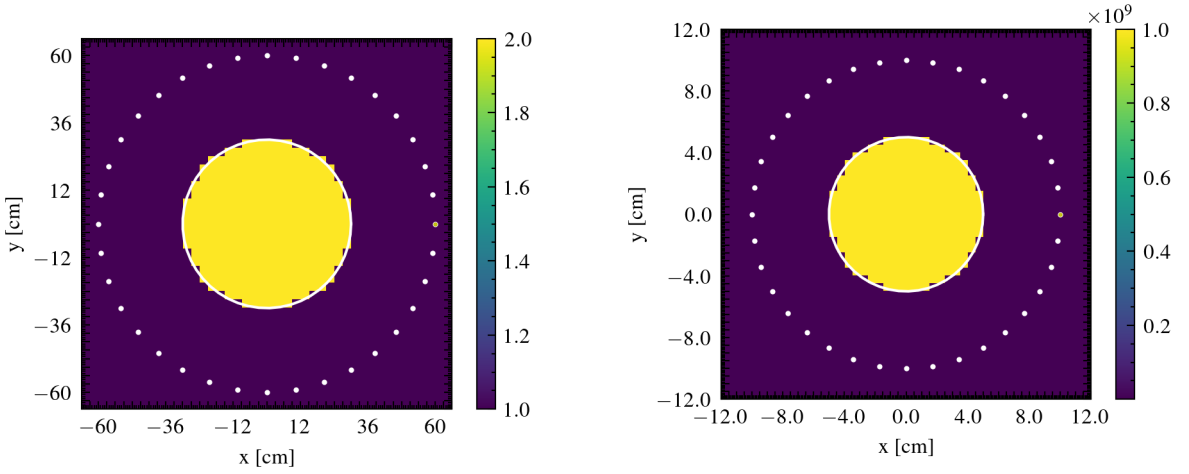

(a) Permittivity of lossless cylinder in free space.

(b) Permittivity of PEC cylinder in background medium.

Figure 4.2: Homogeneous cylinders used for analytic solutions.

cylinder on the x and y axes. The cylinders will be discretized to 100 cells/λ^2 which is an oft cited rule of thumb for accurate solutions with MoM [75]. Fig. 4.2a shows the cylinder in free space and Fig. 4.2b shows the PEC cylinder in the background medium. The lossy cylinder is omitted but has the same dimensions as Fig. 4.2b. For computational simplicity, a current phasor $I = 1\angle 0°$ A is used. This is larger than the 1 μA $-$ 1 mA currents that can be expected in a typical physical implementation.

The relative residual error (RRE) defined by eq. (4.18) is used to quantify the error over the complex scattered fields.

$$RRE = \frac{\sum |E^s_{analytic} - E^s_{simulated}|}{\sum |E^s_{analytic}|} \tag{4.18}$$

As shown in Figs. 4.3 through 4.8 the simulated fields follow a similar trend to the analytic solution for all test scenarios. Table 4.1 has the relative residual errors for the test objects. The RRE is undefined inside the PEC cylinder because the analytic fields are zero.

The 100 cells/λ^2 discretization provides accurate solutions. The accuracy can be improved by increasing the discretization.

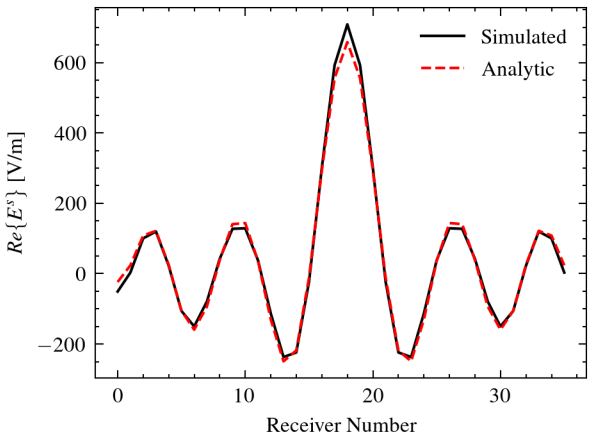

(a) Real component.

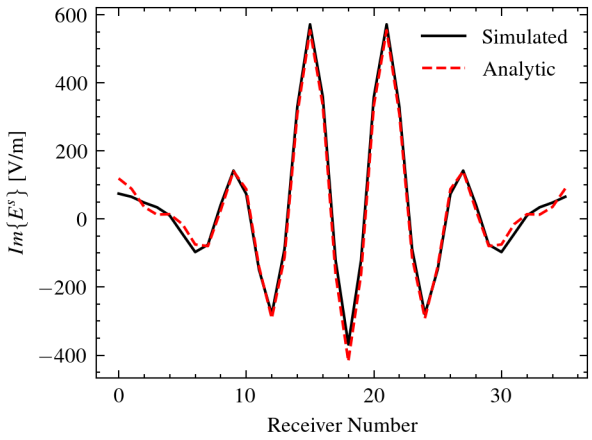

(b) Imaginary component.

Figure 4.3: Scattered fields from lossless homogeneous cylinder in free space.

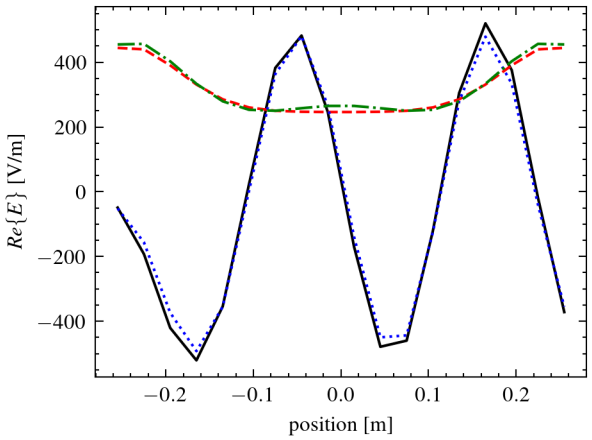

(a) Real component.

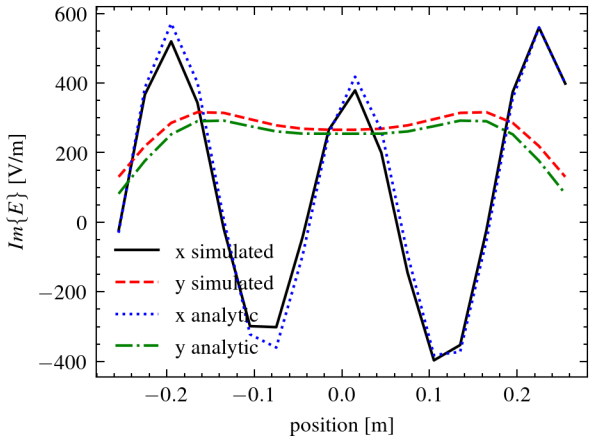

(b) Imaginary component.

Figure 4.4: Total fields inside lossless cylinder in free space.

Table 4.1: Relative residual error for test objects.

RRE	Lossless Cylinder	Lossy Cylinder	PEC Cylinder
Outside Cylinder	0.10	0.03	0.11
Inside Cylinder x-axis	0.09	0.06	-
Inside Cylinder y-axis	0.07	0.05	-

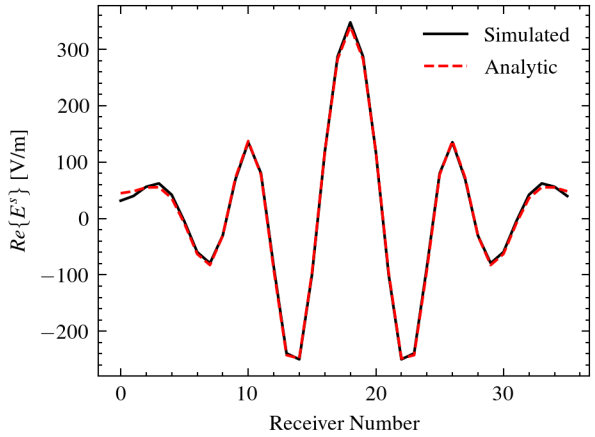

(a) Real component.

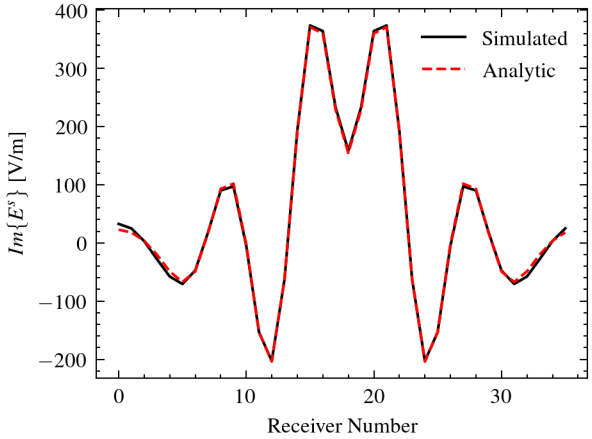

(b) Imaginary component.

Figure 4.5: Scattered fields from lossy homogeneous cylinder in background medium.

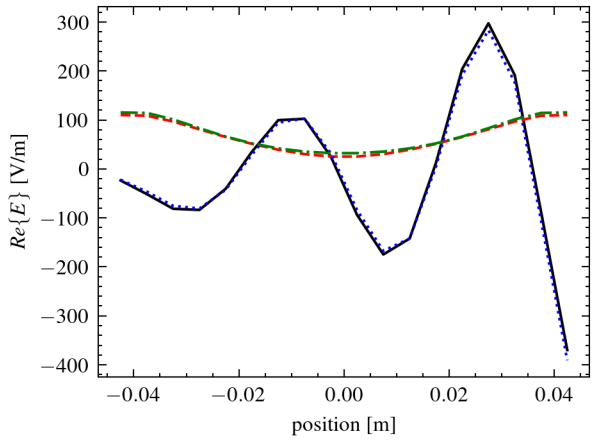

(a) Real component.

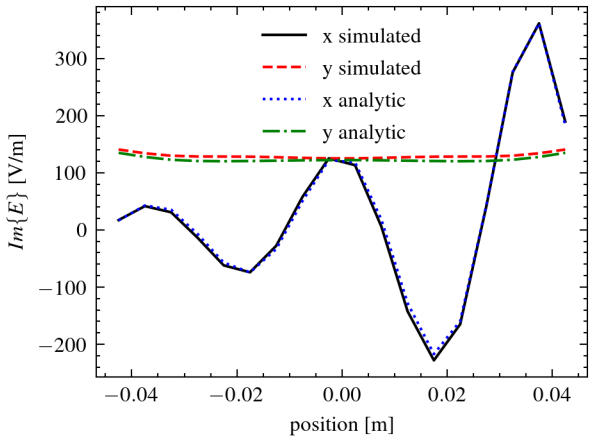

(b) Imaginary component.

Figure 4.6: Total fields inside lossy homogeneous cylinder in background medium.

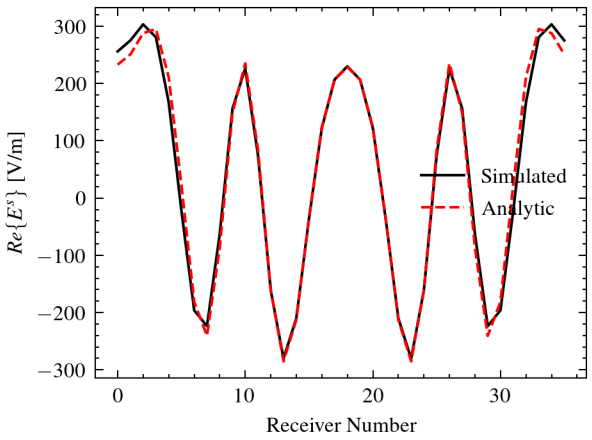

(a) Real component.

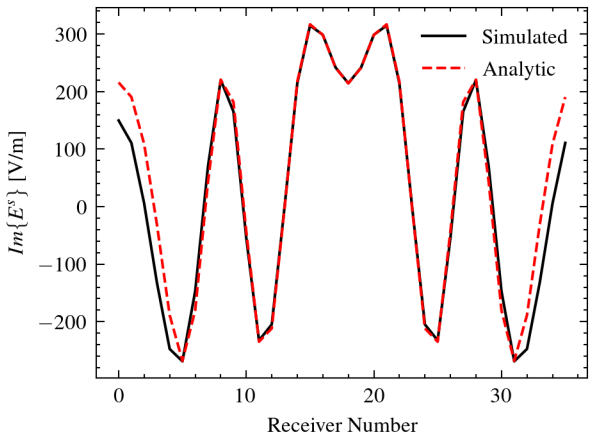

(b) Imaginary component.

Figure 4.7: Scattered fields from PEC cylinder in background medium.

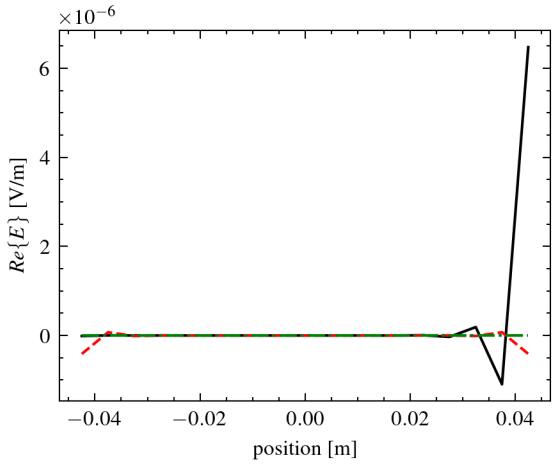

(a) Real component.

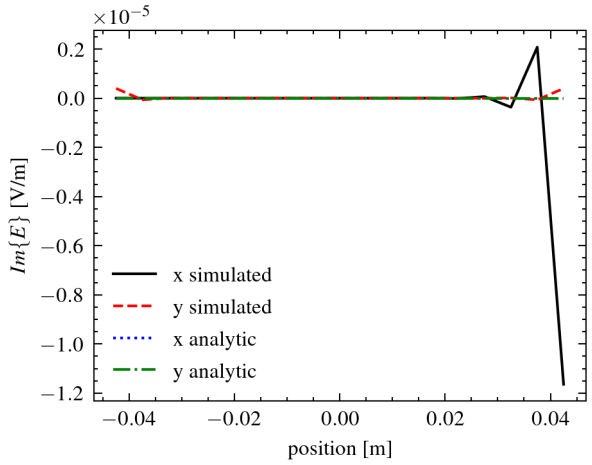

(b) Imaginary component.

Figure 4.8: Total fields inside PEC cylinder in background medium.

4.3 Inverse Problem

The inverse microwave scattering problem is the analytical basis of MWT. While this problem is of great practical interest, the physics of microwave scattering lead to a non-linear, ill-posed problem that proves difficult to solve.

A problem is considered well posed if it has a solution that is unique and depends continuously on the data [79] and is ill-posed if any of these criteria are not met. As a practical matter, the inverse problem must have a solution because some physical object created the scattered fields [80]. However, it is possible that noise and modelling errors preclude a solution to real measurements [68]. The question of uniqueness is of much greater interest. It has been shown that for noiseless measurements, the 2D inverse scattering solution is unique provided all measurement locations and angles are used [81, 82]. Applying *a priori* assumptions can help ensure uniqueness when finite measurement views are used [81] but, in general, for a practical problem the solution is not unique [80]. The greatest issue in practical microwave inverse scattering is stability. The noise in measurement data and discretization of the problem introduce inexorable errors that can make the reconstructed profile varying greatly. As will be seen in this section, even simple lossless objects with minimal measurement error present a very ill-posed problem that will require the incorporation of some *a priori* information to generate useful results. This regularization is a necessary step to 1) select one of the many possible solutions and 2) stabilize the problem.

The basic microwave inversion technique using the point matching scheme will now be discussed and analyzed. Similar to Section 4.2 the inverse problem will be formulated as a 2D TM problem.

From the forward problem, the scattered field equation has previously been derived. For practical situations where the scattered fields are measured at discrete points outside the imaging domain there are two closely related equations that govern the inverse scattering problem: the data equation eq. (4.19) which gives the scattered field at the measurement locations and the state equation eq. (4.20) which provides the fields within the imaging

domain [68].

$$E(\boldsymbol{r}_{rx}) - E^i(\boldsymbol{r}_{rx}) = E^s(\boldsymbol{r}_{rx}) = -\frac{jk_b^2}{4}\iint_{\mathcal{D}} \chi(\boldsymbol{r})E(\boldsymbol{r})H_0^{(2)}(k_b|\boldsymbol{r}_{rx} - \boldsymbol{r}|)d\boldsymbol{r}, \boldsymbol{r}_{rx} \in \mathcal{S}, \boldsymbol{r} \in \mathcal{D} \tag{4.19}$$

$$E(\boldsymbol{r}) - E^i(\boldsymbol{r}) = E^s(\boldsymbol{r}) = -\frac{jk_b^2}{4}\iint_{\mathcal{D}} \chi(\boldsymbol{r}')E(\boldsymbol{r}')H_0^{(2)}(k_b|\boldsymbol{r} - \boldsymbol{r}'|)d\boldsymbol{r}', \boldsymbol{r}, \boldsymbol{r}' \in \mathcal{D} \tag{4.20}$$

For the forward problem, the data equation is a Fredholm integral equation of the first kind whereas the state equation is a Fredholm equation of the second kind [68]. However, for the inverse problem both the data and states equations are inhomogeneous non-linear Fredholm equations of the first kind. Fredholm equations arise in numerous inversion problems involving remote sensing and indirect measurements such as atmospheric sounding, seismology, and ultrasound [83]. While the forward scattering problem (eq. (4.9)) is linear, the inverse scattering problem is non-linear due to the fact that the scattered fields depend on the contrast and total fields, but the total fields are themselves a function of the contrast. A subtle difference between the two equations is the scattered field at the receivers is known (within some measurement accuracy), but the scattered field within the imaging domain is unknown. In practice, the scattered field is measured by taking an total field measurement without the OUT and a total field measurement with the OUT.

The Fredholm integral of the first type has the form:

$$g(t) = \int_a^b K(s,t)f(s)ds \tag{4.21}$$

where $g(t)$ is the measured data, $K(t,s)$ is the kernel, and $f(s)$ is the desired, unknown function. Note that for the case $K(s,t) = K(s-t)$ the forward problem represents a convolution operator.

The ill-posedness of the Fredholm equation is related to the smoothness of the kernel where smoothness is defined as the number of continuous partial derivatives [84]. The smoother the kernel, the more the desired function is smoothed in the output. Thus, the forward problem can be viewed as a low-pass filter operation, and the inverse operation can be thought to amplify high frequency components.

The inverse scattering problem is further complicated by the fact that the scattered field is non-linear. For a given geometry, the non-linear effects are worse with higher frequencies and higher contrasts [68]. The inverse scattering problem can be linearized by assuming $E(\boldsymbol{r}) = E^i(\boldsymbol{r})$. This is the well-known Born or small-scatterer approximation which is valid for small objects with small contrast. The Born approximation can be considered valid for relative phase changes through the scatterer of about π [85] however there are other metrics used in the literature [86]. While this is generally not valid for biomedical applications, it can be useful in examining the ill-posedness of a practical inversion.

Applying the Born approximation, the inverse scattering problem reduces to:

$$E^s(\boldsymbol{r}) = -\frac{jk_b^2}{4}\iint \chi(\boldsymbol{r}')E^i(\boldsymbol{r}')H_0^{(2)}(k_b|\boldsymbol{r}-\boldsymbol{r}'|)d\boldsymbol{r}' \tag{4.22}$$

The discretized problem can be written as a system of linear equations:

$$\boldsymbol{e}^s = \boldsymbol{M}\boldsymbol{x} \tag{4.23}$$

where $\boldsymbol{e}^s$ is an $N_{rx}\cdot N_{tx}\times 1$ vector with entries E^s, $\boldsymbol{x}$ is an $N_x\cdot N_y\times 1$ vector with entries χ, and $\boldsymbol{M}$ is an $N_{rx}\cdot N_{tx}\times N_x\cdot N_y$ matrix with entries:

$$M_{pq,ij} = -\frac{jk_b^2}{4}E^i_{p,nm}\iint_{\mathcal{D}_{nm}} H_0^{(2)}(k_b|r_q-\boldsymbol{r}'|)d\boldsymbol{r}' \tag{4.24}$$

where $p = 1,2,\ldots,N_{tx}$, $q = 1,2,\ldots,N_{rx}$ and i,j are the x,y indices inside the imaging domain.

4.3.1 Singular Value Decomposition

To quantify the ill-posedness of the inverse operation, the SVD of the inversion matrix can be used. Consider a complex matrix $\boldsymbol{A}$ of size $m \times n$ with rank p. The SVD is a rank-revealing decomposition that factors a matrix into sets of orthonormal vectors $\boldsymbol{u}_i$, $\boldsymbol{v}_i$ and associated singular values s_i [87].

$$\boldsymbol{A} = \boldsymbol{U}\boldsymbol{S}\boldsymbol{V}^{\boldsymbol{H}} \tag{4.25}$$

where U is an $m \times m$ unitary matrix with the set of vectors u_i, V is an $n \times n$ unitary matrix with a set of vectors v_i, S is a diagonal matrix with entries s_i, and $(\cdot)^H$ denotes the conjugate transpose. The SVD is rank revealing because $s_i = 0$, $i > p$. SVD algorithms are available in common linear algebra libraries such as NumPy [88] and LAPACK [89].

The SVD provides many valuable insights into $\boldsymbol{A}$ including the invertibility, condition number, and pseudoinverses. It is useful to know that the inverse of $\boldsymbol{A}$ (if it exists) can be found from the SVD as:

$$\boldsymbol{A}^{-1} = \boldsymbol{V}\boldsymbol{S}^{-1}\boldsymbol{U}^{H} \tag{4.26}$$

where S^{-1} is now a diagonal matrix with elements $1/s_i$.

However, in many inverse problems there are many more unknowns than there are measurements, that is $m > n$. From the proceeding definitions it is easy to see that the matrix is singular because there are some $s_i = 0$. Thus, it is useful to define a pseudoinverse:

$$\boldsymbol{A}^{\dagger} = \boldsymbol{V}\boldsymbol{S}^{\dagger}\boldsymbol{U}^{H} \tag{4.27}$$

where $(\cdot)^\dagger$ denotes the pseudoinverse and $\boldsymbol{S}^\dagger$ is a diagonal matrix with entries $1/s_i$ for $i < p$ with the remaining diagonal entries left as 0.

A distinction should be made between rank deficient and ill-posed problems both of which

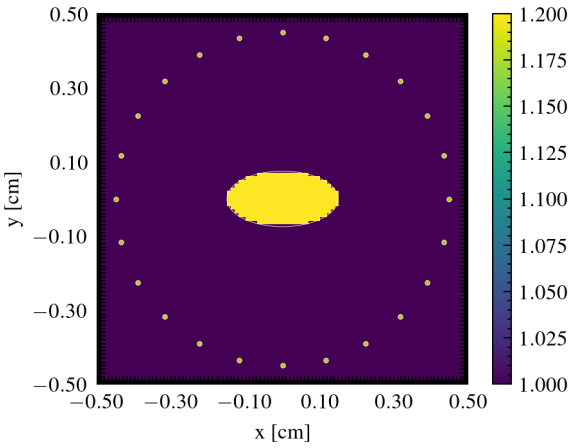

Figure 4.9: Tomographic setup for imaging homogeneous elliptical cylinder.

will have singular matrices $\boldsymbol{A}$. If a problem is merely rank deficient there are often simple solutions that provide accurate results e.g. the linear least squares solution.

$$\boldsymbol{x} = \arg\min_{x} \|\boldsymbol{b} - \boldsymbol{A}\boldsymbol{x}\| \tag{4.28}$$

which can be solved as:

$$\boldsymbol{x} = (\boldsymbol{A}^H\boldsymbol{A})^{-1}\boldsymbol{A}^H\boldsymbol{b} \tag{4.29}$$

A rank deficient problem has a well-defined gap in singular values indicating linearly dependent measurements and redundant information and thus a clear definition of effective rank [84]. An ill-posed problem has slowly decaying singular values with no clear definition of effective rank. As will be seen, the linear least squares solution will not be enough to solve the ill-posed problem and in fact often generates worse results.

4.3.2 Direct Inversion and Singular Values

To examine the ill-posedness of the inverse microwave problem, SVD can be applied to $\boldsymbol{M}$ and the singular values analyzed.

Consider an inverse problem where the Born approximation holds: an infinite homoge-

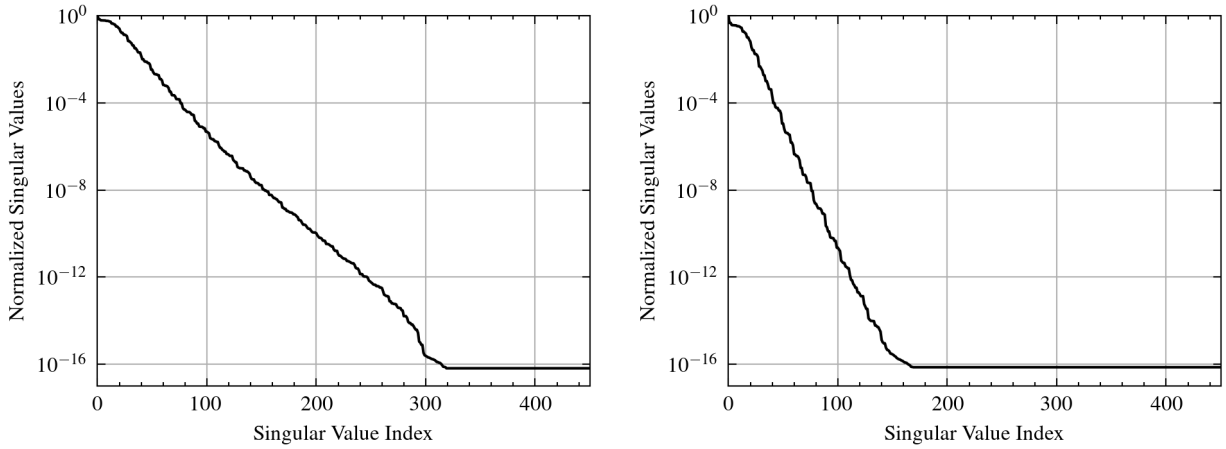

(a) Singular values of $\boldsymbol{M}$

(b) Singular values of $\boldsymbol{M}^H\boldsymbol{M}$

Figure 4.10: Singular values for a homogeneous elliptical cylinder.

neous elliptical cylinder with properties $\varepsilon_r(\boldsymbol{r}) = 1.2 + j0$ with major axis length 30 cm and minor axis length 15 cm placed in an 30 cm x 30 cm imaging domain of free space as shown in Fig. 4.9. Let there be 24 equidistant receivers and transmitters placed on a circle of radius 45 cm. To solve numerically, the image domain is discretized into a 30 x 30 grid.

To analyze both the direct inversion and the linear least squares solution, the singular values of both $\boldsymbol{M}$ and $\boldsymbol{M}^H\boldsymbol{M}$ are generated as seen in Fig. 4.10.

In both cases, the singular values decrease gradually until they reach the machine precision. Note that there are only a maximum of 450 linearly independent measurements due to the reciprocity of signals between transmitters and receivers. This gradual decay of singular values is characteristic of ill-posed problems [84].

Simulated measurements are generated on the same grid with no noise added. The permittivity is solved for using direct inversion and linear least squares.

As can be seen in Fig. 4.11, the direct inversion and linear least squares solutions give very poor results. Due to the very poor conditioning of the problem, the resulting permittivity estimates are highly innacurate. As expected from the singular values, the linear least squares solution is worse than the direct inversion which is a well-known result for ill-posed problems [83].

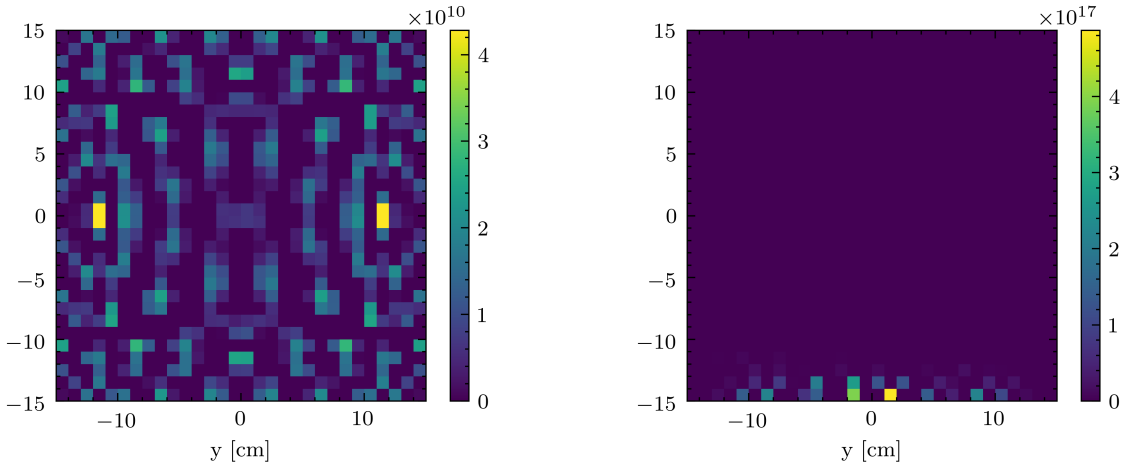

(a) Direct inversion solution.

(b) Linear least squares solution.

Figure 4.11: Results from inversion of homogeneous cylinder without regularization.

These results motivate looking into more advanced methods of solving the inverse scattering problem. In general, some *a priori* information will be used to solve the inverse scattering problem through a process called regularization.

4.4 Chapter Conclusion

In this chapter, standard approaches to the forward microwave scattering problem have been developed and validated. This forward solver will prove very useful in both solving and validating solutions to the inverse scattering problem. The formulation of the inverse problem has been discussed and the ill-posedness of a simple linear inversion has been explored. The ill-posed problem prevents the application of standard direct and least squares techniques to solve the linear matrix equation.

Chapter 5

Microwave Tomography for Hydration Assessment

5.1 Chapter Introduction

As discussed in Chapter 2, because hydration is bulk property of the tissue, THA requires a lower resolution image than typical MWT applications, allowing a simpler system and approach.

In this chapter, the non-linear inversion and requisite regularization used to detect changes in the properties of the forearm are discussed and validated *in silico*. The focus of the current formulation is a proof of concept using basic microwave tomography techniques. The Distorted Born Iterative Method (DBIM) is introduced and analyzed as a method of inversion. The application of the DBIM is extended to change detection between time-series data. The regularization of this technique is then discussed through the well-known Tikhonov regularization and L-curve tool. A simple adaptive regularization technique is introduced to help linearize the initial iterations. These techniques are then applied to a realistic forearm models. An *in silico* analysis of tomographic system design parameters is used to obtain a standard tomographic system optimized for hydration monitoring.

5.2 Non-linear Inversion

As seen in Section 4.3, the data and state equations (eqs. (4.19), (4.20)) are non-linear. Typically, solutions to the non-linear microwave scattering inverse problem consist of iterative methods that solve the data and state equations in turn.

The first class of solutions involves extensions to the Born approximation called the Born iterative method (BIM) [90] and the DBIM [91]. For these methods, the state equation is solved at each iteration, k, through a forward solve with an estimate of the contrast function χ_k. The data equation is then solved using the estimate of the total fields to update the contrast function χ_{k+1} and the process is repeated. In the BIM, the linearized equation eq. (4.23) is applied at each iteration assuming the scattered fields propagate in the homogeneous background medium. However, in the DBIM the inversion is done on the residual error between the calculated and measured scattered fields to yield a contrast step $\Delta\chi_k$. Both techniques yield non-linear solutions using iterative linear methods. The DBIM is generally a better solution to the non-linear problem, because the Green's function is updated (or distorted) at each iteration to account for the propagation in the inhomogeneous medium.

Another commonly used formulation for non-linear inversion is the contrast source inversion (CSI) [92] technique. CSI is an iterative method where the contrast $\chi(\boldsymbol{r})$ and the contrast sources $\chi(\boldsymbol{r})E(\boldsymbol{r})$ are sequentially updated using the data and state equations, respectively. One major difference between CSI and Born methods is that no forward solver calls are required in CSI to generate solutions. In addition, the CSI method with multiplicative regularization has been shown to perform better than the DBIM especially in blind inversions [43]. The DBIM was selected for its simpler implementation.

5.2.1 Distorted Born Iterative Method

The details for the DBIM algorithm will now be discussed.

The algorithm is initialized with some contrast distribution $\chi_0(\boldsymbol{r})$. This distribution can

be an *a priori* estimate of the final distribution or the Born approximation can be applied to generate an initial solution. After generating $\chi_0(\boldsymbol{r})$, the scattered and total fields are found through a forward solver call, eqs. (4.8), (4.9). The residuals between the measured and simulated scattered fields are then found as:

$$\Delta \boldsymbol{e}_k^s = \boldsymbol{e}_k^s - \ddot{\boldsymbol{e}}^s \tag{5.1}$$

where $\boldsymbol{e}_k^s$ is the simulated scattered fields at iteration k and $\ddot{\boldsymbol{e}}^s$ is the measured data.

Additionally, the DBIM updates the Green's function to better account for the phase changes and non-linear effects of larger and higher contrast objects. However, the updated Green's function must be calculated at each iteration. In general, the distorted Green's function does not have a closed form solution so it must be computed numerically. Using the reciprocity theorem in electromagnetics, the Green's function can be found by using forward solves at each of the receivers. While this could be quite computationally intensive, if the transmitters and receivers are co-located ($\boldsymbol{r}_{rx} = \boldsymbol{r}_{tx}$) and the total fields from the transmitter have been computed, the Green's function can be found simply by applying eq. (5.2).

$$G_k(\boldsymbol{r}_{rx}, \boldsymbol{r}) = \frac{1}{j\omega\mu_0 I} E_k(\boldsymbol{r}_{tx}, \boldsymbol{r}), \boldsymbol{r}_{rx} = \boldsymbol{r}_{tx} \tag{5.2}$$

Applying the distorted Green's function and the estimate of the total fields to the residuals with the discretization outlined in Chapter 4 yields the linear equation:

$$\Delta \boldsymbol{e}_k^s = \boldsymbol{M}_k \boldsymbol{\Delta\chi}_k \tag{5.3}$$

where $\boldsymbol{M}_k$ is the distorted Green's function operator with elements:

$$M_{pq} = \int_{\mathcal{D}} k_{b,k}^2(\boldsymbol{r}) E_{p,k}(\boldsymbol{r}) G_k(\boldsymbol{r}, \boldsymbol{r_q}) d\boldsymbol{r}$$
$$M_{pq,ij} = k_{b,ij,k}^2 E_{q,ij,k} G_{q,ij,k} \cdot (dx \cdot dy)_{ij} \tag{5.4}$$

where $p = 1, 2, ..., N_{tx}$, $q = 1, 2, ..., N_{rx}$, $i = 1, 2, ..., N_x$, $j = 1, 2, ..., N_y$, $k_{b,k}(\boldsymbol{r})$ is the inhomogeneous wavenumber in the medium $\chi_k(\boldsymbol{r})$, and $dx \cdot dy$ is the area of element $\mathcal{D}_{ij}$. Because it is assumed that the field and contrast values are constant over the discrete elements $\mathcal{D}_{ij}$ the integral in eq. (5.4) reduces to a simple area calculation.

Eq. (5.3) is an ill-posed equation that requires regularization to generate useful $\Delta\chi_k(\boldsymbol{r})$. The contrast is then updated by adding the update step:

$$\chi_{k+1}(\boldsymbol{r}) = \chi_k(\boldsymbol{r}) + \Delta\chi_k(\boldsymbol{r}) \tag{5.5}$$

Once the contrast is updated, the forward solver is run again, and the process is repeated until convergence.

At each iteration, the scattered fields at the receivers are calculated and compared to the measured data to check convergence. By defining the relative residual error (repeated here from eq. (4.18)), the quality of the inversion can be quantified.

$$RRE_k = \frac{\sum_{rx} ||\boldsymbol{e}_k^s - \ddot{\boldsymbol{e}}^s||_2}{\sum_{rx} ||\ddot{\boldsymbol{e}}^s||_2} = \frac{\sum_{rx} ||\Delta\boldsymbol{e}^s||_2}{\sum_{rx} ||\ddot{\boldsymbol{e}}^s||_2} \tag{5.6}$$

Once the residuals reach some predefined threshold, F, or increase, the algorithm can terminate. Other stopping criteria for the DBIM include: a maximum number of iterations or a definition of convergence based on the decrease in residuals or change in contrast.

The DBIM algorithm is summarized here:

1. Initialize solver with $\chi_0(\boldsymbol{r})$. Either solve for $\chi_0(\boldsymbol{r})$ using the Born approximation $E_0(\boldsymbol{r}) = E^i(\boldsymbol{r})$, or use an *a priori* estimate.

2. Run a forward solve with $\chi_{k-1}(\boldsymbol{r})$ to update total fields inside image domain $E_k(\boldsymbol{r})$, the scattered fields at the receivers E_k^s, and the distorted Green's function $G_k(\boldsymbol{r}, \boldsymbol{r}_{tx})$.

3. Check convergence. If $RRE_k < F$ or $RRE_k > RRE_{k-1}$, terminate algorithm.

4. Compute distorted Greens function operator, $\boldsymbol{M}_k$ using eq. (5.4).

5. Solve for contrast update $\Delta\chi_k(\boldsymbol{r})$ with appropriate regularization and update contrast.

6. Go to step 2.

The dielectric properties associated with $\chi_k(\boldsymbol{r})$ must be restricted to physical values after each iteration ($Re\{\varepsilon_{r,k}(\boldsymbol{r})\} \geq 1$, $\sigma_k(\boldsymbol{r}) \geq 0$) in order to be able to do the forward solve. *A priori* information can also be incorporated by enforcing minimum and maximum values.

The distorted Born iterative method has been shown to be equivalent to non-linear Gauss-Newton (GN) optimization [93] that is also commonly used in non-linear microwave imaging, e.g. [94]. The contrast update $\Delta\chi_k(\boldsymbol{r})$ is equivalent to the step direction and the distorted Green's function operator $\boldsymbol{M_k}$ is equivalent to the Jacobian. This is an important result as the literature on non-linear optimization using the GN method can be applied to explore the convergence and behavior of the DBIM. An important aspect of the GN method is that it is only locally convergent thus its performance strongly depends on the choice of $\chi_0(\boldsymbol{r})$. This local convergence is complicated by the need for regularization as will be discussed in the next sections. Initializing the DBIM with the Born approximation can be unreliable for higher frequencies and higher contrast objects.

To improve convergence, a number of augmentations can be used such as a linear search algorithm to reduce the step size if the residuals increase [95] or smoothing the image after each iteration [96].

Because the contrast updates are carried out as a function of the residual error, the DBIM is more susceptible to noise than the BIM [91] and a good first estimate for the error threshold is the noise level of the measured scattered signal.

5.2.2 Change Detection

While reconstructing physiologically meaningful permitivities for forearm imaging has previously been shown [11], which lends credence to microwave tomography as an accurate imaging modality, for hydration monitoring the relative change over time is more relevant.

The DBIM algorithm lends itself well to a number of extensions for change detection. Consider a baseline scattered field measurement $E^{s,b}(\boldsymbol{r})$ taken while the subject is assumed to be at euhydration and another measurement $E^{s,d}(\boldsymbol{r})$ when the subject has an unknown hydration status. The difference between the reconstructed properties $\delta\chi(\boldsymbol{r}) = \chi^d(\boldsymbol{r}) - \chi^b(\boldsymbol{r})$ can be found in a number of ways.

The first method is to apply the DBIM algorithm to both measurements separately with whatever initialization χ_0 is required to converge to useful solutions, $\chi^d(\boldsymbol{r})$ and $\chi^b(\boldsymbol{r})$. In this way the absolute reconstructed properties can be compared. This process has benefits in that the data are treated separately with no assumption of similarity between the measurements. However, this will be more computationally intensive as the full reconstructions from the *a priori* distribution, $\chi_0(\boldsymbol{r})$, is required.

The next logical step would be using the baseline reconstruction, $\chi_b(\boldsymbol{r})$, as the initialization of the unknown reconstruction $\chi_d(\boldsymbol{r})$. This would take advantage of the assumed similarity between the measurements to hasten the convergence of the second reconstruction. It is possible this technique would be more sensitive to small changes because the baseline reconstruction has already been achieved so only the difference $\delta\chi(\boldsymbol{r})$ needs to be found during the optimization. However, the sensitivity of this technique to changes between the measurements that are not hydration related, such as positioning, should be considered.

A final method looks at the differential scattered fields between measurements to generate the change in properties, $\delta\chi(\boldsymbol{r})$, itself. This technique takes advantage of the fact that the DBIM is already a differential method (the scattered field is the difference between the measured fields with and without the object) but replaces the incident field measurement with the baseline measurement. This method has the form [97]:

$$\Delta E^s(\boldsymbol{r_{rx}}) = \int_{\mathcal{D}} k_b^2(\boldsymbol{r}) \Delta\chi(\boldsymbol{r}) E(\boldsymbol{r}) G(\boldsymbol{r}, \boldsymbol{r_{rx}}) \tag{5.7}$$

If the DBIM algorithm is to be applied, $E(\boldsymbol{r})$ and $G(\boldsymbol{r}, \boldsymbol{r_{rx}})$ are estimates of the total fields and inhomogeneous Green's function, respectively. As such, a full inversion of the baseline data is required to obtain the estimates.

However, if the Born approximation is applied, the incident fields and homogeneous Green's function can be used, the inversion of the baseline measurements is not required, and the inversion can be directly applied to the differential measurements. This technique, while less accurate than the DBIM, was applied in [97] for real-time differential imaging for thermal therapy monitoring.

A presumed benefit of this technique is that errors common to both measurements should be reduced. However, it could be susceptible to errors that are different between the measurements such as object positioning.

This differential technique is outside the scope for this project but should be considered in future work.

5.3 Regularization

To generate useful solutions to ill-posed inverse problems, some *a priori* information is incorporated through a process called regularization. A very common assumption is that the object under test is smooth in some sense. Techniques like truncated SVD, and standard Tikhonov regularization achieve regularization by removing the problematic singular values at the expense of spatial resolution [84]. More involved techniques like Tikhonov regularization with Laplacian operator or total variation techniques can provide edge-preserving capabilities at some computational expense. Because hydration is a bulk phenomenon, low resolution images are adequate, and the simple smoothing regularization is applied.

5.3.1 Tikhonov Regularization

Tikohnov or additive regularization is a commonly used technique in microwave tomography. This method involves solving the following minimization [98]:

$$\boldsymbol{x} = \arg\min_{\boldsymbol{x}}(\|\boldsymbol{A}\boldsymbol{x} - \boldsymbol{b}\|_2^2 + \lambda^2 \|\boldsymbol{L}\boldsymbol{x} - \boldsymbol{x_0}\|_2^2) \tag{5.8}$$

Where $\boldsymbol{A}$ is the ill-posed linear operator, $\boldsymbol{x}$ is the desired function, $\boldsymbol{b}$ is the measured data, λ is a positive, real regularization parameter, $\boldsymbol{x}_0$ is an *a priori* estimate of $\boldsymbol{x}$ and $\boldsymbol{L}$ is the regularization matrix that implements a linear operation on $\boldsymbol{x}$.

The above minimization can be solved as a constrained linear least squares problem [99]:

$$(\boldsymbol{A}^H\boldsymbol{A} + \lambda^2\boldsymbol{L}^H\boldsymbol{L})\boldsymbol{x} = \boldsymbol{A}^H\boldsymbol{b} + \lambda^2\boldsymbol{L}^H\boldsymbol{L}\boldsymbol{x}_0 \tag{5.9}$$

In standard form, $\boldsymbol{L} = \boldsymbol{I}$ and $||\boldsymbol{L}\boldsymbol{x}||_2^2$ is a measure of the variance in the desired signal. This implements the *a priori* assumption that the distribution of $\boldsymbol{x}$ is smooth. Typical operations when $\boldsymbol{L} \neq \boldsymbol{I}$ include derivatives such as finite differences [83] or the Laplacian [43]. If no *a priori* estimate of $\boldsymbol{x}$ is used $\boldsymbol{x}_0 = \boldsymbol{0}$.

The regularization parameter λ weighs the solution between the minimization of the system of interest $\boldsymbol{A}\boldsymbol{x} - \boldsymbol{b}$ and the *a priori* assumption of the form of $\boldsymbol{x}$. If λ is too small, the solution will be under-regularized resulting in an ill-conditioned matrix and noisy results similar to the results of direct inversion in Fig. 4.11. If λ is too large, the solution is over-regularized resulting in large regularization errors. Thus, the selection of λ proves critical to optimal performance of any regularization scheme.

The impact of the regularization parameter on the inversion can be explored through the SVD. The pseudoinverse $\boldsymbol{A}^\dagger$ can be written in terms of SVD vectors $\boldsymbol{u}_i$ and $\boldsymbol{v}_i$ and the associated singular values s_i, and the least squares solution can be found by applying $\boldsymbol{A}^\dagger\boldsymbol{b}$:

$$\boldsymbol{A}^\dagger = \sum_{i=1}^{\text{rank}(\boldsymbol{A})} \frac{\boldsymbol{v}_i\boldsymbol{u}_i^H}{s_i} \tag{5.10}$$

$$\boldsymbol{x} = \boldsymbol{A}^{\dagger}\boldsymbol{b} = \sum_{i=1}^{\text{rank}(\boldsymbol{A})} \frac{\boldsymbol{v}_i \boldsymbol{b} \boldsymbol{u}_i^H}{s_i} \tag{5.11}$$

Considering eq. (5.9) and $\boldsymbol{L} = \boldsymbol{I}$, the regularized solution $\boldsymbol{x}_{\text{reg}}$ can be found using the SVD of $\boldsymbol{A}$ and λ as [84]:

$$\boldsymbol{x}_{\text{reg}} = \sum_{i=1}^{n} \frac{s_i}{s_i^2 + \lambda^2} \boldsymbol{v}_i \boldsymbol{b} \boldsymbol{u}_i^H \tag{5.12}$$

Eq. (5.12) gives some insight into the effect of different λ values. Considering an ill-posed problem, there are some $s_p \ll s_{max}$ that make the inverse ill-conditioned. If $\lambda < s_p$ the regularization will have little effect and the problem is still ill-conditioned. If $\lambda \gg s_{max}$ the solution will be dominated by regularization errors. Because the singular values/functions are analogous to the eigenvalues/vectors of the system, regularization can be seen as replacing the high frequency eigenvectors (i.e. small eigenvalues) that would destabilize the solution. This will generate useful solutions at the expense of the high frequency information in the final solution. While this helps restrict λ to $s_{max} > \lambda > s_p$ there are still many options for λ. As was illustrated in Fig. 4.10, the singular values of an ill-posed problem vary slowly so there is often no obvious λ to use.

The above analysis is readily extended to the non-standard form, $\boldsymbol{L} \neq \boldsymbol{I}$, by considering the generalized singular value decomposition of the matrix pair $(\boldsymbol{A}, \boldsymbol{L})$ and the associated generalized singular values γ_i [84].

5.3.2 Tikhonov Regularization and Non-linear Inversion

Applying standard Tikhonov regularization to a GN non-linear optimization yields the well-known Levenberg-Marquardt (LM) Method [100, 101, 102]. From the LM perspective, the regularization parameter (sometimes called the damping parameter) helps maintain the linearization (i.e. Taylor series expansion) involved in the GN method by restricting the size of the update step [101]. A commonly used procedure for LM optimization with well-posed

problems is to start with a large regularization parameter to ensure stable solutions and to decrease the regularization after each iteration until it approaches the GN method [102]. Viewing the DBIM algorithm with Tikhonov regularization from the perspective of LM optimization, it can be seen that regularization is a crucial part of regularizing both the ill-posed and non-linear aspects of the problem. Specifically, for a large contrast object the Born approximation is not an accurate solution and the inversion can yield poor results. However, over-regularizing with large λ yields solutions with smaller norms that are more likely to meet the Born approximation. This can help convergence for blind inversions.

The LM method has been used by a number of authors in microwave imaging [103, 104]. In [105], a LM scheme with a regularization parameter as an empirical function of the residual error was used. This empirical method was also used in [94].

5.3.3 L-Curve

There are many methods of determining a useful λ parameter such as empirical experience [106], discrepancy principle [107], and generalized cross validation [108]. One of the most robust is the L-Curve method [109]. This method utilizes the fact that Tikhonov regularization attempts to balance the solution to the ill-posed solution and the *a priori* assumption of the form of the solution. The norms of the solution, $\|\boldsymbol{x}_{reg}\|$, and the residuals, $\|\boldsymbol{A}\boldsymbol{x}_{reg} - \boldsymbol{b}\|$, create a characteristic L-shaped curve that can be used to balance both.

The L-curve is defined by the logarithm of the norms for various λ:

$$(\zeta(\lambda), \eta(\lambda)) = (\log \|\boldsymbol{A}\boldsymbol{x}_{reg} - \boldsymbol{b}\|, \log \|\boldsymbol{x}_{reg}\|) \tag{5.13}$$

The knee point of the parameterized curve can be found using the maximum of the standard curvature formula:

$$\kappa(\lambda) = \frac{\zeta'\eta'' - \zeta''\eta'}{((\zeta')^2 + (\eta')^2)^{\frac{3}{2}}} \tag{5.14}$$

where derivatives are with respect to λ. The derivatives can be calculated directly from the SVD and measured data [109]. The optimum regularization parameter from the L-curve λ_L is found from the maximum of the curvature function.

This formulation of the L-curve is computationally intensive because the SVD of the matrix is required [109]. While enough λ points should be used to generate a smooth L-curve (which requires solving the inverse equation many times), $\boldsymbol{u}_i$, $\boldsymbol{v}_i$ and s_i can be stored and eq. (5.12) can be applied for each λ. There are a number of alternate formulations to more efficiently compute the L-curve. An iterative technique can be applied where a few points are used and a new λ is added at the point of maximum curvature at each iteration until convergence is reached [84]. One of the most efficient L-curve methods avoids the SVD all together by applying Lanczos bidiagonalization to compute the bounds of the curvature [110].

Even with the computational requirements of a simple implementation, the benefit of the L-curve technique is that it adapts to the data. The L-curve method does not make any assumptions of the form of measurement noise [109]. The L-curve is a powerful tool for analyzing discrete ill-posed problems as it conveniently shows the entire solution space for a set of λ as all solutions must be on or above the L-curve [84]. It should be noted that the L-curve technique was developed in the context of linear inversion problems in which the discrete Picard condition holds for error free measurements [84] which may not be applicable to non-linear microwave scattering [100].

5.3.4 Proposed Regularization Scheme

The proposed regularization scheme will combine the L-curve method for determining the regularization parameter from the ill-posedness of the problem and the LM perspective of reducing any overcorrections due to non-linearity. Specifically, the following formula will be used at each iteration:

$$\lambda_k = \lambda_{L,k} + \lambda_{LM,k} \tag{5.15}$$

where $\lambda_{L,k}$ is the optimum regularization parameter found from the L-curve and $\lambda_{LM,k}$ is the kth element in the monotonically decreasing sequence:

$$\sqrt{\text{tr}(\boldsymbol{A}^H\boldsymbol{A})} \cdot p^{-k-1} \tag{5.16}$$

where $\text{tr}(\cdot)$ denotes the trace and $p > 1$ is an arbitrary real number used to control how much regularization to do and how fast to approach the L-curve solution. The trace term is used to estimate s_{max} without relying on the computationally intensive SVD. The trace of $\boldsymbol{A}^H\boldsymbol{A}$ is equal to the sum of the eigenvalues of $\boldsymbol{A}^H\boldsymbol{A}$ and the singular values of $\boldsymbol{A}$ are the square root of the eigenvalues of $\boldsymbol{A}^H\boldsymbol{A}$. Therefore, the square root of the trace will be on the same order of magnitude as s_{max}. The sequence is started at -1 to help ensure $\lambda < s_{max}$ so some regularization occurs on the first iteration but depending on the selection of p this is not always the case. The matrix trace has previously been used to determine the regularization parameter in the empirical method [42] and in the generalized cross validation [108].

λ_{LM} was chosen to satisfy the properties $\lambda_k > 0$, $1 \leq \frac{\lambda_k}{\lambda_{k+1}} \leq c$ and $\lim_{k\to\infty} \lambda_k = 0$. This sequence has been shown to be locally convergent for some non-linear ill-posed iterative GN problems [111].

The following procedure is proposed for determining the constant, p, in practice:

- Attempt the inversion using only the L-curve method by setting $p = 10^{13}$.
- Reduce p until the inversion converges (if it does).

Note that as p approaches 1 the change in λ_{LM} at each iteration will decrease slowing the rate of convergence and more iterations may be needed to reach convergence.

While the adaptive parameter will not be influenced by noise levels, the L-curve will be.

As the iterations develop and the solution approaches the actual, the noise will be more dominate but the L-curve method will be used.

This technique represents a novel fusion of the standard approaches to determining the regularization parameter in microwave inverse scattering. The L-curve method has been used in [43] and LM techniques have been used in [104, 94]. To the author's knowledge the use of a monotonically decreasing regularization parameter as outlined in [111] for microwave imaging is also novel.

5.3.5 Validating Non-Linear Inversion

The DBIM non-linear inversion technique and the proposed regularization scheme will now be explored through an example inversion. A lossless, homogeneous elliptical cylinder of diameters λ by $\lambda/2$ with a 3:1 contrast ratio is imaged using 12 transmitters and receivers on a circle of diameter 2λ. The tomographic setup as described is shown in Fig. 5.1. The inversion is done at 1 GHz with the data generated using a discretization of 0.5 cm and the inverse is done on a coarser grid of 1.0 cm. The inversion is terminated after 20 iterations. The empirical method is applied with $p = 2$.

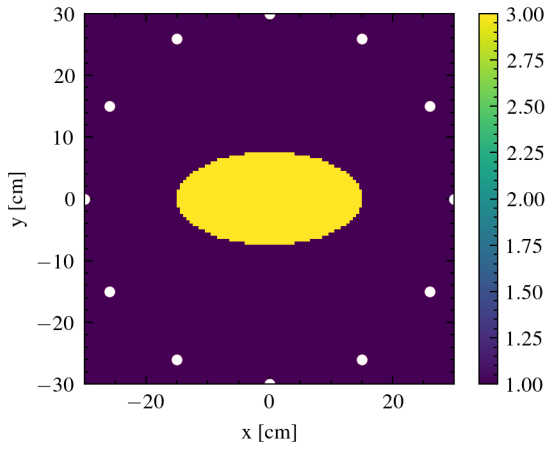

Figure 5.1: Homogeneous elliptic cylinder in free space.

Fig. 5.2 shows the reconstructed permittivity using the L-curve method, the decaying series, and the hybrid method. As shown, the L-curve method fails to produce a useful

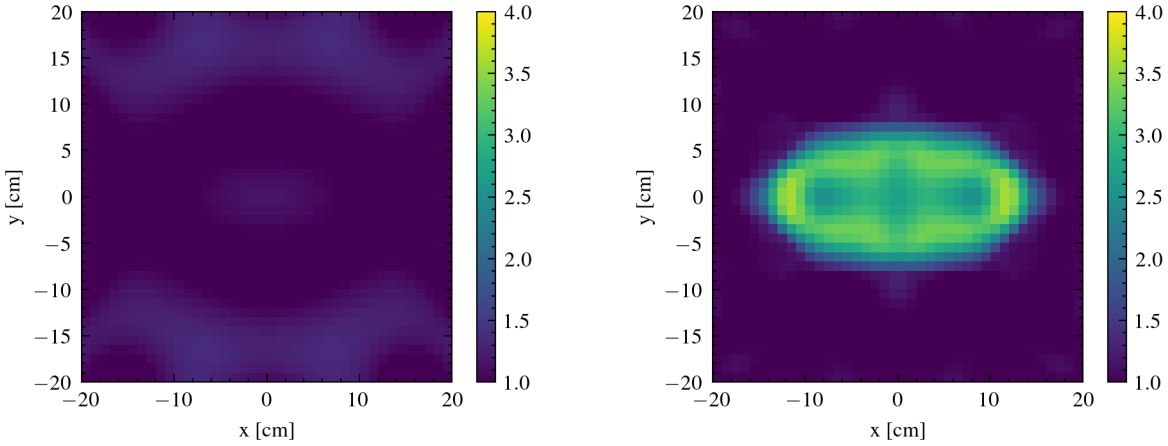

(a) Standard L-Curve approach.

(b) Decaying series.

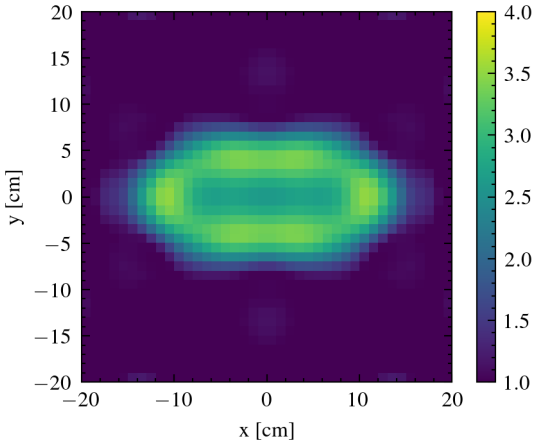

(c) Hybrid method.

Figure 5.2: Reconstructed homogeneous elliptic cylinder.

solution, but the series and hybrid methods produce similar, useful results. The addition of the L-curve parameter has only a subtle impact on the final reconstruction. It is expected that when measurement errors are present the inclusion of the L-curve parameter will have a larger impact.

The standard L-curve technique fails to converge to a useful solution after only one iteration before the residuals increase. Fig 5.3 shows the L-curve and associated curvature for the first iteration of the inversion. The algorithm successfully picks the point of maximum curvature however the L-curve does not match the ideal "L" shape and the regularization parameters fail to yield useful results.

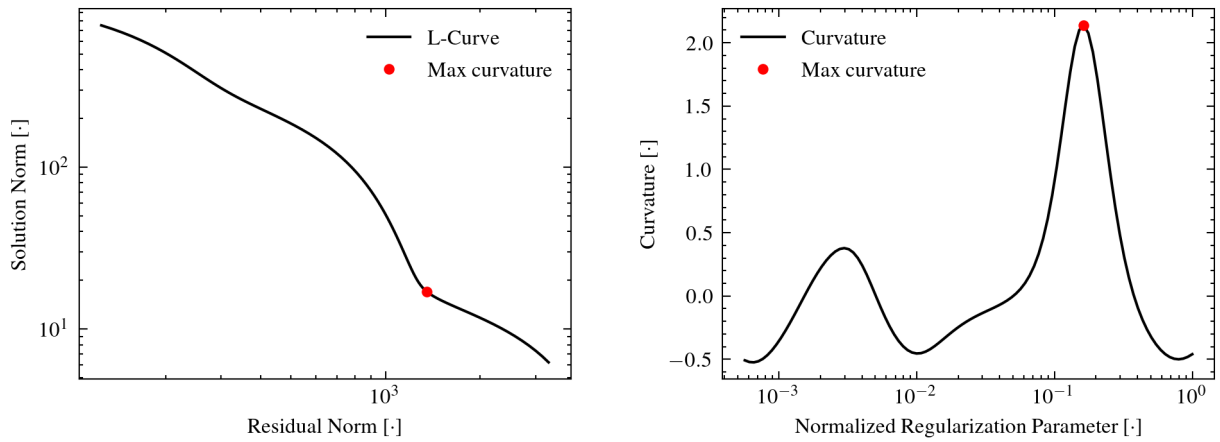

(a) (b)

Figure 5.3: L-curve and associated curvature for first iteration of homogeneous elliptic cylinder inversion.

Fig. 5.4 shows the associated regularization parameters using the L-curve, decaying series, and the hybrid method. As can be seen the decaying series initially introduces much more regularization than the L-curve method. The regularization parameter decays until the L-curve (max curvature) parameter is used.

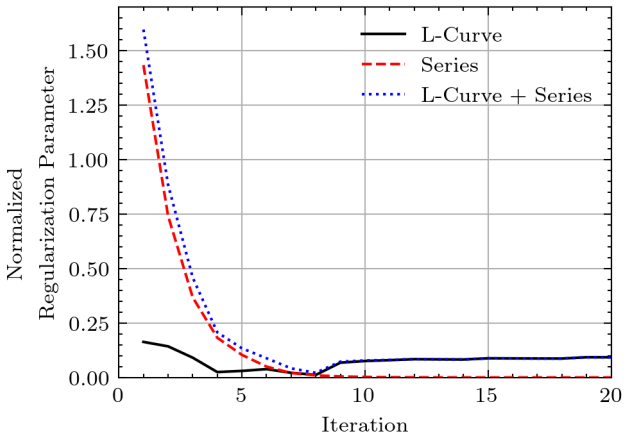

Figure 5.4: Regularization parameters from L-Curve, decaying series, and hybrid method.

Table 5.1: Demographic information for realistic models.

Name	Age [years]	Height [m]	Weight [kg]	BMI [kg/m^2]	Forearm Width [cm]
Duke	34	1.77	70.2	22.4	7.0
Ella	26	1.63	57.3	21.6	6.1

5.4 Forearm Models

The application of the DBIM with Tikhonov regularization for detecting changes in hydration is validated through a model of hydration changes applied to realistic forearm model.

For an *in silico* validation of the hydration monitoring technique, accurate forearm models are used. The two full body, repositionable models, Duke and Ella (IT'IS Foundation, Zurich, Switzerland), were generated from tissue segmented MRI images [112]. A 2D cross-section of the forearm, Fig. 5.5a, is taken at the midpoint between the olecranon and ulnar head at a 1 mm voxelization. Table 5.1 shows the demographic information on the models.

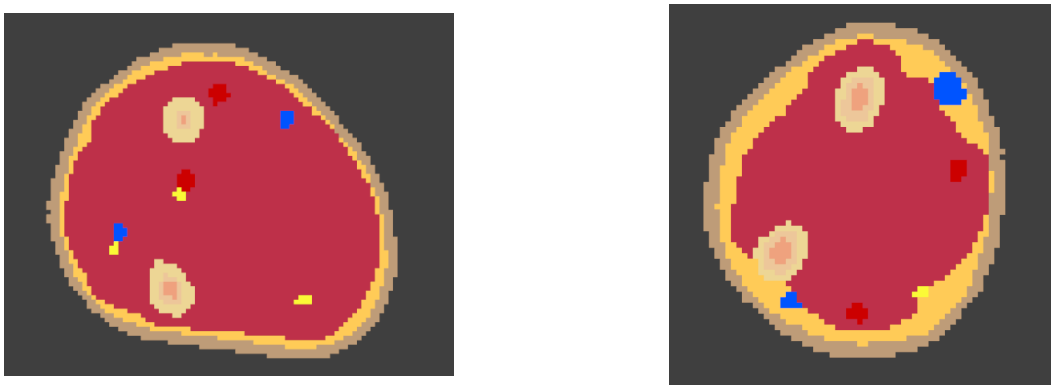

(a) Duke model.

(b) Ella model.

Figure 5.5: 2D cross section of Duke and Ella forearm models. The blue, dark red, and yellow voxels represent veins, arteries, and interstitial fat, respectively. Images not to scale.

The system will be designed using the Duke model with nominal properties, Table 5.2. The Ella model will be used to validate the final design.

Table 5.2: Nominal dielectric properties for Duke model at 500 MHz.

Tissue	ε_r [·]	σ [S/m]
Blood	63.5	1.4
Muscle	57.0	0.77
Skin	42.6	0.72
Bone (cancellous)	21.5	0.25
Bone (cortical)	12.9	0.10
Fat	11.6	0.09

5.5 System Design

A standard tomographic setup will be used for the proof of concept. The standard tomographic setup with a circular measurement surface, matching medium, and antennas operating at a distance from the object under test is widespread in the literature [11, 113, 10] because of its flexibility to image objects of various sizes, relative ease at replacing the sensors, and ability to change the matching medium. This setup also lends itself well to pseudo-3D imaging as reconstructions can be done using 2D slices at various sensor heights [67]. Systems operating with antennas in direct contact with the OUT have had limited use in tomographic systems because of modelling errors, more restrictive sensor design, and general smaller size limiting the number of sensors.

The general setup of the tomographic system will first be discussed, then the specific background medium, operating frequency, and number of sensors will be optimized.

5.5.1 System Setup

The physical size of the system will be determined by the maximum expected arm size. Considering the separation distances found in Chapter 3 and the wrestler study [8] the maximum antenna separation distance found was 7.5 cm. This value is comparable to the forearm size of women with high body mass index [114]. As such the largest imaging domain is set to be 10 cm x 10 cm to accommodate the irregular shape of the forearm and positioning

errors. This is about 3 cm smaller than the largest imaging domain of the system used to image forearms in [11] and generally smaller than other tomographic systems [113, 10]. From this imaging domain size, the measurements must be taken on a circle with $r_{\text{rx}} \geq 5\sqrt{2}$ cm so a radius of 8 cm will be used. The Duke model presents a forearm in line with the largest found during the wrestler [8] and Ramadan studies. As can be seen in Fig. 5.5a, the Duke model has a thin subcutaneous fat layer. Fig. 5.6 shows the permittivity of the Duke forearm model in the proposed tomographic setup.

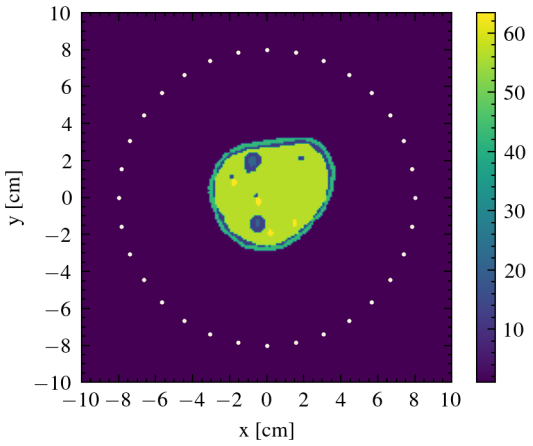

Figure 5.6: Duke forearm permittivity model in tomographic system with free space background.

The monostatic data is excluded from all reconstructions. In a physical system, the monostatic (S_{11}) data represents a large increase in the measurement system complexity while adding little to the quality of the reconstruction.

The measured data is generated on a grid discretized to 1 mm x 1 mm cells (80 x 80 grid) and the inverse problem is done with 2.5 mm x 2.5 mm cells (32 x 32 grid). The smaller discretization is used generate accurate measurements while the inverse problem is computed on a coarser grid to ensure reasonable computation speed. The reconstructed images are resized to 80 x 80 using bicubic interpolation to enable proper comparison. Note that while different discretizations are used in the forward and inverse problems, the inverse grid is essentially a subsampling with every 5^{th} element aligning exactly. This can cause some errors to cancel in the forward and inverse problem generating overly optimistic results. However,

for the purpose of evaluating the relative performance with different design parameters this is adequate and will be remedied when evaluating the final system.

5.5.2 Permittivity Metrics

The ultimate goal of the hydration assessment technique is to detect changes in the real permittivity of the forearm. As illustrated in [7], permittivity is more sensitive than condutivity to changes in hydration. To this end two metrics are defined: the bulk permittivity $\varepsilon_{\text{bulk}}$, eq. (5.17), which is the mean permittivity over the forearm and the average permittivity ε_{avg}, eq. (5.18) which is the mean permittivity over the image.

$$\varepsilon_{\text{bulk}} = \frac{1}{N} \sum_{\mathcal{D}_{arm}} \varepsilon_r' \tag{5.17}$$

where $\mathcal{D}_{arm}$ is the forearm cross section. In the case of reconstructed images, the forearm cross section will be estimated by segmenting the images using a technique that will be discussed in the coming sections.

$$\varepsilon_{\text{avg}} = \frac{1}{N} \sum_{\mathcal{D}} \varepsilon_r' \tag{5.18}$$

where the sum is over the whole image domain $\mathcal{D}$. The permittivity metrics will be used as a final design metric when evaluating the sensitivity of the system to noise.

5.5.3 System Optimization

An optimized system design is presented for hydration monitoring. An *in silico* analysis of important system parameters ($\varepsilon_{r,b}$, frequency, number of receivers, and system size) is an important first step for defining the expected performance of microwave tomography for hydration assessment.

A physical implementation of the tomography system would have to account for non-idealities related to antenna patterns, mutual coupling between the transmitters and neigh-

boring antennas, and field interactions with receivers and system boundaries. A physical implementation would also have to manage the complexities related to the measurement system such as signal isolation, sensor feeding, and multiplexing the transmitters and receivers. While these considerations are outside the scope of the current work, they will be accounted for when choosing the design parameters. For example, the highest conductivity medium that produces good quality reconstructions will be selected for the matching medium as a higher conductivity medium is often used to reduce the mutual coupling and field interactions in real systems [69].

There are three critical microwave tomography parameters to decide: frequency, number of receivers, and matching medium. The matching medium is chosen for practicality and loss, the frequency will be maximized to improve resolution, and the number of receivers will be minimized to reduce measurement and simulation complexity. First, the matching fluid will be designed using a large number of receivers, $N_{rx} = 32$, and a low frequency, $f = 500$ MHz. A large number of receivers will provide the best quality data while the low frequency will provide more stable solutions. Once the matching medium is optimized, the frequency will be selected, then finally the number of receivers will be optimized. The matching medium is chosen to optimize first because it has the largest impact on $\chi(\boldsymbol{r})$ which is the function of interest. While the properties of both the matching medium and the biological tissues are dispersive, the change across the frequencies of interest (0.3 MHz to 3 GHz) will be much smaller than the change in contrast with different matching media. *In silico*, the number of receivers is expected to determine the impact of noise on the final reconstructions. In practice, the matching medium and frequency would have an impact on the noise level of the measurements by influencing the amount of attenuation and coupling.

The quality of reconstructions will be quantified using mean square error (MSE), eq. (5.19), in the complex permittivity. While the MSE is unavailable during real measurements, it provides a useful metric for comparing images *in silico*.

$$\text{MSE} = \sqrt{\frac{\sum\limits_{\mathcal{D}_{\text{arm}}} |\varepsilon_{\text{reco}} - \varepsilon_{\text{actual}}|^2}{\sum\limits_{\mathcal{D}_{\text{arm}}} |\varepsilon_{\text{actual}}|^2}} \tag{5.19}$$

where $\varepsilon_{\text{reco}}$ is the reconstructed complex relative permittivity, $\varepsilon_{\text{actual}}$ is the actual relative permittivity, and $\mathcal{D}_{arm}$ is the cross section of the forearm. The images are segmented using the input model to compare the reconstructed values over the cross section of the forearm excluding the background.

The reconstructions are terminated when $RRE = 1\%$, $RRE_k > RRE_{k-1}$ or after 20 iterations. No noise is added to measurements when optimizing the matching medium and frequency, but noise will be added when optimizing the number of receivers. In this context, the added noise represents any of the errors possible during a real measurement (i.e. thermal noise, receiver placement errors, etc.) including errors between the model and real signal propagation.

Matching Medium

The optimum matching medium is found by doing a parametric analysis of the real permittivity $1 \leq \varepsilon'_{r,b} \leq 80$ representing permittivities from free space to water and imaginary permittivity from $0 \leq -\varepsilon''_{r,b} \leq 45$ representing conductivities from free space to a saline solution [69]. A total of 120 different media are simulated. All reconstructions are done with regularization parameters selected using both the L-curve method and the hybrid method with constant $p = 2$.

Fig. 5.7 shows the mean square error in the scattered fields and reconstructed images. The adaptive regularization achieves similar quality reconstructions as the standard L-curve method for well matched media. However, for larger contrasts the adaptive regularization outperforms the standard L-curve. Both techniques show poorer results with both low and high permittivity media where the object presents a higher contrast. There is a broad minimum shown with both techniques illustrating stable performance. Fig. 5.8 shows the

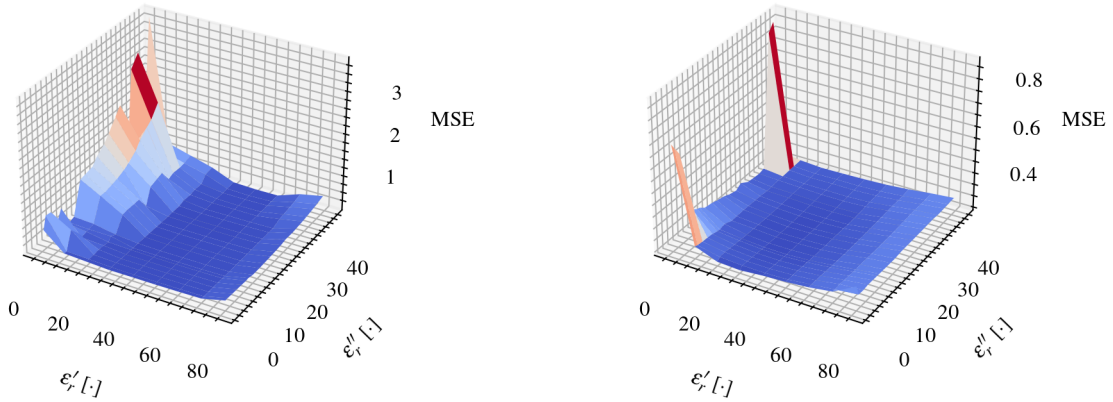

(a) Using standard L-curve method.

(b) Using adaptive method.

Figure 5.7: Mean square error of Duke forearm reconstructions with various background media.

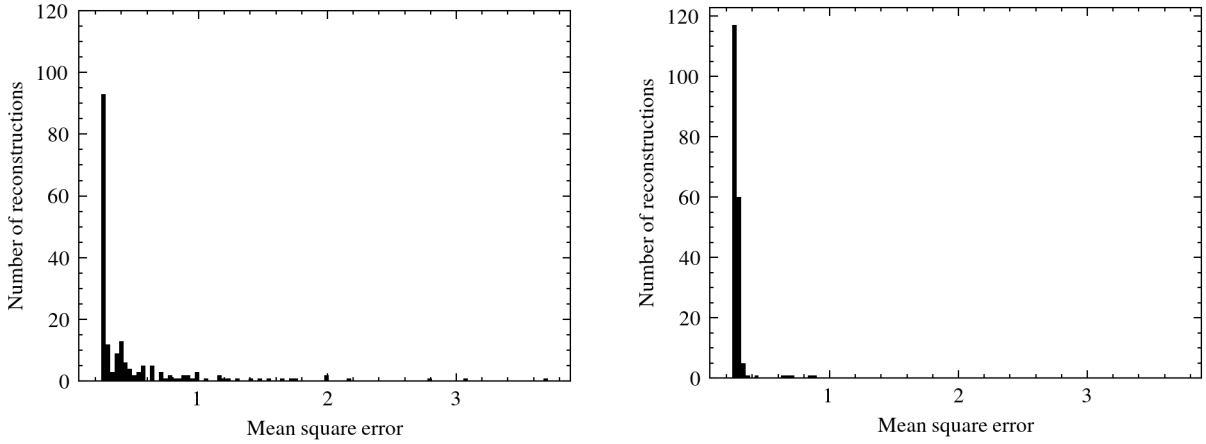

(a) Using standard L-curve method.

(b) Using adaptive method.

Figure 5.8: Histograms of mean square error for Duke forearm reconstructions with various background media.

frequency of the MSE values. Table 5.3 shows the minimum MSE, associated optimum ε_r, and the percent of reconstructions to reach convergence ($RRE < 1\%$). The adaptive regularization improves the number of tested high contrast cases that reach convergence.

Considering the design criteria, the final media is selected to be $\varepsilon_r = 35 - j30$ ($\sigma = 0.83$S/m). The final reconstructions with this medium are shown in Figs. 5.9 and 5.10 with cross-sections along the x-axis and through the bones in Fig. 5.11 and 5.12. The methods using the L-curve and adaptive parameter selection generate similar results. Qualitatively,

Table 5.3: Statistics on matching medium parameter sweep with Duke forearm.

Regularization	Minimum MSE [·]	Optimum ε_r [·]	Convergence [%]
Standard Tikhonov	0.24	40-j30	93.3
Adaptive	0.25	30-j0	99.1

the adaptive technique looks to provide slightly smoother solutions. The relatively high MSE can be attributed to the smooth solutions generated using the Tikhonov regularization and the relatively low frequency. While a more accurate reconstruction would be beneficial for accurately determining absolute properties, this technique will be adequate for change detection.

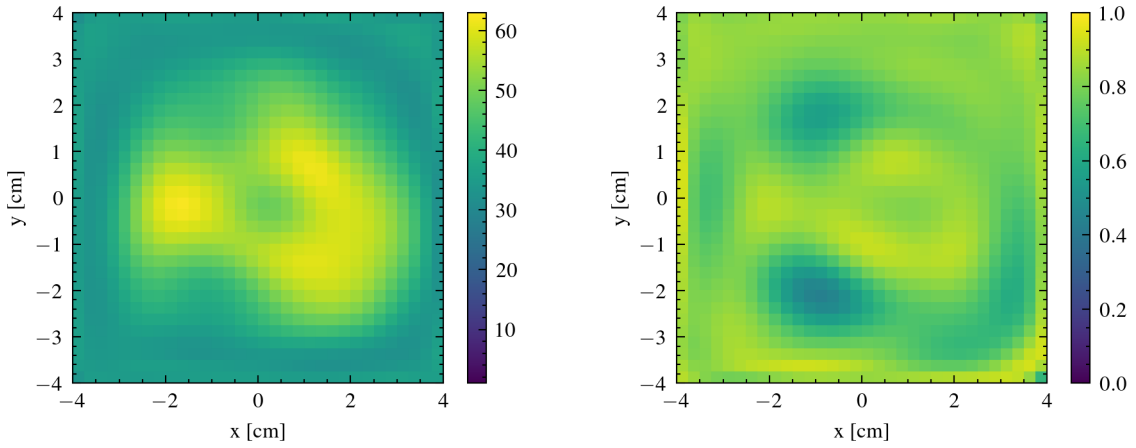

(a) Relative permittivity.

(b) Conductivity.

Figure 5.9: Reconstructed forearm in optimum background medium using standard L-curve method.

A real permittivity on the lower side of the minimum is selected to better match various forearm compositions. In [11], a high permittivity of $\varepsilon_r' = 77$ is used, and the system had markedly worse performance imaging forearms with larger subcutaneous fat layers. The associated study of different matching fluids [69] focused on optimizing loss with different concentrations of saline solutions used. From Fig. 5.7 the reconstruction of the forearm appears to be more sensitive to the real permittivity. However, much of the benefit of increased loss is related to reducing real measurements errors which are outside the scope

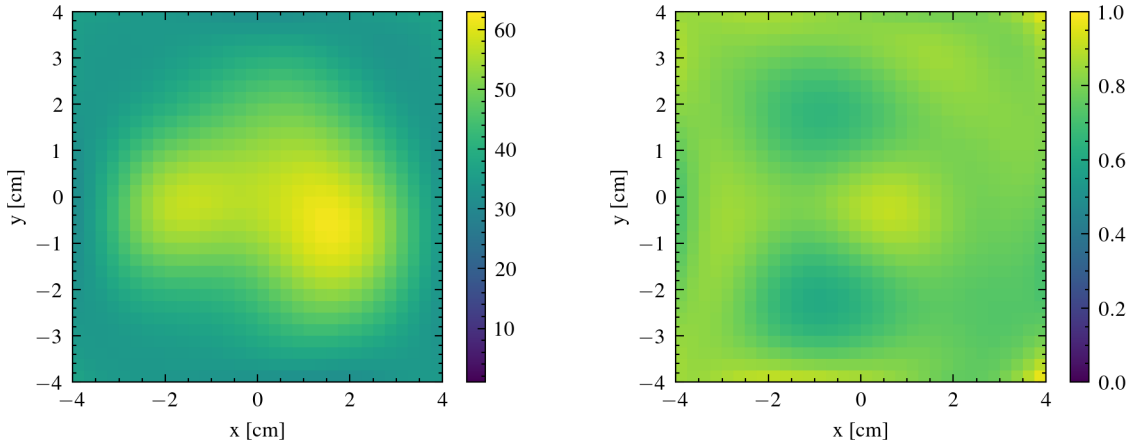

(a) Relative permittivity. (b) Conductivity.

Figure 5.10: Reconstructed forearm in optimum background medium using adaptive method.

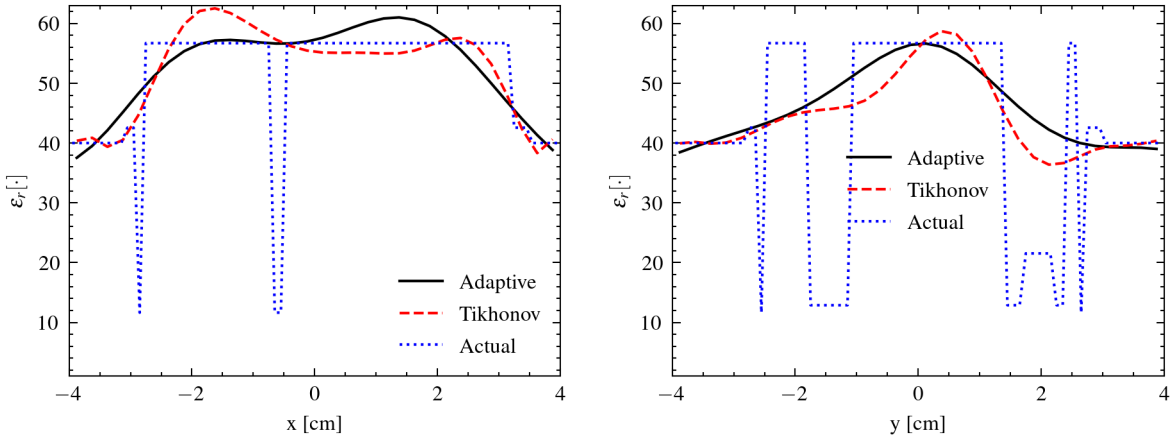

(a) Cross-section through y = 0 cm. (b) Cross-section through x = -1 cm.

Figure 5.11: Cross-section of reconstructed forearm permittivity in optimum background medium at 500 MHz compared to actual values.

of this current work. The proposed conductivity falls within in the optimum conductivity range found in [69].

To practically implement this matching medium at 500 MHz a 9:1 mixture of glycerin and water can be used [115]. Because the loss of glycerin-water mixtures is low below 1 GHz [115], salt may need to be included to achieve $\sigma = 0.83$ S/m. Glycerin-water mixtures provide a cheap and safe matching medium that can be mixed in different ratios to generate real permittivities between 20-80 in the region from 0.1-3 GHz [115]. However, the conductivity

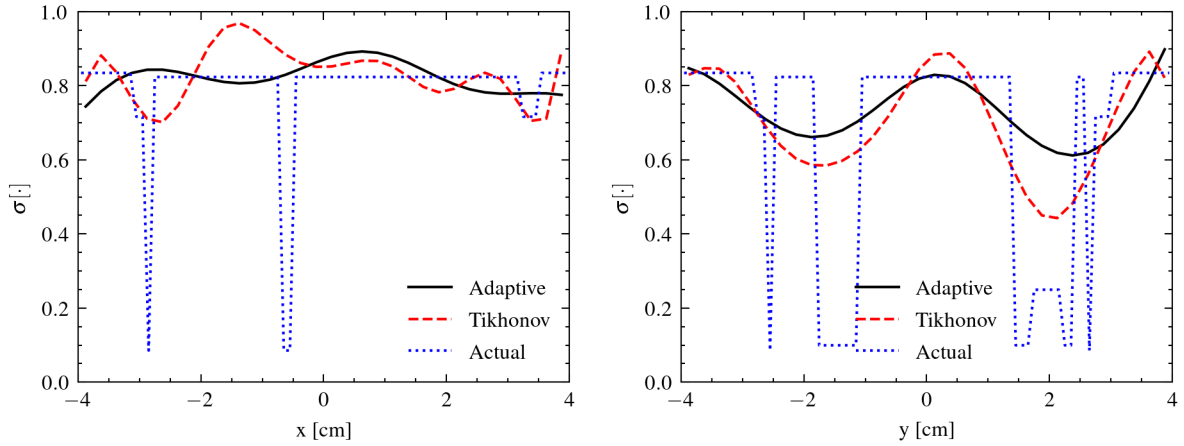

(a) Cross-section through y = 0 cm.

(b) Cross-section through x = -1 cm.

Figure 5.12: Cross-section of reconstructed forearm conductivity in optimum background medium at 500 MHz compared to actual values.

begins to increase rapidly after 2 GHz. It is also important to note that glycerin is highly dispersive in this frequency range.

Frequency

Next, the frequency is analyzed using the optimum background medium. The frequency of the inversion influences many important parameters such as properties of the OUT, properties of the background medium, electrical size, effective contrast, and image resolution. From diffraction tomography theory, the maximum image resolution is generally considered to be the Rayleigh resolution of $\lambda/4$ for near-field imaging [116]. However, when non-linear quantitative microwave tomography is applied there is experimental evidence of so-called super resolution with up to $\lambda/30$ [117]. Thus, it is important to maximize frequency in order to improve image resolution. However, the attenuation in lossy materials increases with frequency, placing large demands on the sensitivity of the measurement devices [69] and the non-linear and ill-posed aspects of the inverse scattering problem get worse. Generally, for a given contrast function inversions get more difficult with increasing frequency [68]. This can be explained via the larger phase changes through objects as well as the larger scattering magnitude.

The frequency is swept from 0.3 - 3 GHz in 100 MHz steps. The dispersion of the forearm is accounted for using the Debye model. The background medium is kept at the previously found optimum $\varepsilon_r = 35 - j30$ (conductivity $0.17 - 5.0$ S/m). Again, regularization parameters are determined by both the standard L-curve and the adaptive scheme with $p = 2$.

Fig. 5.13 shows the MSE of the reconstructed complex permittivity as well as the RRE of the scattered fields. As can be seen from the RRE plots, the standard L-curve technique fails to generate convergence for frequencies greater than 0.9 GHz resulting in poor MSE. The MSE of the L-curve method increases exponentially until the initial Born approximation is so poor that only one or two iterations are run before residuals increase and the algorithm is terminated. Below 0.6 GHz the L-curve and adaptive approaches have similar results. The MSE of the adaptive approach improves with frequency until 1.4 GHz except for spurious results at 0.9 and 1 GHz.

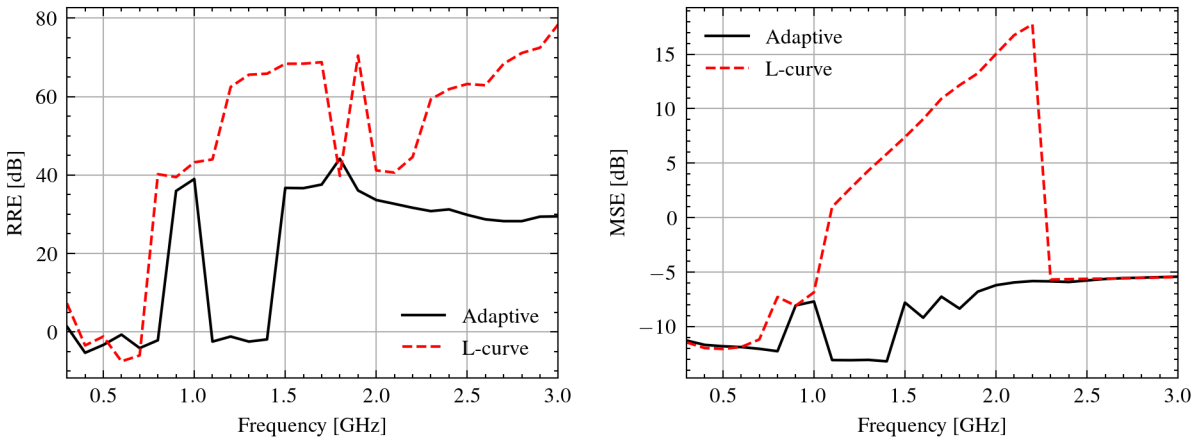

(a) (b)

Figure 5.13: MSE in reconstructed complex permittivity and relative residual error of scattered fields for Duke forearm in optimum medium vs frequency.

From this analysis 1.2 GHz is selected because it is a higher frequency that converges reliably. Fig. 5.14 shows the resulting reconstruction using the L-curve method and Fig. 5.15 shows the reconstruction with the adaptive approach. Figs. 5.16 and 5.17, show cross-sections of the reconstructed properties through the x-axis and through the forearm bones. As can be seen the reconstruction using the L-curve fails to converge to a solution with phys-

ically meaningful properties. The adaptive reconstruction converges to accurate properties with the bones identifiable.

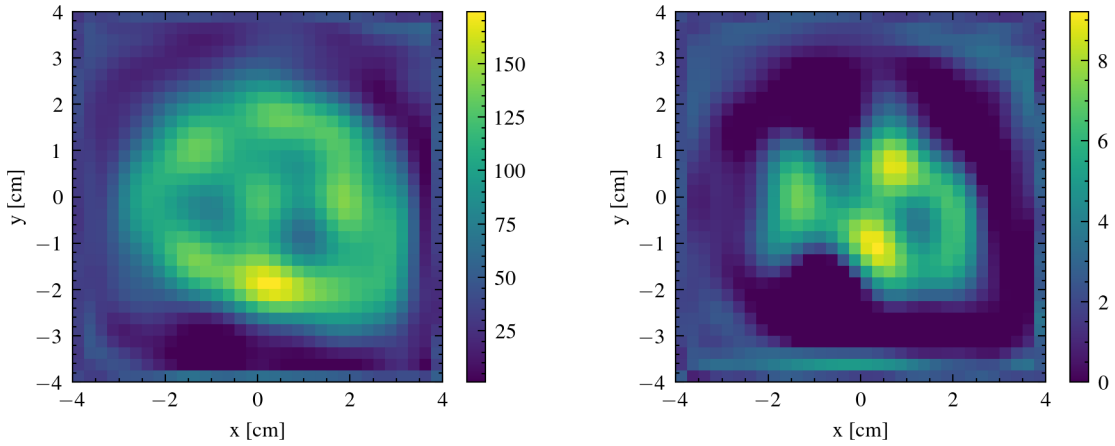

(a) Relative permittivity. (b) Conductivity.

Figure 5.14: Reconstructed forearm properties for Duke model in optimum background medium at 1.2 GHz using standard L-curve technique.

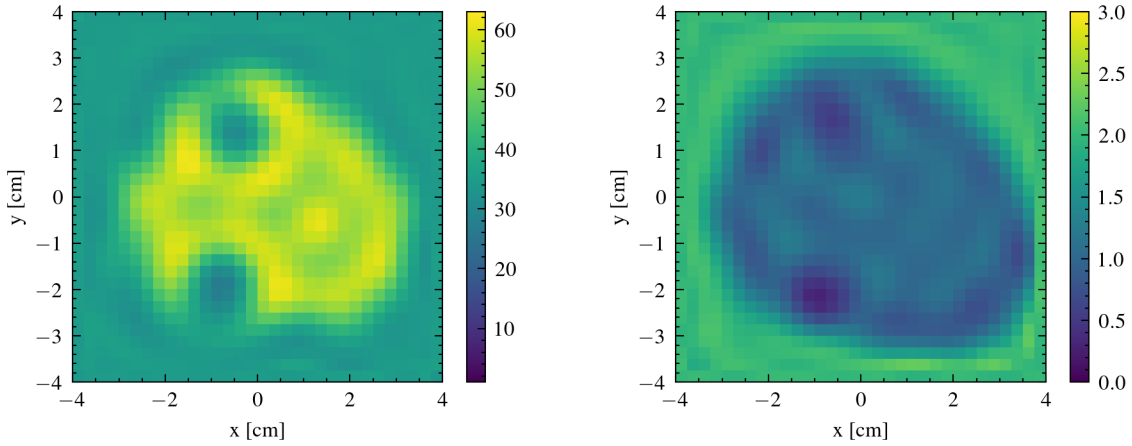

(a) Relative permittivity. (b) Conductivity.

Figure 5.15: Reconstructed forearm properties for Duke model in optimum background medium at 1.2 GHz using adaptive technique.

The matching fluid $\varepsilon_r = 35 - j30$, can be implemented at 1.2 GHz using a 70-80% glycerin, 30-20% water solution [115]. Salt may be required to increase the conductivity to the 2 S/m value.

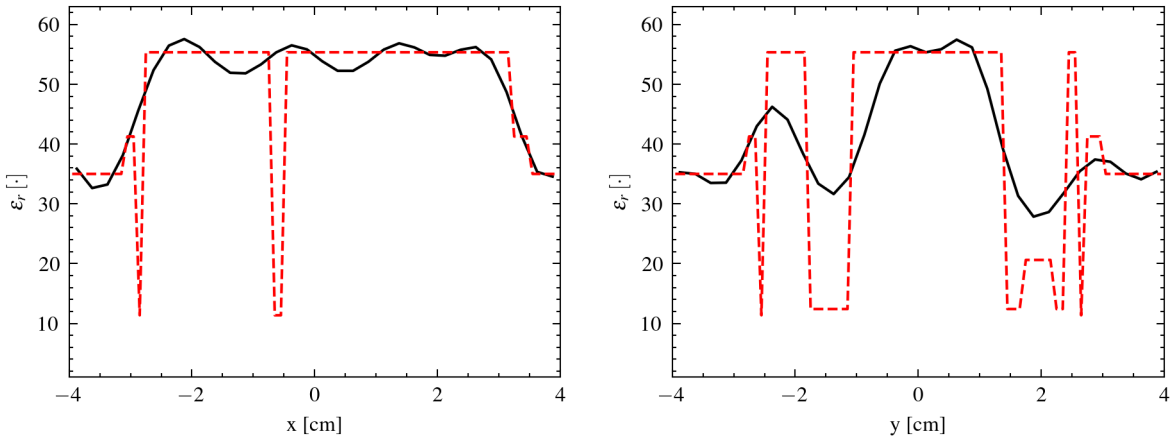

(a) Cross-section through y = 0 cm. (b) Cross-section through x = -1 cm.

Figure 5.16: Cross-section of reconstructed forearm permittivity in optimum background medium at 1.2 GHz using adaptive technique compared to actual values.

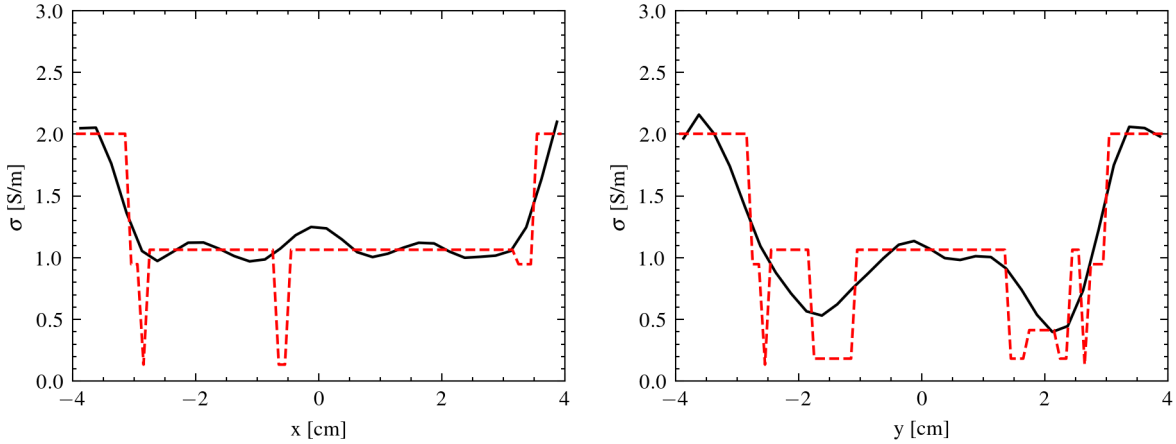

(a) Cross-section through y = 0 cm. (b) Cross-section through x = -1 cm.

Figure 5.17: Cross-section of reconstructed forearm conductivity in optimum background medium at 1.2 GHz using adaptive technique compared to actual values.

Number of Receivers

Finally, the number of receivers and transmitters are optimized. For a practical application, it is important to minimize the number of receivers to reduce the measurement complexity. However, using fewer receivers reduces the information available which limits the number of unknowns that can be reconstructed and reduces the quality of the reconstruction. As a first point, if all bistatic and monostatic data is used, the number of potentially linearly

independent measurements is $N_{rx}^2/2$ because of the reciprocal nature of the measurements. In practice, this reciprocity is not guaranteed because of noise and measurement errors.

The sampling requirements for accurate microwave inversion is a large topic of study in the field [118, 119, 120]. Two commonly cited rules of thumb are $\lambda/2$ to satisfy the Nyquist sampling theorem and $\lambda/4$ [120]. However, determining the exact sampling requirements for an arbitrary object is not a trivial problem as it gets to the foundation of the ill-posed problem. In [119], the amount of information available in the scattered fields is examined through the SVD of simple models to yield the number of recoverable unknowns for incident plane waves as $16\pi(\frac{a}{\lambda}^2(\frac{\pi}{2}))$ where a is the measurement surface radius. However, the authors state that for near-field imaging the maximum information that can be recovered is governed instead by the signal-to-noise ratio [119].

For the system as designed so far, the wavelength in the background medium is 4.2 cm. With a measurement surface of radius 8 cm, Nyquist sampling rate is almost satisfied with $N_{rx} = 24$. Here, the optimum number of receivers will be determined empirically. The number of receivers will be swept through the series $N_{rx} = 32, 24, 16, 12, 8, 4$.

The noisy data is generated from the noiseless data using eq. (5.20).

$$\tilde{\boldsymbol{E}}^s = \boldsymbol{E}^s + \max(\boldsymbol{E}^s)B(\alpha + j\beta) \tag{5.20}$$

where $\tilde{\boldsymbol{E}}^s$ is the noisy measurement, $\boldsymbol{E}^s$ is the noiseless measurement, B is a scalar defined in percent, and α, β are random variables drawn from a zero mean normal distribution with variance 0.33. This means roughly 99.7% of the samples are between ± 1. This formula is adapted from [43] where 5% noise is added when inverting synthetic leg data.

Three noise levels will be examined $B = 1, 5, 10\%$ corresponding to 40, 26, and 20 dB signal-to-noise ratios in addition to the noiseless case. Ten measurements and inversions will be done at each noise level to characterize the effect of the noise. The residual termination threshold is set to the noise level.

Fig 5.18 shows the minimum, mean, and maximum of the final RRE and MSE of the

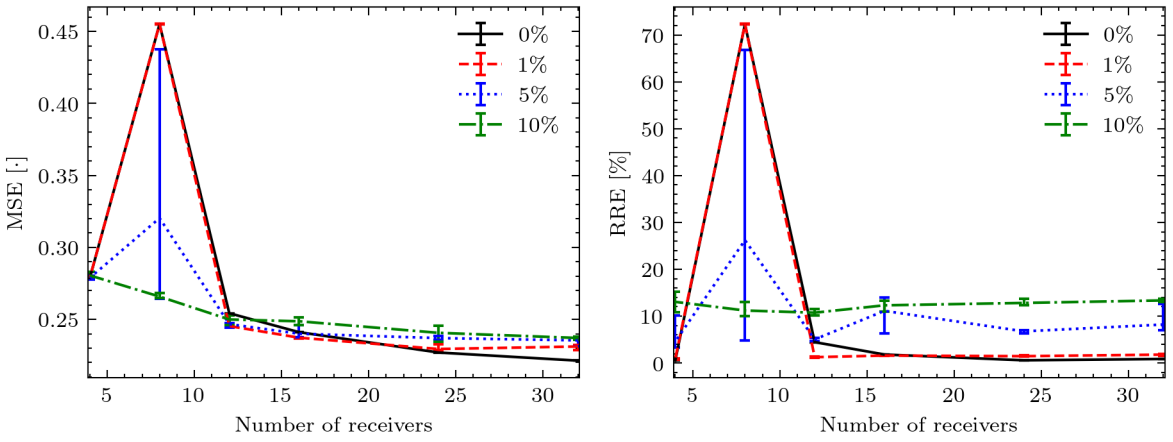

(a) (b)

Figure 5.18: Mean square error in reconstructed complex permittivity and relative residual error of scattered fields for Duke forearm at 1.2 GHz using adaptive technique with different noise levels and number of receivers. Error bars denote the minimum and maximum values

reconstructions for each number of receivers at each noise level. The reconstruction algorithm is stable for different frequencies and number of receivers. The RRE generally increased a few percentage points before the threshold. At $N_{rx} = 8$ the algorithm fails to converge to a reasonable solution for the cases with less noise. This is hypothesized to have occurred because of the different shape of the L-curve and different regularization parameters. The algorithm converges for $N_{rx} = 4$ because there are so few scattered field measurements, they can be matched easily even with poor MSE. Fig. 5.18 shows the MSE increases with fewer receivers and with more noise. Considering the results with good convergence, the marginal impact on the MSE of decreasing the number of receivers is less for higher noise measurements. Thus, in a practical implementation it is important to minimize noise to take full advantage of any increase in the number of receivers.

To evaluate the effect of noise on the $\varepsilon_{\text{bulk}}$ metric a segmentation technique is required to isolate the forearm response from the background medium. *In silico*, the actual model can be used to segment the reconstructed image as has been done with the MSE calculations, however this technique cannot be applied in practice. To isolate the forearm response, real permittivity image is sharpened using the Laplacian, squared, then the resulting image is

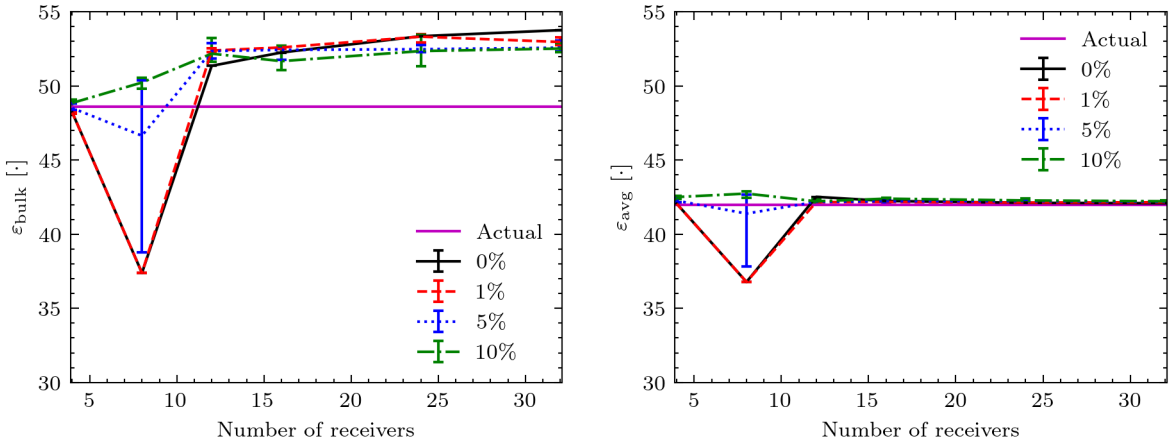

Figure 5.19: Permittivity estimates ε_{avg} and $\varepsilon_{\text{bulk}}$ with different number of receivers and noise levels. Error bars denote minimum and maximum values.

thresholded to its mean. More details and examples of this technique being applied to the images generated here can be found in Appendix C. The threshold chosen is arbitrary but based on the contrast with the background medium and relative size of the forearm in the image. More advanced techniques such as K-means clustering can be applied to make this more robust [121]. The bones are often left out of the segmented image. This is advantageous because bones are a relatively low water content tissue when compared to muscle (see Table 6.1) so the changes in properties due to hydration are expected to be larger in muscle than bone. The effect of larger subcutaneous fat layer will be examined later.

Using this technique and the image mean, the effect of noise and number of receivers on permittivity estimates is examined. Fig. 5.19 shows the estimated bulk and average permittivities as a function of number of receivers and noise.

From Fig. 5.19 it can be seen that the average permittivity is less sensitive to noise but is biased by the inclusion of the background medium. The bulk permittivity estimate is more sensitive to noise level. The bulk permittivity estimate is larger than the actual bulk permittivity of the forearm model but less than the permittivity of the muscle ($\varepsilon_r = 57$). The higher bulk permittivity is explained by the exclusion of the bones from the calculation due to the image segmentation.

Considering the MSE and mean permittivity results, $N_{rx} = 12$ is chosen as it had stable

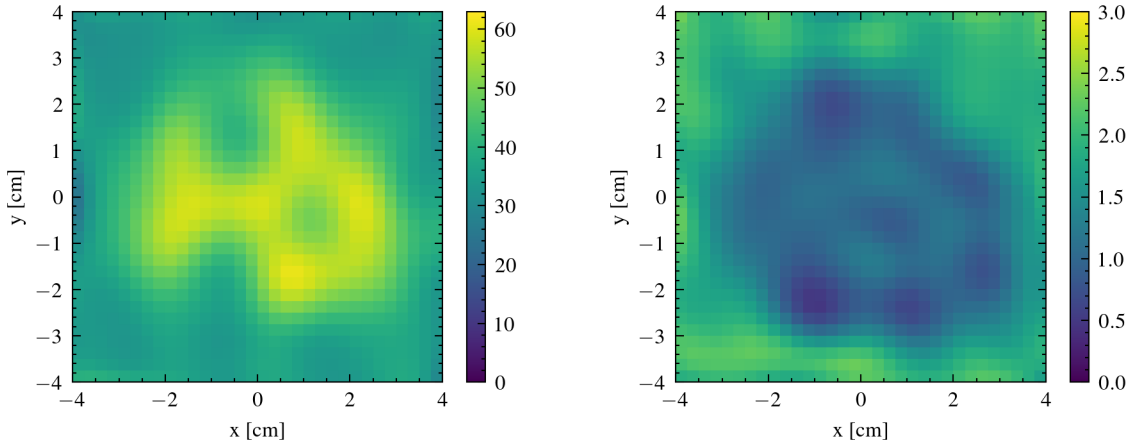

(a) Relative permittivity. (b) Conductivity.

Figure 5.20: Reconstructed Duke forearm model with optimized design and 5% noise.

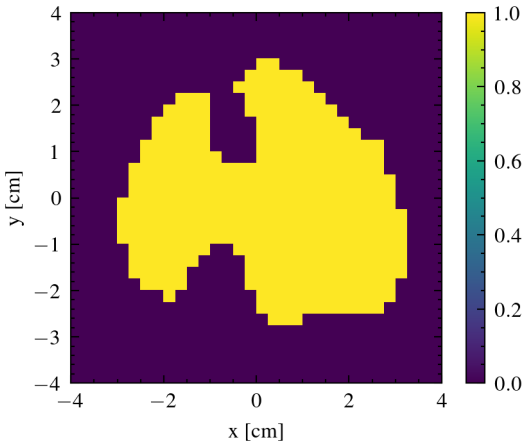

Figure 5.21: Segmented image for Duke forearm in optimized design and 5% noise.

reconstructions that were only marginally worse than those with more receivers. Fig. 5.20 shows a final reconstruction with 5% noise. From this figure the forearm is easily identifiable but with worse resolution than the noiseless, $N_{rx} = 32$ case (Fig. 5.15). Fig. 5.21 shows the associated segmented image used to define the forearm cross section. As can be seen, the bones are excluded from the segmented image. $N_{rx} = 12$ can be considered the worst acceptable case with more receivers generally providing better results. In the discussion of the thresholding found in Appendix C some reconstructions with different noise levels and more receivers can be found.

5.6 Chapter Conclusion

In this chapter, the details of the tomographic THA technique are outlined, and the system designed. A standard DBIM algorithm with Tikhonov regularization is applied to solve the non-linear ill-posed problem associated with the microwave scattering. To improve convergence for high contrast objects a simple empirical method based on LM techniques is proposed to enforce the Born approximation linearization. A standard tomographic system is designed with the aid of a realistic forearm model. First the matching medium is optimized to maximize convergence and loss using low frequencies and many antennas. Next the frequency is increased to improve resolution. Finally, the number of transmitters and receivers is reduced to increase the ease of application. In the process, permittivity metrics are defined to quantify the changes in permittivity seen in reconstructed images. The THA technique and accompanying system will be further validated in the next chapter.

Chapter 6

In Silico Validation of Tomographic Hydration Assessment

In this chapter the previously outlined techniques for THA and the designed THA system are validated using *in silico* models. First, a previously developed hydration model [7] is used to generate realistic changes in properties due to changes in hydration is introduced. This model is then applied to two forearm models and the THA methods are applied to characterize the technique's sensitivity to clinically relevant changes in hydration. Next the effect of measurement noise will be analyzed, and finally the effect of positioning errors will be examined.

6.1 Hydration Model

The hydration model is based on [7, 8] in which changes in weight due to water loss generate changes in dielectric properties of tissues based on their Debye models and water content. This work was used in an ultrawideband application in the 1-10 GHz range. For greater stability in the reconstructions, lower frequencies in the 300 MHz - 3 GHz range will be used. As a result, the analysis carried out in [7] will be adapted to the lower frequency range. This is especially important as biological tissues have larger dispersion below 1 GHz.

The physiological basis for using dielectric properties at microwave frequencies to detect changes in hydration is the close relationship between the dielectric properties of tissues and their water content [9]. The dielectric properties of a wide range of human tissue have been measured from 10 Hz to 20 GHz by Gabriel and Gabriel [25] who also fit 4 pole Cole-Cole models [122]. A simpler model of the dielectric properties is the single pole Debye model, eq. (6.1), which has been shown to generate accurate fits in the microwave region [123].

$$\varepsilon_r(\omega) = \varepsilon_\infty + \frac{\varepsilon_s - \varepsilon_\infty}{1 + j\omega\tau} + \frac{\sigma_s}{j\omega\varepsilon_0} \tag{6.1}$$

Where ε_s is the static (low-frequency) permittivity, ε_∞ is the optical (high-frequency) permittivity, τ is the relaxation constant, and σ_s is the static conductivity.

The Debye model is used because if τ is held constant the complex permittivity becomes a linear function of the remaining Debye parameters. The relaxation constants vary little between the tissues [123]. The Debye model is fit to the Cole-Cole results from 300 MHz to 3.0 GHz with a relaxation constant of 50 ps. Note that in [7] a relaxation constant of 17.5 ps was used, however the higher τ used here will better account for the low frequency dispersion. A similar relaxation constant was used for a Debye model of skin tissue in the low GHz range in [124]. Fig. 6.1 shows the Cole-Cole models and their associated Debye model fits. Table 6.1 shows the tissue percent water content [24], Debye parameters, and the sum square error of the residual complex permittivities between the Debye fit and literature Cole-Cole models normalized to the number of frequency points.

In [7], a linear model between the Debye parameters for the various tissues and their water content is established. Using this linear model, the effect of changes in tissue water content on dielectric properties can be estimated. Because different Debye models were used to accommodate lower frequencies, the linear fit is done again. Fig. 6.2 shows the linear relationship between the Debye parameters and water contents for the forearm tissues. Table 6.2 shows the corresponding slopes and the R^2 values for the fits.

In [7], model is then developed for estimating the changes in the tissue water content

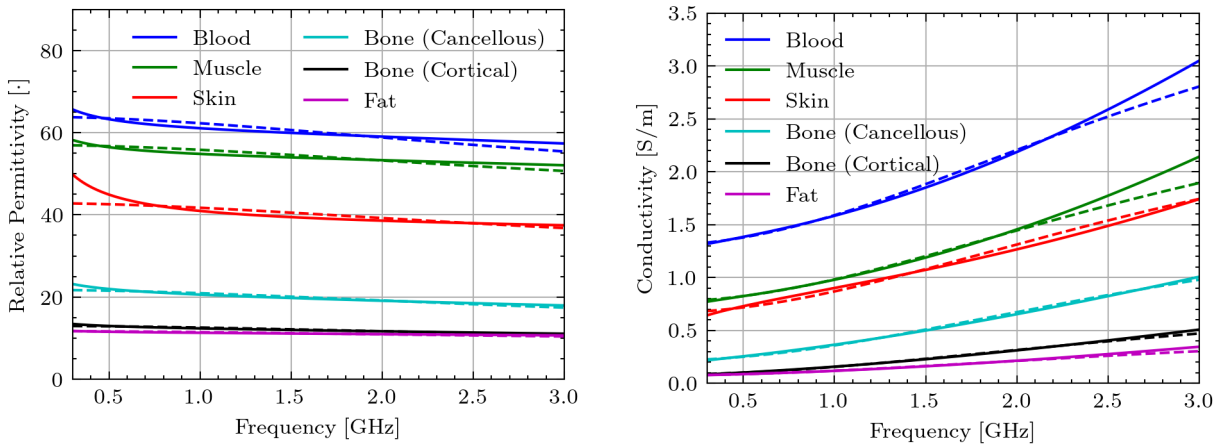

Figure 6.1: Forearm tissue properties. Literature values (solid) [122] and Debye fit (dashed).

Table 6.1: Water content of forearm tissue [24], Debye parameters of fit and mean sum squared error between Debye and Cole-Cole models.

Tissue	Water content [%]	ε_s [·]	ε_∞ [·]	σ_s [S/m]	τ [ps]	Error
Blood	80.0	63.9	45.8	1.30	50	1.03
Muscle	74.1	57.0	44.0	0.77	50	0.59
Skin	65.3	42.9	29.9	0.66	50	2.10
Bone (cancellous)	23.0	21.8	12.5	0.21	50	0.14
Bone (cortical)	15.0	13.0	8.3	0.08	50	0.03
Fat	21.2	11.7	9.0	0.07	50	0.02

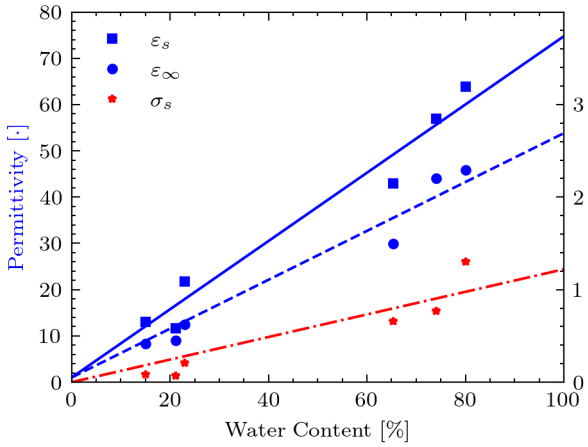

Figure 6.2: Debye parameters as a linear function of water content with linear regression.

Table 6.2: Slopes for linear fit of tissue Debye parameters vs water content and R^2 values.

Parameter	Slope	R^2
ε_s	0.73	0.96
ε_∞	0.53	0.96
σ_s	0.01	0.84

based on changes in total body water content and subsequent weight changes due to water loss, eq. (6.2). This method uses the subject's sex and age to estimate the fraction of total body water content. The method showed good agreement between theory, simulation [7] and the wrestler pilot study [8].

$$\boldsymbol{D}_i(\Delta W) = \boldsymbol{D}_{i,nominal} + \left(\frac{\phi_i}{\phi_B}\Delta W\right)\boldsymbol{m} \tag{6.2}$$

where i denotes the tissue type, ΔW is weight change, $\boldsymbol{D}$ is a vector with the tissue's Debye parameters, ϕ_i is the tissue water fraction (Table 6.1), ϕ_B is the body water fraction, and $\boldsymbol{m}$ is a vector with the Debye parameter slopes.

Applying this dehydration model to the Debye fits yields a Debye model that is then used to generate the permittivity and conductivity for the forearm model.

6.2 Change Detection

The change detection techniques as outlined in Section 5.2.2 will now be applied to models with realistic changes in tissue properties. The first technique applies blind inversions for both the baseline and perturbed measurements. The second technique uses the blind baseline inversion as an *a priori* initialization for the change detection. Clinically relevant changes in hydration are applied via weight losses of 0 - 2.0 %. Figs. 6.3 and 6.4 show the permittivity of the Duke and Ella models at baseline ($\Delta W = 0\%$) and at $\Delta W = 2\%$.

Unless specified, the data will be generated using the same 8 cm x 8 cm (80 x 80) grid as in the design section, but the inversion will now be done on a slightly different grid of

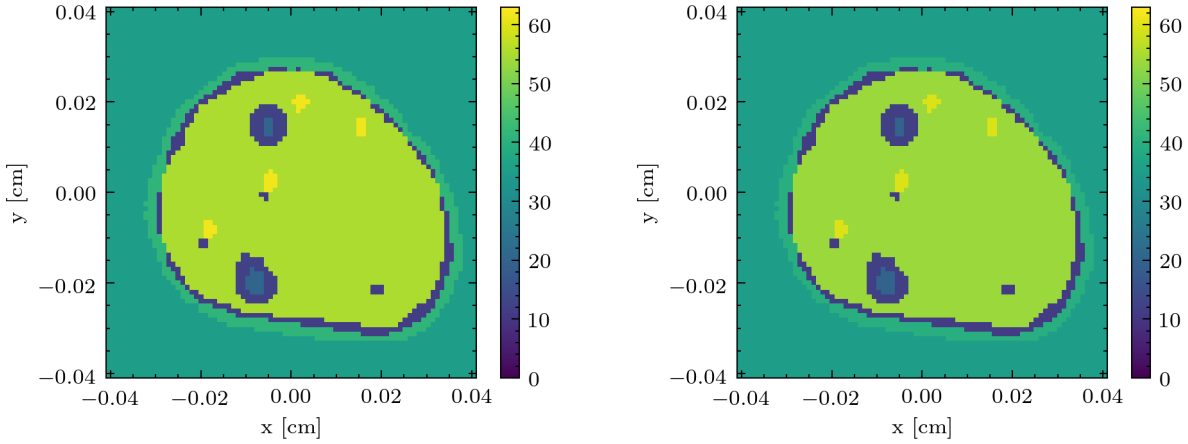

(a) $\Delta W = 0.0\%$ (b) $\Delta W = 2.0\%$

Figure 6.3: Permittivity of Duke forearm model at baseline and 2% dehydration.

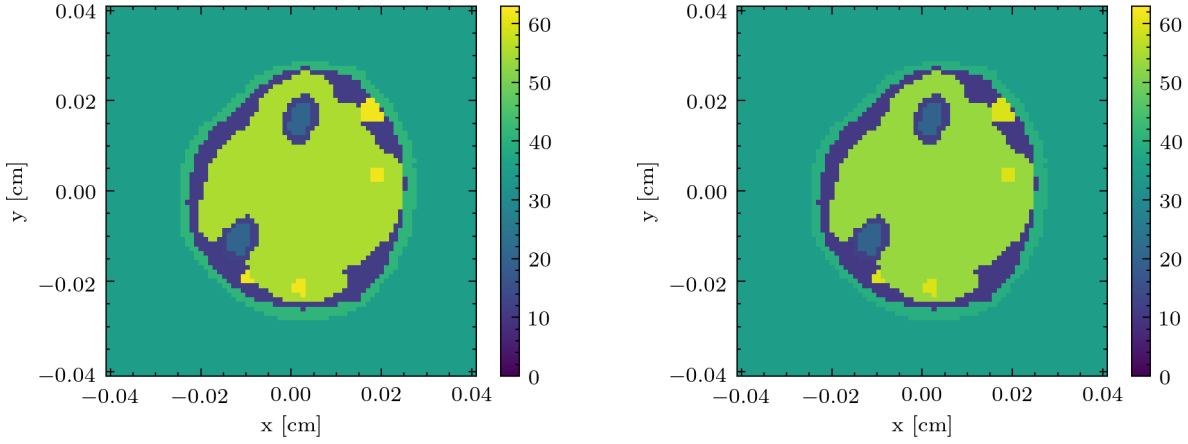

(a) $\Delta W = 0.0\%$ (b) $\Delta W = 2.0\%$

Figure 6.4: Permittivity of Ella forearm model at baseline and 2% dehydration.

8.2 cm x 8.2 cm (40 x 40) grid. The different image domain grid helps prevent the so-called inverse crime when the data and inversion are generated on the same grid using the same method. This is considered a crime in the inverse problem community because it can lead to errors in the forward and inverse problems cancelling each other and an overly optimistic reconstruction [80].

To quantify changes in hydration, an estimate of the permittivity will be generated at baseline, ε_e, and a second estimate will be generated at with the different levels of dehydration, ε_d. Both the average permittivity and the bulk permittivity will be reported. The

relative change will be calculated, in percent, as:

$$\Delta\varepsilon = \frac{\varepsilon_d - \varepsilon_e}{\varepsilon_e} \cdot 100 \tag{6.3}$$

The sensitivity of the technique to changes in hydration is defined as:

$$S = \frac{\Delta\varepsilon_r}{\Delta W} \tag{6.4}$$

First, the Duke and Ella models will be used to validate the THA technique with noiseless measurements. Then the Duke model will be used to examine the impact of measurement noise on the performance of THA. Finally, the impact of repositioning on baseline permittivity estimates and change detection will be examined.

6.2.1 Noiseless Measurements

Noiseless measurements are generated at each hydration level and the relative change in the permittivity metrics calculated. These values are then compared to the expected values based on the input model. For Ella the expected average permittivity change is smaller because of the smaller forearm and thus more background medium is included. However, the actual bulk permittivity change is greater because the total body water estimate for Ella is less therefore a 2% change in weight produces a larger change in hydration and properties.

Fig. 6.5 shows the change in permittivity metrics using blind inversions. The average permittivity metrics follows the expected trend very closely for both Ella and Duke. The bulk permittivity follows the expected value less closely due to the smoothing of the forearm and segmenting of the reconstructed image. While the bulk permittivity metric is less sensitive than expected it is still more sensitive than the average permittivity.

Fig. 6.6 shows the change in permittivity metrics using the *a priori* inversions. From the average permittivity, the Duke model follows the expected value closely, but the Ella model shows greater than expected sensitivity to changes in hydration. The bulk permittivity esti-

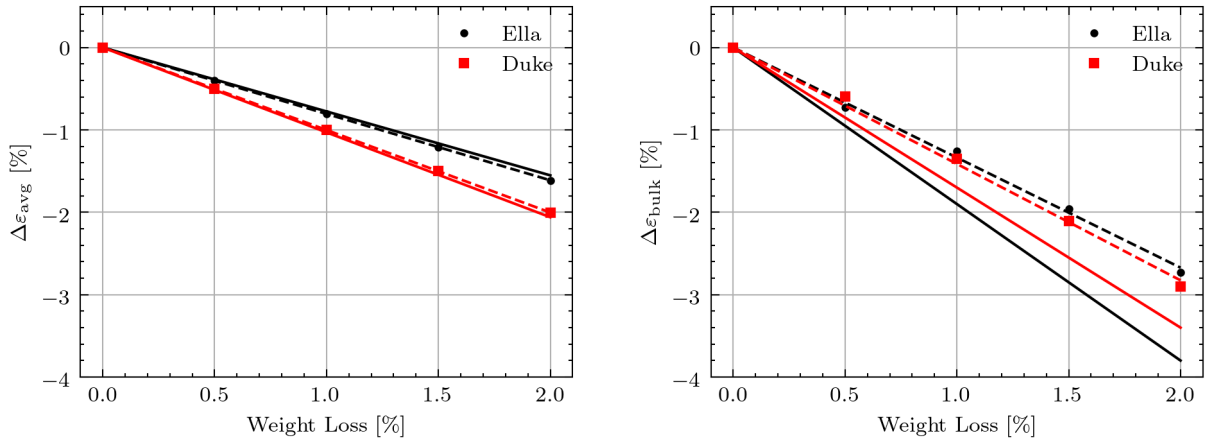

Figure 6.5: Estimated change in permittivity due to dehydration using blind inversions. Dashed lines represent linear regression and solid lines represent input model values.

mates for the *a priori* estimates are very similar to those of the blind inversions. The similar bulk permittivity sensitivity across both models and techniques suggests the sensitivity is limited by either the forearm smoothing or image segmentation.

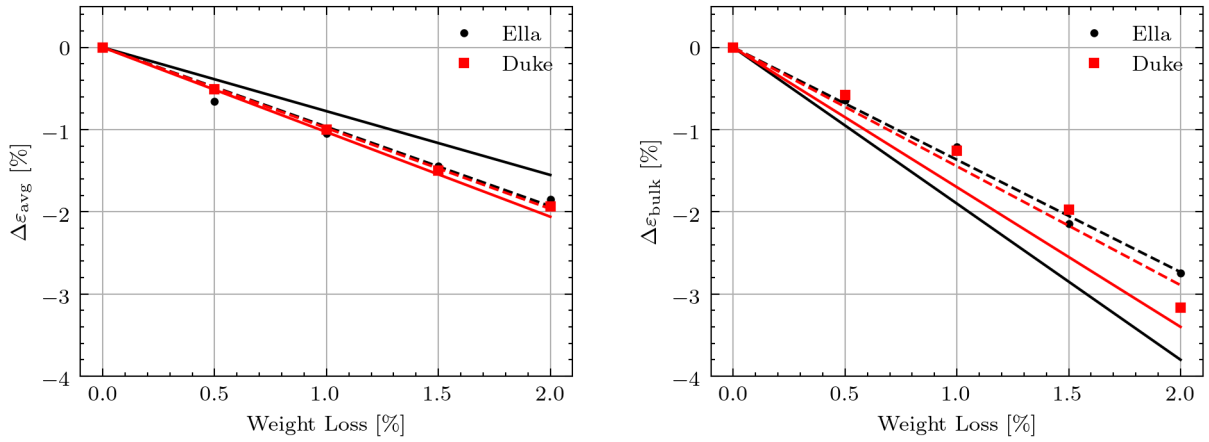

(a) (b)

Figure 6.6: Estimated change in permittivity due to dehydration using *a priori* inversions. Dashed lines represent linear regression and solid lines represent input model values.

Table 6.3 shows the slope of the linear regressions and the associated R^2 values. The very high R^2 indicate a strong linear relationship between each permittivity metric for both models as expected. The slopes show good agreement with the expected values. In [7], slopes of -1.8 and -2.3 for Duke and Ella, respectively, were found using TDS.

Table 6.3: Linear regression parameters for changes in permittivity due to dehydration for Duke and Ella models.

	$\Delta\varepsilon_{\text{avg}}$			$\Delta\varepsilon_{\text{bulk}}$		
Case	Actual Slope [·]	Slope [·]	R^2	Actual Slope [·]	Slope [·]	R^2
Duke, *a priori*	-1.03	-0.98	1.0	-1.71	-1.35	0.99
Duke, blind	-1.03	-1.00	1.0	-1.71	-1.41	1.0
Ella, *a priori*	-0.78	-0.96	1.0	-1.90	-1.37	1.0
Ella, blind	-0.78	-0.81	1.0	-1.90	-1.33	1.0

Table 6.4: Measured noise levels from the literature.

Reference	Noise Level [%]	Background Medium	Comment
[105]	10	Distilled Water	
[37]	3.0	Saline	
[11]	20	Saline	Noise defined using reciprocal data
[115]	10	Glycerin	Depends on frequency

6.2.2 Noise Analysis

The influence of measurement noise on the tomographic hydration assessment technique will now be examined. Noise levels of $1, 5, 10, 25\%$ will be added using eq. (5.20). At each noise and hydration level, ten measurements are taken. The baseline measurements are them inverted without an *a priori*. For the blind inversion technique, the ten perturbed measurements are inverted independently. For the *a priori* technique, each of the ten baseline inversions is used as an *a priori* for each of ten perturbed measurements (i.e. 100 inversions total). All combinations of the blind inversions are compared, generating 100 difference measurements.

Table 6.4 shows measured noise levels from a number of tomographic systems in the literature.

Fig. 6.7 shows the estimated permittivities at various noise levels using blind inversions. Fig. 6.8 shows the estimated permittivities at various noise levels using *a priori* inversions. For both techniques there is good agreement between the results with noise and the noiseless results. The bulk permittivity estimate is more sensitive to noise and its sensitivity to changes in hydration decreases with noise. This happens because as the measurements get

noisier, there is more variation in the reconstructed image which makes it harder to segment the image correctly. The *a priori* inversions are more sensitive to noise level than the blind inversions. This occurs because the baseline reconstructions were done with different errors than the difference measurements.

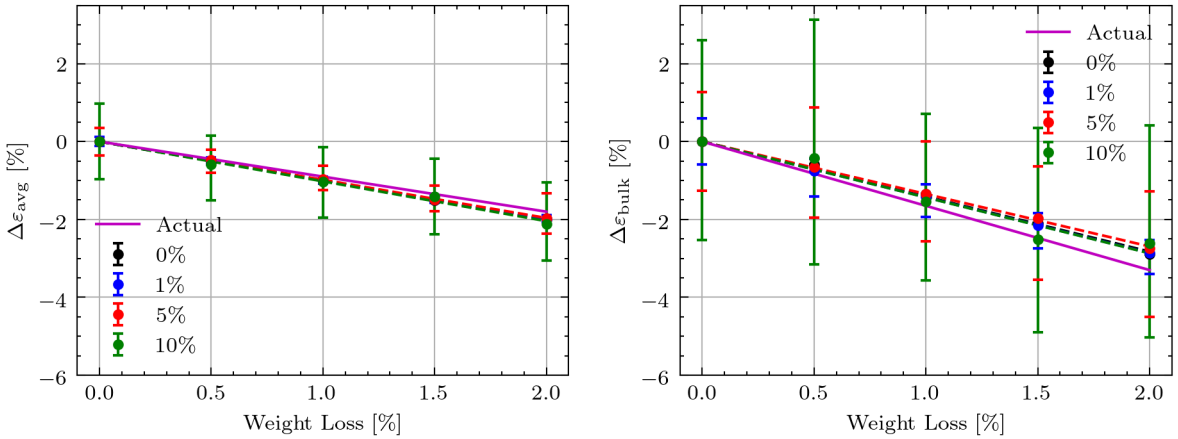

(a) (b)

Figure 6.7: Estimated change in permittivity for Duke model undergoing 2% weight loss using blind inversions at various noise levels. Dots represent sample median, error bars represent minimum and maximum, and dotted lines are linear regressions.

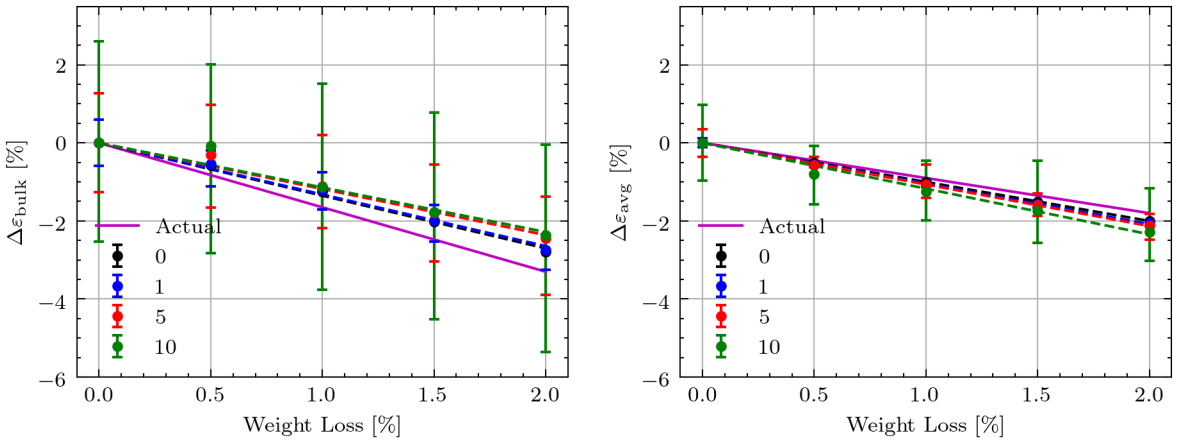

(a) (b)

Figure 6.8: Estimated change in permittivity for Duke model undergoing 2% weight loss using *a priori* inversions at various noise levels. Dots represent sample median, error bars represent minimum and maximum, and dotted lines are linear regressions.

Figs. 6.9 and 6.10 show the measured samples at $\Delta W = 2\%$. From these plots the

exact distribution of the samples can be seen. The variance in the measured permittivity is directly affected by the noise level.

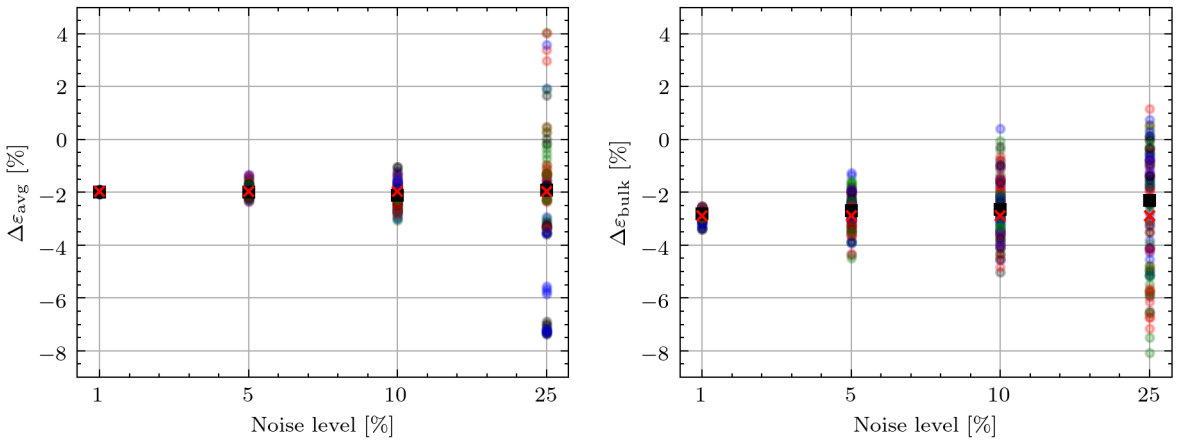

(a) (b)

Figure 6.9: Measured changes in permittivity at $\Delta W = 2\%$ at various noise levels using blind inversions. Dots represent samples, 'x' represents noiseless result, and squares represent sample median.

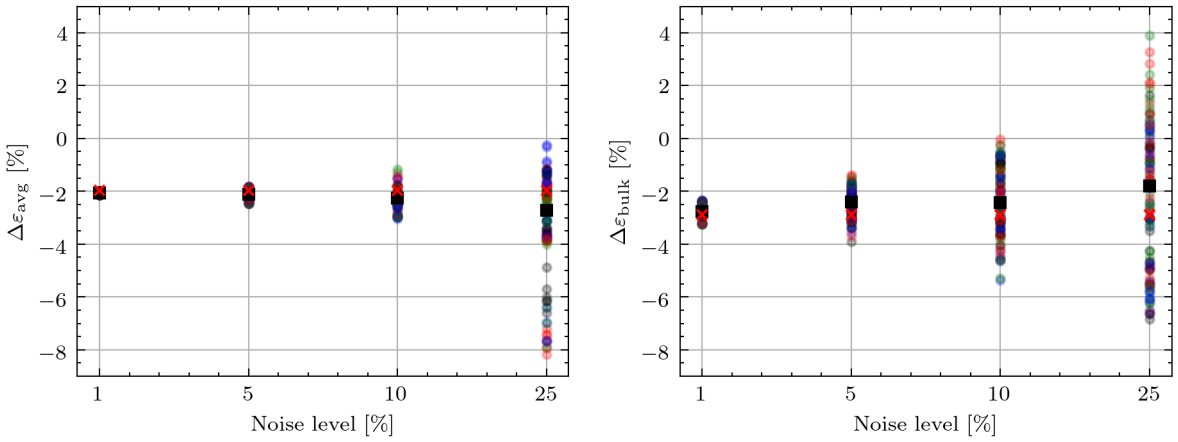

(a) (b)

Figure 6.10: Measured changes in permittivity at $\Delta W = 2\%$ at various noise levels using *a priori* inversions. Dots represent samples, 'x' represents noiseless result, and squares represent sample median.

Table 6.5 shows the slopes of the linear regression at each noise level. The R^2 for all regressions were greater than 0.98.

Because the expected changes in permittivity are so small, the noise level presents a

Table 6.5: Linear regression slopes for change in permittivity due to weight loss.

		Noise Level [%]			
Case	Actual	0	1	5	10
$\varepsilon_{\text{bulk}}$, blind	-1.71	-1.41	-1.43	-1.34	-1.43
$\varepsilon_{\text{bulk}}$, *a priori*	-1.71	-1.35	-1.32	-1.18	-1.17
ε_{avg}, blind	-1.03	-1.00	-0.99	-0.98	-1.02
ε_{avg}, *a priori*	-1.03	-0.98	-1.32	-1.18	-1.14

serious design challenge to the tomographic hydration assessment technique. While the sample medians agree well with the expected changes, the noise in the measurements and variance in permittivity estimates could preclude the useful application of THA.

Ultimately, the noise level will be determined by the physical system. In this context, the noise represents any measurement errors including the mismatch between the propagation model and the physical wave propagation. As such, it is important to accurately calibrate the measured signals, avoid mutual coupling between sensors, and reduce reflections from the system boundary by increasing matching fluid loss. These considerations are outside the scope of this work, but noise should be a primary consideration when designing a physical THA system.

6.2.3 Position Analysis

Next the effect of variations in the forearm positioning will be examined.

The image domain is increased to its maximum size of 10 cm x 10 cm. Inversions are done in a domain of size 10.2 cm x 10.2 cm to avoid the inverse crime. The center of the forearm (x_0, y_0) is varied by generating x and y steps Δx, Δy using a uniform distribution from -1 cm to 1 cm in x and y.

Noiseless measurements are generated at ten forearm locations. Changes in hydration of corresponding to $\Delta W = 0, 0.5, ..., 2.0\%$ are applied at each location. The blind inversions and *a priori* inversions are applied. The blind inversions are done independently and 100 *a*

priori inversions are done. Fig. 6.11 shows the Duke forearm model displaced by (1 cm, 1 cm) in the tomography setup.

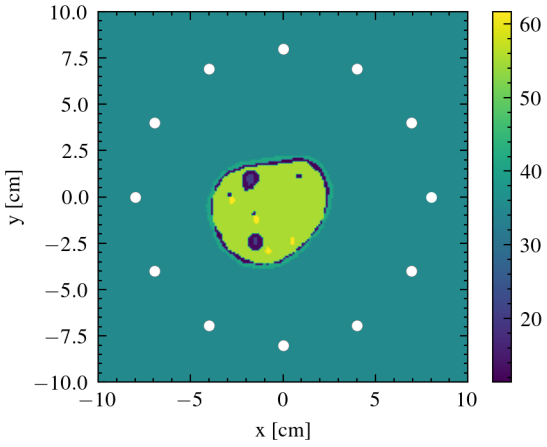

Figure 6.11: Duke forearm model displaced by 10 mm in x and y.

First the effect of placing the forearm off center is examined by doing inversions across the ΔW range with the forearm located at the same spot in the baseline and difference measurements. Fig. 6.12 shows the RRE at each hydration level as a function of distance from the center. When the forearm is placed away from the center, it sometimes fails to converge to the 1 % threshold. The same measurements fail to converge with both blind and *a priori* inversions however the *a priori* converge to a lower RRE. Decreasing the empirical regularization parameter p from 2 can improve the convergence but still not all the results converge. Interestingly, some results at displacements of 0.75 cm converge and others do not. This suggests the convergence is sensitive to exact placement of the forearm. This could be due to the asymmetry of the forearm such as the location of the bones within the forearm.

As can be seen in Figs. 6.13 and 6.14 this failure to converge has an impact on the absolute permittivity estimations. The non-convergent results consistently have a different baseline permittivity estimate than the convergent results. However, the technique maintains its sensitivity to hydration changes since the change in permittivity is similar for all positions.

Next the effect of positioning errors between the baseline and difference measurements is examined. The relative change in permittivity at $\Delta W = 2\%$ will be examined to see

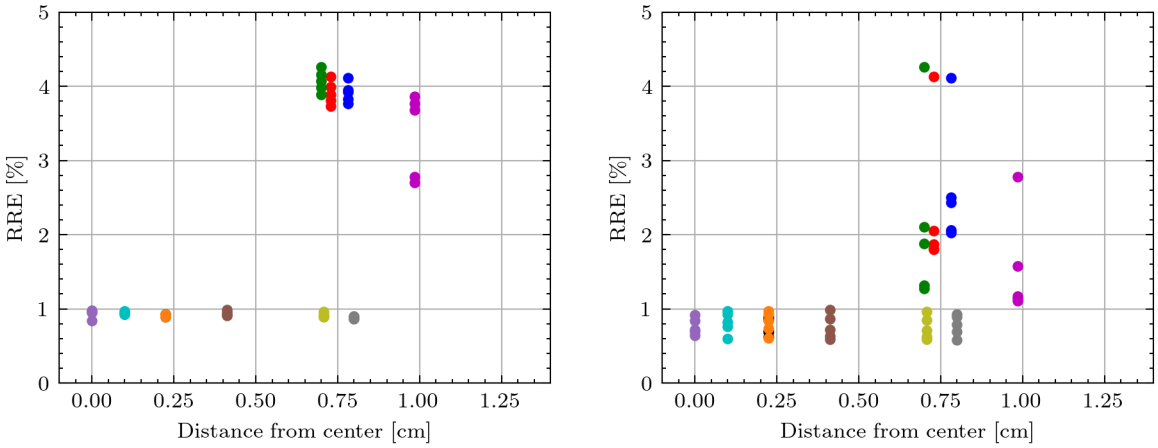

(a) Blind inversions

(b) *A priori inversions.*

Figure 6.12: Relative residual error at $\Delta W = 0, 0.5, 1.0, 1.5, 2.0$ with forearm at various locations.

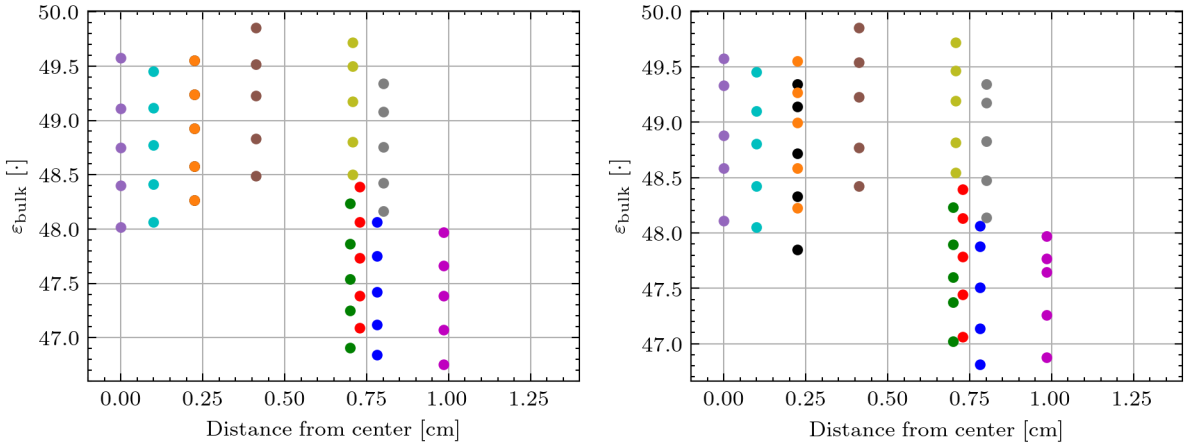

(a) Blind inversions

(b) *A priori* inversions.

Figure 6.13: Absolute bulk permittivity estimates at $\Delta W = 0, 0.5, 1.0, 1.5, 2.0\%$ with forearm at various locations.

impact of positioning on clinically relevant changes. As can be seen in Figs. 6.15 and 6.16 the average permittivity is more robust to positioning errors and the different levels of RRE. While the estimate of bulk permittivity change performs much worse, the worst performing samples are those that did not converge fully. The *a priori* estimates are more robust due to the better convergence at $\Delta W = 2\%$.

These results suggest that the tomographic approach is robust to small repositioning errors between measurements provided the inversion converges to the expected residual thresh-

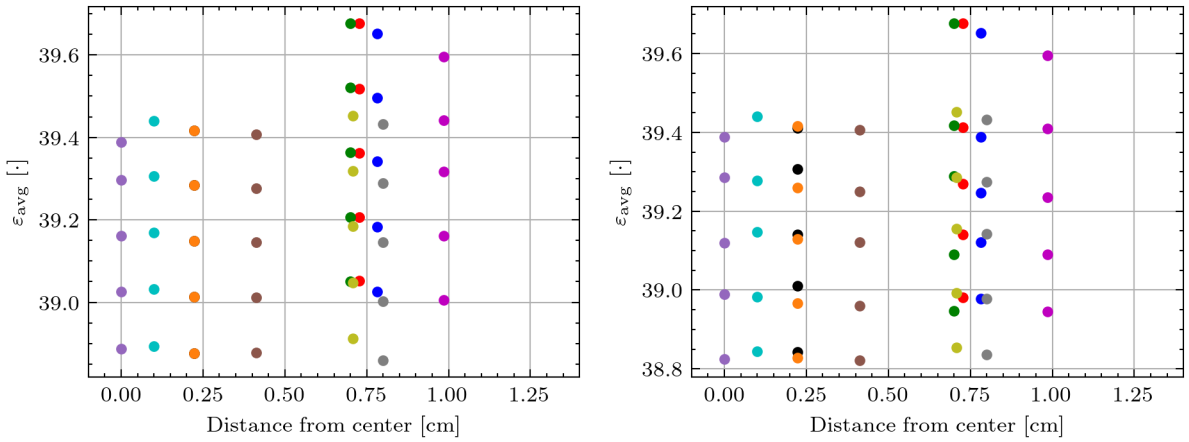

(a) Blind inversions

(b) *A priori* inversions.

Figure 6.14: Absolute average permittivity estimates at $\Delta W = 0, 0.5, 1.0, 1.5, 2.0\%$ with forearm at various locations.

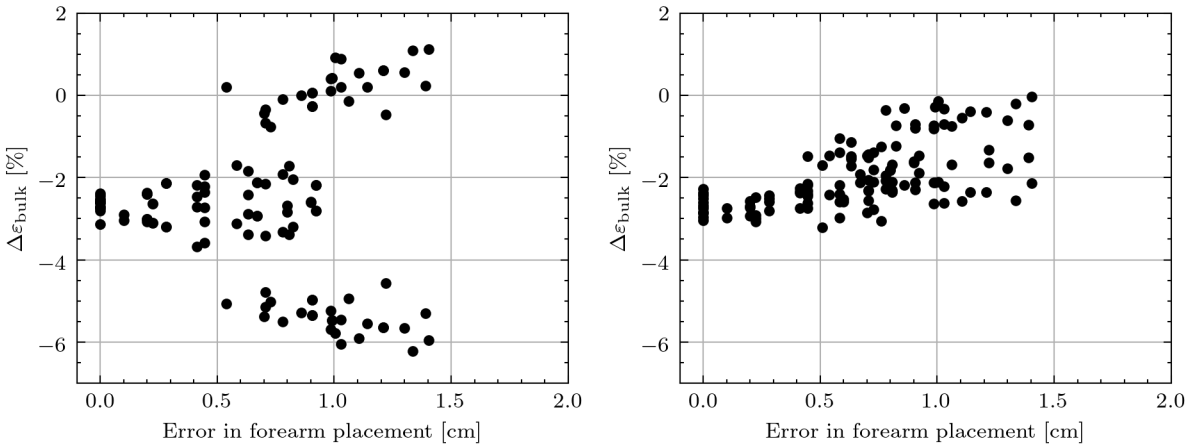

(a) Blind inversions

(b) *A priori* inversions.

Figure 6.15: Estimated change in bulk permittivity at $\Delta W = 2.0\%$ with errors in baseline and difference forearm locations.

old. Every attempt should be made to reduce repositioning errors in practice by including position guidance for the subject such as a handle and developing a standard procedure for placing the forearm inside the system. By comparing the phase of the various signals around the system, it could be possible to estimate positioning errors and retake the measurement if the errors are expected to be too large. In [11], the difference in reciprocal transmission data (i.e. S_{21} and S_{12}) is used to estimate the movements during a single scan. The effect of larger repositioning errors should also be examined. However, if the repositioning errors

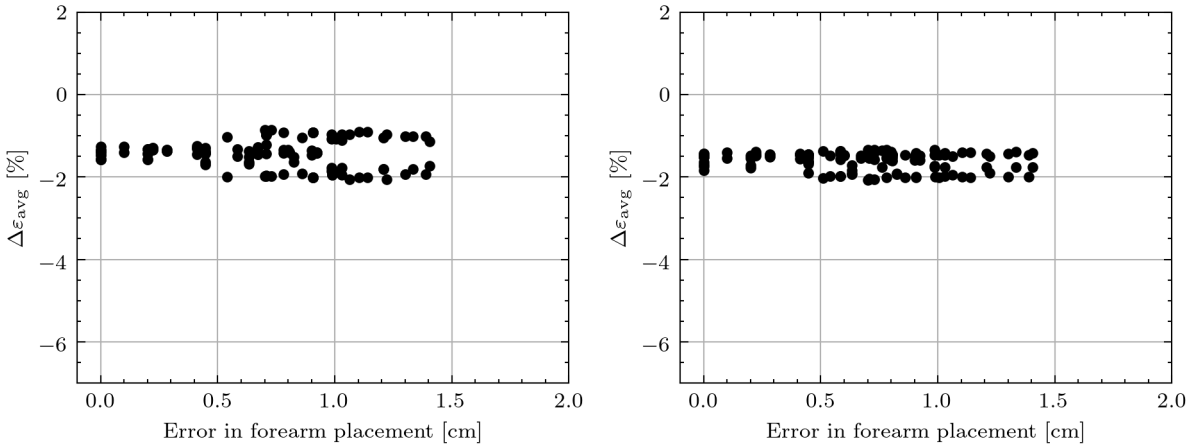

(a) Blind inversions

(b) *A priori* inversions.

Figure 6.16: Estimated change in average permittivity at $\Delta W = 2.0\%$ with errors in baseline and difference forearm locations.

get much larger, the forearm will not be in the imaging domain so the reconstruction will be quite poor.

6.3 Conclusion

In this chapter the tomographic hydration assessment technique was validated in two *in silico* models, against various noise levels, and positioning errors. THA accurately measured changed in permittivity representative of clinically relevant changes in hydration in both the Duke and Ella models. The bulk permittivity metric was less sensitive to changes in permittivity than expected due to image smoothing and segmentation, but it was more sensitive than the average permittivity metric. However, the bulk permittivity metric was more sensitive to the effect of noise. The THA technique is very sensitive to noise and the noise level should be primary consideration when designing a THA system. The THA technique was less sensitive to positioning errors, however there were some convergence issues when the forearm was placed away from the center. The *a priori* inversion was more sensitive to noise, but less sensitive to positioning errors due to better convergence. This technique shows potential for detecting clinically relevant changes in hydration, however it will need

to be validated using real data.

Chapter 7

Conclusion

A pilot study of fasting volunteers failed to show a relationship between permittivity estimates from TDS and the assumed dehydration occurring throughout the day. While dehydration was occurring as measured by the subjects' weight change, this subtle dehydration presents a serious challenge to the measurement capabilities of hydration assessment technology. Urine specific gravity, another commonly used measurement of hydration status, failed to detect any changes in hydration. This study motivated further research into microwave hydration assessment specifically MWT.

Using a standard MWT approach including DBIM and standard Tikhonov regularization, a tomographic hydration assessment technique was developed. To augment this standard approach an empirical method for determining the regularization parameter was introduced. This empirical method greatly increases the convergence of blind inversions for high contrast objects. A standard tomographic system was then designed sequentially to find practical and effective design parameters for hydration assessment.

The THA system and technique was then validated using realistic forearm models. The effect of measurement noise and placement errors are examined. Change detection was analyzed using both blind inversions and an *a priori* inversions. Both techniques produced similar results however *a priori* was more sensitive to noise level but less sensitive to conver-

gence errors due to placement. The measurement noise has a clear impact on the quality of the change detection so should be a primary design consideration. It is important to reiterate that measurement noise in this context entails any errors in the measurement including deviations between model propagation, antenna mutual coupling, and thermal noise. Thus, it will largely be defined by the system itself.

In the context of the objectives outlined in Chapter 1 the following was achieved:

1. **Evaluate the efficacy of microwave hydration assessment techniques in a sedentary population.** From the study of fasting volunteers, a need for more sensitive and robust microwave hydration assessment techniques is identified.

2. **Develop a robust method of regularization without the need for *a priori* information.** By combining the well-known L-Curve technique with an empirical adaptive approach, a robust selection of the regularization parameter is made greatly improving non-linear reconstruction of high contrast objects.

3. **Design a tomographic system for microwave hydration assessment in simulation.** The systematic design yields a system that can accurately estimate the dielectric properties of the forearm while enabling a practical implementation.

4. **Validate microwave tomography for hydration assessment *in silico*.** The THA technique is shown to accurately detect changes in hydration as little as 2% by body weights.

7.1 Contributions

This work makes the following contributions to the existing literature:

1. **A pilot study of microwave hydration assessment technology in sedentary populations.** While previous work reported tracking dramatic, short-term changes in

hydration [8], the study of fasting volunteers is the first report of microwave hydration assessment in this population. This provides insight into the challenges of microwave hydration assessment.

2. **A simple empirical method for determining the Tikhonov regularization parameter.** This empirical method combines two previously reported method of determining the regularization parameter the L-curve [84, 43] and empirical adaptive methods [105]. To the author's knowledge, this is the first reported application of the regularization parameter conditions outlined in [111] to MWT.

3. **A design of a tomographic system for hydration assessment.** The systematic design used here is widely applicable to tomographic systems. The resulting system is readily implemented. Similar to previous work [69, 115] a broad array of matching media provide adequate results. Selecting a matching medium often consists of a trade-off between measurement loss and model errors which can be used to optimize physical tomographic systems.

4. **Proof of concept for tomographic microwave hydration assessment.** This work demonstrates the ability to track changes in properties related to clinically relevant changes in hydration over time. Utilizing baseline reconstructions as an *a priori* estimate to detect changes is proposed instead of incorporating information from *ad hoc* [11] methods and other imaging modalities [104]. Initial *in silico* validation of bulk property estimation using MWT is potentionally more robust to changes in tissue composition, such as larger adipose tissue layers, than imaging applications [11].

7.2 Limitations and Future Work

There are a number of limitations in the present work that warrant further investigation. This future work can be viewed in three parts: *in vivo* validation, improvements to the MWT

algorithms, and practical implementation.

First and foremost, the technique should be validated with real measurements. As an initial step the proposed regularization scheme should be validated using available forearm data, e.g. [11, 38], to ensure that a reasonable reconstruction is possible. The technique should then be validated using real measurements of phantom materials with known properties. While the effect of noise and positioning were examined *in silico*, the robustness of the change detection algorithm to the measurement and model errors inherent to real measurements should be verified. Ultimately, the tomographic technique should be verified in volunteers undergoing changes in hydration. While fasting volunteers provide an excellent model for the subtle changes in dehydration sedentary healthy adults experience day-to-day, the initial validation should be explored using more acute changes in hydration such as exercising athletes.

There are a number of improvements that could potentially increase the sensitivity and robustness to noise of the technique. First, there are the myriad variations on the DBIM with standard Tikhonov regularization approach taken here. More advanced regularization such as using a Laplacian regularization matrix [11] or multiplicative regularization [41] could help improve the image quality providing more accurate permittivity estimates. Secondly, alternative formulations such as frequency hopping [125] or CSI [11] could also help image quality and algorithm convergence. Applying the differential inversion technique [97] could improve system robustness to systematic measurement errors.

Finally, more consideration of the practical design and target population of THA is needed. If the target population is athletes, a more convenient implementation that can compete with simple hydration metrics like weight change and urine concentration should be considered. In-contact systems are of interest for possible wearable and long-term monitoring applications of microwave tomography, e.g. [126]. While in-contact tomographic systems have had little traction for important technical reasons, the low-resolution requirements of hydration assessment could make it a promising application to explore. If more clinical

applications such as monitoring changes in hydration in older persons are to be pursued, a bulkier implementation could be adequate, as it would be important to maintain sensitivity to ensure clinically relevant dehydration is detected before any health concerns are present.

Bibliography

[1] M. S. Ganio, L. E. Armstrong, D. J. Casa, B. P. McDermott, E. C. Lee, L. M. Yamamoto, S. Marzano, R. M. Lopez, L. Jimenez, L. L. Bellego, E. Chevillotte, and H. R. Lieberman, "Mild dehydration impairs cognitive performance and mood of men," *British Journal of Nutrition*, vol. 106, no. 10, pp. 1535–1543, Nov. 2011.

[2] S. N. Cheuvront and R. W. Kenefick, "Dehydration: Physiology, Assessment, and Performance Effects," *Comprehensive Physiology*, pp. 257–285, 2014.

[3] B. M. Popkin, K. E. D'Anci, and I. H. Rosenberg, "Water, hydration, and health," *Nutrition Reviews*, vol. 68, no. 8, pp. 439–458, Aug. 2010.

[4] D. C. Garrett, N. Rae, J. R. Fletcher, S. Zarnke, S. Thorson, D. B. Hogan, and E. C. Fear, "Engineering Approaches to Assessing Hydration Status," *IEEE Reviews in Biomedical Engineering*, vol. 11, pp. 233–248, 2018.

[5] L. Hooper, D. Bunn, F. O. Jimoh, and S. J. Fairweather-Tait, "Water-loss dehydration and aging," *Mechanisms of Ageing and Development*, vol. 136-137, pp. 50–58, Mar. 2014.

[6] A. M. El-Sharkawy, A. Virdee, A. Wahab, D. J. Humes, O. Sahota, M. A. J. Devonald, and D. N. Lobo, "Dehydration and clinical outcome in hospitalised older adults: A cohort study," *European Geriatric Medicine*, vol. 8, no. 1, pp. 22–29, Feb. 2017.

[7] D. C. Garrett and E. C. Fear, "Feasibility Study of Hydration Monitoring Using Microwaves–Part 1: A Model of Microwave Property Changes With Dehydration," *IEEE Journal of Electromagnetics, RF and Microwaves in Medicine and Biology*, vol. 3, no. 4, pp. 292–299, Dec. 2019.

[8] D. C. Garrett, J. R. Fletcher, D. B. Hogan, T. S. Fung, and E. C. Fear, "Feasibility Study of Hydration Monitoring Using Microwaves–Part 2: Measurements of Athletes," *IEEE Journal of Electromagnetics, RF and Microwaves in Medicine and Biology*, vol. 3, no. 4, pp. 300–307, Dec. 2019.

[9] K. R. Foster and H. P. Schwann, "Dielectric Properties of Tissues and Biological Materials: A Critical Review," *Critical Reviews in Biomedical Engineering*, vol. 17, no. 1, pp. 25–104, 1989.

[10] P. M. Meaney, M. W. Fanning, T. Raynolds, C. J. Fox, Q. Fang, C. A. Kogel, S. P. Poplack, and K. D. Paulsen, "Initial Clinical Experience with Microwave Breast Imaging in Women with Normal Mammography," *Academic Radiology*, vol. 14, no. 2, pp. 207–218, Feb. 2007.

[11] C. Gilmore, A. Zakaria, S. Pistorius, and J. LoVetri, "Microwave Imaging of Human Forearms: Pilot Study and Image Enhancement," *International Journal of Biomedical Imaging*, vol. 2013, pp. 673 027– 1–673 027–17, Aug. 2013.

[12] E. Jéquier and F. Constant, "Water as an essential nutrient: The physiological basis of hydration," *European Journal of Clinical Nutrition*, vol. 64, no. 2, pp. 115–123, Feb. 2010.

[13] S. M. Kleiner, "Water: An Essential But Overlooked Nutrient," *Journal of the American Dietetic Association*, vol. 99, no. 2, pp. 200–206, Feb. 1999.

[14] "National hospital discharge survey," https://www.cdc.gov/nchs/nhds/nhds_tables.htm#number, Jul. 2021.

[15] L. E. Armstrong, "Assessing Hydration Status: The Elusive Gold Standard," *Journal of the American College of Nutrition*, vol. 26, no. sup5, pp. 575S–584S, Oct. 2007.

[16] A. C. Grandjean and S. M. Campbell, *Hydration: Fluids for Life*. ILSI North America, 2004.

[17] S. A. Kavouras, "Assessing hydration status," *Current Opinion in Clinical Nutrition & Metabolic Care*, vol. 5, no. 5, pp. 519–524, Sep. 2002.

[18] S. N. Cheuvront, B. R. Ely, R. W. Kenefick, and M. N. Sawka, "Biological variation and diagnostic accuracy of dehydration assessment markers," *The American Journal of Clinical Nutrition*, vol. 92, no. 3, pp. 565–573, Sep. 2010.

[19] L. Armstrong, C. M. Maresh, J. W. Castellani, M. F. Bergeron, R. W. Kenefick, K. E. LaGasse, and D. Riebe, "Urinary Indices of Hydration Status," *International Journal of Sport Nutrition and Exercise Metabolism*, vol. 4, no. 3, pp. 265–279, 1994.

[20] D. J. Casa, P. M. Clarkson, and W. O. Roberts, "American College of Sports Medicine roundtable on hydration and physical activity: Consensus statements," *Current Sports Medicine Reports*, vol. 4, no. 3, pp. 115–127, May 2005.

[21] S. M. Shirreffs and R. J. Maughan, "Urine osmolality and conductivity as indices of hydration status in athletes in the heat," *Medicine and science in sports and exercise*, vol. 30, no. 11, pp. 1598–1602, Nov. 1998.

[22] R. P. Francesconi, R. W. Hubbard, P. C. Szlyk, D. Schnakenberg, D. Carlson, N. Leva, I. Sils, L. Hubbard, V. Pease, J. Young, and a. et, "Urinary and hematologic indexes of hypohydration," *Journal of Applied Physiology*, vol. 62, no. 3, pp. 1271–1276, Mar. 1987.

[23] S. Gabriel, R. W. Lau, and C. Gabriel, "The dielectric properties of biological tissues: III. Parametric models for the dielectric spectrum of tissues," *Physics in Medicine and Biology*, vol. 41, no. 11, pp. 2271–2293, Nov. 1996.

[24] F. A. Duck, *Physical Properties of Tissues: Comprehensive Reference Book*, 1st ed. New York, NY, USA: Academic, 2013.

[25] S. Gabriel, R. W. Lau, and C. Gabriel, "The dielectric properties of biological tissues: II. Measurements in the frequency range 10 Hz to 20 GHz," *Physics in Medicine and Biology*, vol. 41, no. 11, pp. 2251–2269, Nov. 1996.

[26] M. P. Robinson, J. Clegg, and D. A. Stone, "A novel method of studying total body water content using a resonant cavity: Experiments and numerical simulation," *Physics in Medicine and Biology*, vol. 48, no. 1, pp. 113–125, Jan. 2003.

[27] B. Oldroyd, M. Robinson, E. Lindley, L. Rhodes, and K. Hind, "Resonant cavity perturbation: A promising new method for the assessment of total body water in children," *Physiological Measurement*, vol. 36, no. 12, pp. 2503–2517, Nov. 2015.

[28] D. S. Moran, Y. Heled, M. Margaliot, Y. Shani, A. Laor, S. Margaliot, E. E. Bickels, and Y. Shapiro, "Hydration status measurement by radio frequency absorptiometry in young athletes—a new method and preliminary results," *Physiological Measurement*, vol. 25, no. 1, pp. 51–59, Dec. 2003.

[29] R. Brendtke, M. Wiehl, F. Groeber, T. Schwarz, H. Walles, and J. Hansmann, "Feasibility Study on a Microwave-Based Sensor for Measuring Hydration Level Using Human Skin Models," *PLOS One*, vol. 11, no. 4, p. e0153145, Apr. 2016.

[30] R. Persico, *Introduction to Ground Penetrating Radar: Inverse Scattering and Data Processing*. Hoboken, New Jersey: Wiley, IEEE Press, 2014.

[31] J. D. Shea, P. Kosmas, S. C. Hagness, and B. D. V. Veen, "Three-dimensional microwave imaging of realistic numerical breast phantoms via a multiple-frequency inverse scattering technique," *Medical Physics*, vol. 37, no. 8, pp. 4210–4226, 2010.

[32] J.-C. Bolomey and C. Pichot, "Microwave tomography: From theory to practical imaging systems," *International Journal of Imaging Systems and Technology*, vol. 2, no. 2, pp. 144–156, 1990.

[33] R. Chandra, H. Zhou, I. Balasingham, and R. M. Narayanan, "On the Opportunities and Challenges in Microwave Medical Sensing and Imaging," *IEEE Transactions on Biomedical Engineering*, vol. 62, no. 7, pp. 1667–1682, Jul. 2015.

[34] D. Ireland, K. Bialkowski, and A. Abbosh, "Microwave imaging for brain stroke detection using Born iterative method," *IET Microwaves, Antennas & Propagation*, vol. 7, no. 11, pp. 909–915, 2013.

[35] P. M. Meaney, D. Goodwin, A. H. Golnabi, T. Zhou, M. Pallone, S. D. Geimer, G. Burke, and K. D. Paulsen, "Clinical Microwave Tomographic Imaging of the Calcaneus: A First-in-Human Case Study of Two Subjects," *IEEE Transactions on Biomedical Engineering*, vol. 59, no. 12, pp. 3304–3313, Dec. 2012.

[36] S. Y. Semenov, V. G. Posukh, A. E. Bulyshev, T. C. Williams, Y. E. Sizov, P. N. Repin, A. Souvorov, and A. Nazarov, "Microwave Tomographic Imaging of the Heart in Intact Swine," *Journal of Electromagnetic Waves and Applications*, vol. 20, no. 7, pp. 873–890, Jan. 2006.

[37] S. Semenov, J. Kellam, P. Althausen, T. Williams, A. Abubakar, A. Bulyshev, and Y. Sizov, "Microwave tomography for functional imaging of extremity soft tissues: Feasibility assessment," *Physics in Medicine and Biology*, vol. 52, no. 18, pp. 5705–5719, Sep. 2007.

[38] A. Broquetas, J. Romeu, J. Rius, A. Elias-Fuste, A. Cardama, and L. Jofre, "Cylindrical geometry: A further step in active microwave tomography," *IEEE Transactions on Microwave Theory and Techniques*, vol. 39, no. 5, pp. 836–844, May 1991.

[39] W. C. Chew, G. P. Otto, W. H. Weedon, J. H. Lin, C. C. Lu, Y. M. Wang, and M. Moghaddam, "Nonlinear diffraction tomography: The use of inverse scattering for imaging," *International Journal of Imaging Systems and Technology*, vol. 7, no. 1, pp. 16–24, 1996.

[40] A. Abubakar, P. M. van den Berg, and S. Y. Semenov, "Two- and Three-Dimensional Algorithms for Microwave Imaging and Inverse Scattering," *Journal of Electromagnetic Waves and Applications*, vol. 17, no. 2, pp. 209–231, Jan. 2003.

[41] P. Mojabi and J. LoVetri, "Microwave Biomedical Imaging Using the Multiplicative Regularized Gauss–Newton Inversion," *IEEE Antennas and Wireless Propagation Letters*, vol. 8, pp. 645–648, 2009.

[42] N. Joachimowicz, C. Pichot, and J.-P. Hugonin, "Inverse scattering: An interative numerical method for electromagnetic imaging," *IEEE Transactions on Antennas and Propagation*, vol. 39, no. 12, pp. 1742–1752, 1991.

[43] C. Gilmore, P. Mojabi, and J. LoVetri, "Comparison of an Enhanced Distorted Born Iterative Method and the Multiplicative-Regularized Contrast Source Inversion method," *IEEE Transactions on Antennas and Propagation*, vol. 57, no. 8, pp. 2341–2351, Aug. 2009.

[44] S. Semenov, A. Bulyshev, A. Abubakar, V. Posukh, Y. Sizov, A. Souvorov, P. van den Berg, and T. Williams, "Microwave-tomographic imaging of the high dielectric-contrast objects using different image-reconstruction approaches," *IEEE Transactions on Microwave Theory and Techniques*, vol. 53, no. 7, pp. 2284–2294, Jul. 2005.

[45] A. H. Sakr, "Fasting in Islam," *Journal of the American Dietetic Association*, vol. 67, no. 1, pp. 17–21, Jul. 1975.

[46] J. B. Leiper, A. M. Molla, and A. M. Molla, "Effects on health of fluid restriction during fasting in Ramadan," *European Journal of Clinical Nutrition*, vol. 57, no. S2, pp. S30–S38, Dec. 2003.

[47] R. J. Maughan and S. M. Shirreffs, "Hydration and performance during Ramadan," *Journal of Sports Sciences*, vol. 30, no. sup1, pp. S33–S41, Jul. 2012.

[48] K. Trabelsi, S. R. Stannard, H. Chtourou, W. Moalla, H. Ghozzi, K. Jamoussi, and A. Hakim, "Monitoring athletes' hydration status and sleep patterns during Ramadan observance: Methodological and practical considerations," *Biological Rhythm Research*, vol. 49, no. 3, pp. 337–365, May 2018.

[49] S. M. Shirreffs and R. J. Maughan, "Water and salt balance in young male football players in training during the holy month of Ramadan," *Journal of Sports Sciences*, vol. 26, no. sup3, pp. S47–S54, Dec. 2008.

[50] J. Ramadan, G. Telahoun, N. S. Al-Zaid, and M. Barac-Nieto, "Responses to exercise, fluid, and energy balances during ramadan in sedentary and active males," *Nutrition*, vol. 15, no. 10, pp. 735–739, Oct. 1999.

[51] R. J. Shephard and E. Bouhel, "Hydration and Fluid Restriction in Athletes," in *Optimizing Physical Performance During Fasting and Dietary Restriction: Implications for Athletes and Sports Medicine*. CRC Press, Aug. 2015, pp. 117–130.

[52] A. Chaouachi, J. B. Leiper, N. Souissi, A. J. Coutts, and K. Chamari, "Effects of Ramadan Intermittent Fasting on Sports Performance and Training: A Review," *International Journal of Sports Physiology & Performance*, vol. 4, no. 4, pp. 419–434, Dec. 2009.

[53] S. Hassan, F. Hassan, N. Abbas, K. Hassan, N. Khatib, R. Edgim, R. Fadol, and K. Khazim, "Does Ramadan Fasting Affect Hydration Status and Kidney Function in CKD Patients?" *Annals of nutrition and metabolism*, vol. 72, no. 3, pp. 241–247, 2018.

[54] G. Manjunath, R. Aravindhakshan, and S. Varghese, "Effect of fasting during Ramadan on thermal stress parameters," *Eastern Mediterranean Health Journal*, vol. 25, no. 1, 2019.

[55] M. Born, I. Elmadfa, and F. W. Schmahl, "Auswirkungen eines periodischen Fluessigkeits- und Nahrungsentzuges." *Muencher Medizinische Wochenschrift*, 1979.

[56] N. Sweileh, A. Schnitzler, G. R. Hunter, and B. Davis, "Body composition and energy metabolism in resting and exercising muslims during Ramadan fast." *Journal of Sports Medicine and Physical Fitness*, vol. 32, no. 2, pp. 156–163, Jun. 1992.

[57] S. H. Cheah, S. L. Ch'Ng, R. Husain, and M. T. Duncan, "Effects of fasting during Ramadan on urinary excretion in Malaysian Muslims," *British Journal of Nutrition*, vol. 63, no. 2, pp. 329–337, Mar. 1990.

[58] J. Bourqui and E. C. Fear, "Shielded UWB Sensor for Biomedical Applications," *IEEE Antennas and Wireless Propagation Letters*, vol. 11, pp. 1614–1617, 2012.

[59] L. Rabiner, R. Schafer, and C. Rader, "The chirp z-transform algorithm," *IEEE Transactions on Audio and Electroacoustics*, vol. 17, no. 2, pp. 86–92, Jun. 1969.

[60] J. Bourqui and E. C. Fear, "System for Bulk Dielectric Permittivity Estimation of Breast Tissues at Microwave Frequencies," *IEEE Transactions on Microwave Theory and Techniques*, vol. 64, no. 9, pp. 3001–3009, Sep. 2016.

[61] F. Peronnet, D. Mignault, P. du Souich, S. Vergne, L. Le Bellego, L. Jimenez, and R. Rabasa-Lhoret, "Pharmacokinetic analysis of absorption, distribution and disap-

pearance of ingested water labeled with D2O in humans," *European Journal of Applied Physiology*, vol. 112, no. 6, pp. 2213–2222, Jun. 2012.

[62] H. Minami and R. W. McCallum, "The Physiology and Pathophysiology of Gastric Emptying in Humans," *Gastroenterology*, vol. 86, no. 6, pp. 1592–1610, Jun. 1984.

[63] L. E. Armstrong, A. C. Pumerantz, K. A. Fiala, M. W. Roti, S. A. Kavouras, D. J. Casa, and C. M. Maresh, "Human Hydration Indices: Acute and Longitudinal Reference Values," *International Journal of Sport Nutrition and Exercise Metabolism*, vol. 20, no. 2, pp. 145–153, Apr. 2010.

[64] R. F. Harrington, *Time-Harmonic Electromagnetic Fields*. New York: Wiley-IEEE Press, 2001, vol. 32.

[65] S. Caorsi, M. Pastorino, and M. Raffetto, "Electromagnetic scattering by a multilayer elliptic cylinder under transverse-magnetic illumination: Series solution in terms of Mathieu functions," *IEEE Transactions on Antennas and Propagation*, vol. 45, no. 6, pp. 926–935, Jun. 1997.

[66] W. C. Chew, *Waves and Fields in Inhomogeneous Media*. New York, 1995.

[67] T. M. Grzegorczyk, P. M. Meaney, P. A. Kaufman, R. M. diFlorio-Alexander, and K. D. Paulsen, "Fast 3-D Tomographic Microwave Imaging for Breast Cancer Detection," *IEEE Transactions on Medical Imaging*, vol. 31, no. 8, pp. 1584–1592, Aug. 2012.

[68] M. Pastorino, *Microwave Imaging*. Hoboken, United States: John Wiley & Sons, Incorporated, 2010.

[69] C. Gilmore, A. Zakaria, J. LoVetri, and S. Pistorius, "A study of matching fluid loss in a biomedical microwave tomography system," *Medical Physics*, vol. 40, no. 2, pp. 023 101–1 – 02 310–14, 2013.

[70] M. Ostadrahimi, P. Mojabi, C. Gilmore, A. Zakaria, S. Noghanian, S. Pistorius, and J. LoVetri, "Analysis of Incident Field Modeling and Incident/Scattered Field Calibration Techniques in Microwave Tomography," *IEEE Antennas and Wireless Propagation Letters*, vol. 10, pp. 900–903, 2011.

[71] A. Taflove and S. Hagness, *Computational Electrodynamics: The Finite-Difference Time-Domain Method*, 3rd ed. Norwood, MA: Artech House, 2005.

[72] J.-M. Jin, *The Finite Element Method in Electromagnetics*, 3rd ed. Hoboken, NJ: J. Wiley, 2014.

[73] D. Borup, D. Sullivan, and O. Gandhi, "Comparison of the FFT Conjugate Gradient Method and the Finite-Difference Time-Domain Method for the 2-D Absorption Problem," *IEEE Transactions on Microwave Theory and Techniques*, vol. 35, no. 4, pp. 383–395, Apr. 1987.

[74] W. C. Gibson, *The Method of Moments in Electromagnetics*. Boca Raton, FL: Chapman & Hall/CRC.

[75] R. F. Harrington, *Field Computation by Moment Methods*. Wiley-IEEE Press, 1993.

[76] J. Richmond, "Scattering by a dielectric cylinder of arbitrary cross section shape," *IEEE Transactions on Antennas and Propagation*, vol. 13, no. 3, pp. 334–341, May 1965.

[77] N. N. Bojarski, "K-Space Formulation of the Electromagnetic Scattering Problem," Air Force Avionics Laboratory, Wright-Patterson Air Force Base, Ohio, Tech. Rep., Sep. 1972.

[78] D. Borup and O. Gandhi, "Calculation of High-Resolution SAR Distributions in Biological Bodies Using the FFT Algorithm and Conjugate Gradient Method (Short

Papers)," *IEEE Transactions on Microwave Theory and Techniques*, vol. 33, no. 5, pp. 417–419, May 1985.

[79] H. Jacques, "Sur les problèmes aux derivees partielles et leur significantion physique," *Princeton University Bulletin*, vol. 13, no. 4, Apr. 1902.

[80] C. Gilmore, "Towards an improved microwave tomography system," Ph.D. dissertation, University of Manitoba, Jan. 2010.

[81] O. M. Bucci and T. Isernia, "Electromagnetic inverse scattering: Retrievable information and measurement strategies," *Radio Science*, vol. 32, no. 6, pp. 2123–2137, 1997.

[82] A. I. Nachman, "Global Uniqueness for a Two-Dimensional Inverse Boundary Value Problem," *Annals of Mathematics*, vol. 143, no. 1, pp. 71–96, 1996.

[83] S. Twomey, *Introduction to the Mathematics of Inversion in Remote Sensing and Direct Measurements*, ser. Developments in Geomathematics. Amsterdam: Elsevier, 1977, no. 3.

[84] P. C. Hansen, *Rank-Deficient and Discrete Ill-Posed Problems*, ser. Mathematical Modeling and Computation. Society for Industrial and Applied Mathematics, Jan. 1998.

[85] M. Slaney, A. Kak, and L. Larsen, "Limitations of Imaging with First-Order Diffraction Tomography," *IEEE Transactions on Microwave Theory and Techniques*, vol. 32, no. 8, pp. 860–874, Aug. 1984.

[86] F. Natterer, "An error bound for the Born approximation," *Inverse Problems*, vol. 20, no. 2, pp. 447–452, Jan. 2004.

[87] G. H. Golub, *Matrix Computations.* Baltimore: Johns Hopkins University Press, 2013.

[88] C. R. Harris, K. J. Millman, S. J. van der Walt, R. Gommers, P. Virtanen, D. Cournapeau, E. Wieser, J. Taylor, S. Berg, N. J. Smith, R. Kern, M. Picus, S. Hoyer, M. H. van Kerkwijk, M. Brett, A. Haldane, J. F. del Río, M. Wiebe, P. Peterson, P. Gérard-Marchant, K. Sheppard, T. Reddy, W. Weckesser, H. Abbasi, C. Gohlke, and T. E. Oliphant, "Array programming with NumPy," *Nature*, vol. 585, no. 7825, pp. 357–362, Sep. 2020.

[89] E. Anderson, Z. Bai, C. Bischof, L. S. Blackford, J. Demmel, J. Dongarra, J. Du Croz, A. Greenbaum, S. Hammarling, A. McKenney, and D. Sorensen, *LAPACK Users' Guide*, 3rd ed. Philadelphia, PA: SIAM, 1999.

[90] Y. M. Wang and W. C. Chew, "An iterative solution of the two-dimensional electromagnetic inverse scattering problem," *International Journal of Imaging Systems and Technology*, vol. 1, no. 1, pp. 100–108, 1989.

[91] W. C. Chew and Y. M. Wang, "Reconstruction of two-dimensional permittivity distribution using the distorted Born iterative method," *IEEE Transactions on Medical Imaging*, vol. 9, no. 2, pp. 218–225, Jun. 1990.

[92] P. M. van den Berg and R. E. Kleinman, "A contrast source inversion method," *Inverse Problems*, vol. 13, no. 6, pp. 1607–1620, Dec. 1997.

[93] R. F. Remis and P. M. van den Berg, "On the equivalence of the Newton-Kantorovich and distorted Born methods," *Inverse Problems*, vol. 16, no. 1, pp. L1–L4, Jan. 2000.

[94] T. Rubaek, P. M. Meaney, P. Meincke, and K. D. Paulsen, "Nonlinear Microwave Imaging for Breast-Cancer Screening Using Gauss–Newton's Method and the CGLS Inversion Algorithm," *IEEE Transactions on Antennas and Propagation*, vol. 55, no. 8, pp. 2320–2331, Aug. 2007.

[95] A. Abubakar, T. M. Habashy, V. L. Druskin, L. Knizhnerman, and D. Alumbaugh, "2.5D forward and inverse modeling for interpreting low-frequency electromagnetic measurements," *GEOPHYSICS*, vol. 73, no. 4, pp. F165–F177, Jul. 2008.

[96] P. M. Meaney, E. Demidenko, N. K. Yagnamurthy, D. Li, M. W. Fanning, and K. D. Paulsen, "A two-stage microwave image reconstruction procedure for improved internal feature extraction," *Medical Physics*, vol. 28, no. 11, pp. 2358–2369, 2001.

[97] M. Haynes, J. Stang, and M. Moghaddam, "Real-time Microwave Imaging of Differential Temperature for Thermal Therapy Monitoring," *IEEE Transactions on Biomedical Engineering*, vol. 61, no. 6, pp. 1787–1797, Jun. 2014.

[98] A. N. Tikhonov and V. A. Arsenin, *Solutions of Ill-Posed Problems*. New York, NY, USA: J. Wiley, 1977.

[99] S. Twomey, "On the Numerical Solution of Fredholm Integral Equations of the First Kind by the Inversion of the Linear System Produced by Quadrature," *Journal of the ACM*, vol. 10, no. 1, pp. 97–101, Jan. 1963.

[100] P. Mojabi and J. LoVetri, "Overview and Classification of Some Regularization Techniques for the Gauss-Newton Inversion Method Applied to Inverse Scattering Problems," *IEEE Transactions on Antennas and Propagation*, vol. 57, no. 9, pp. 2658–2665, Sep. 2009.

[101] K. Levenberg, "A Method for the Solution of Certain Non-Linear Problems in Least Squares," *Quarterly of applied mathematics*, vol. 2, no. 2, pp. 164–168, 1944.

[102] D. W. Marquardt, "An Algorithm for Least-Squares Estimation of Nonlinear Parameters," *Journal of the Society for Industrial and Applied Mathematics*, vol. 11, no. 2, pp. 431–441, Jun. 1963.

[103] A. Franchois and C. Pichot, "Microwave imaging-complex permittivity reconstruction with a Levenberg-Marquardt method," *IEEE Transactions on Antennas and Propagation*, vol. 45, no. 2, pp. 203–215, Feb. 1997.

[104] A. H. Golnabi, P. M. Meaney, S. D. Geimer, and K. D. Paulsen, "Comparison of no-prior and soft-prior regularization in biomedical microwave imaging," *Journal of Medical Physics*, vol. 36, no. 3, pp. 159–170, 2011.

[105] N. Joachimowicz, J. Mallorqui, J.-C. Bolomey, and A. Broquets, "Convergence and stability assessment of Newton-Kantorovich reconstruction algorithms for microwave tomography," *IEEE Transactions on Medical Imaging*, vol. 17, no. 4, pp. 562–570, Aug. 1998.

[106] P. M. van den Berg, A. L. van Broekhoven, and A. Abubakar, "Extended contrast source inversion," *Inverse Problems*, vol. 15, no. 5, pp. 1325–1344, Oct. 1999.

[107] V. A. Morozov, *Methods for Solving Incorrectly Posed Problems*. New York: Springer, 1984.

[108] G. H. Golub, M. Heath, and G. Wahba, "Generalized Cross-Validation as a Method for Choosing a Good Ridge Parameter," *Technometrics*, vol. 21, no. 2, pp. 215–223, May 1979.

[109] P. C. Hansen and D. P. O'Leary, "The Use of the L-Curve in the Regularization of Discrete Ill-Posed Problems," *SIAM Journal on Scientific Computing*, vol. 14, no. 6, pp. 1487–1503, Nov. 1993.

[110] D. Calvetti, P. C. Hansen, and L. Reichel, "L-Curve Curvature via Lanczos Bidiagonalization," p. 16.

[111] A. B. Bakushinskii, "The problem of the convergence of the iteratively regularized Gauss-Newton method," *The problem of the convergence of the iteratively regularized Gauss-Newton method*, vol. 32, no. 9, pp. 1353–1359, 1992.

[112] M.-C. Gosselin, E. Neufeld, H. Moser, E. Huber, S. Farcito, L. Gerber, M. Jedensjö, I. Hilber, F. D. Gennaro, B. Lloyd, E. Cherubini, D. Szczerba, W. Kainz, and N. Kuster, "Development of a new generation of high-resolution anatomical models for medical device evaluation: The Virtual Population 3.0," *Physics in Medicine and Biology*, vol. 59, no. 18, pp. 5287–5303, Aug. 2014.

[113] C. Gilmore, P. Mojabi, A. Zakaria, M. Ostadrahimi, C. Kaye, S. Noghanian, L. Shafai, S. Pistorius, and J. LoVetri, "A Wideband Microwave Tomography System With a Novel Frequency Selection Procedure," *IEEE Transactions on Biomedical Engineering*, vol. 57, no. 4, pp. 894–904, Apr. 2010.

[114] A. Polymeris, P. D. Papapetrou, and G. Katsoulis, "An Average Body Circumference Can Be a Substitute for Body Mass Index in Women," *Advances in Medicine*, vol. 2014, Nov. 2014.

[115] P. M. Meaney, C. J. Fox, S. D. Geimer, and K. D. Paulsen, "Electrical Characterization of Glycerin: Water Mixtures: Implications for Use as a Coupling Medium in Microwave Tomography," *IEEE Transactions on Microwave Theory and Techniques*, vol. 65, no. 5, pp. 1471–1478, May 2017.

[116] T. J. Cui, W. C. Chew, X. X. Yin, and W. Hong, "Study of resolution and super resolution in electromagnetic imaging for half-space problems," *IEEE Transactions on Antennas and Propagation*, vol. 52, no. 6, pp. 1398–1411, Jun. 2004.

[117] C. Gilmore, P. Mojabi, A. Zakaria, S. Pistorius, and J. LoVetri, "On Super-Resolution With an Experimental Microwave Tomography System," *IEEE Antennas and Wireless Propagation Letters*, vol. 9, pp. 393–396, 2010.

[118] O. Bucci and G. Franceschetti, "On the spatial bandwidth of scattered fields," *IEEE Transactions on Antennas and Propagation*, vol. 35, no. 12, pp. 1445–1455, Dec. 1987.

[119] O. M. Bucci and T. Isernia, "Electromagnetic inverse scattering: Retrievable information and measurement strategies," *Radio Science*, vol. 32, no. 6, pp. 2123–2137, 1997.

[120] N. K. Nikolova, *Introduction to Microwave Imaging*, ser. EuMA High Frequency Technologies Series. Cambridge: University Press, 2017.

[121] A. Likas, N. Vlassis, and J. J. Verbeek, "The global k-means clustering algorithm," *Pattern Recognition*, vol. 36, no. 2, pp. 451–461, Feb. 2003.

[122] S. Gabriel, R. W. Lau, and C. Gabriel, "The dielectric properties of biological tissues: III. Parametric models for the dielectric spectrum of tissues," *Physics in Medicine and Biology*, vol. 41, no. 11, pp. 2271–2293, Nov. 1996.

[123] M. Lazebnik, M. Okoniewski, J. H. Booske, and S. C. Hagness, "Highly Accurate Debye Models for Normal and Malignant Breast Tissue Dielectric Properties at Microwave Frequencies," *IEEE Microwave and Wireless Components Letters*, vol. 17, no. 12, pp. 822–824, Dec. 2007.

[124] D. W. Winters, E. J. Bond, B. D. V. Veen, and S. C. Hagness, "Estimation of the Frequency-Dependent Average Dielectric Properties of Breast Tissue Using a Time-Domain Inverse Scattering Technique," *IEEE Transactions on Antennas and Propagation*, vol. 54, no. 11, p. 12, 2006.

[125] W. C. Chew and J. H. Lin, "A frequency-hopping approach for microwave imaging of large inhomogeneous bodies," *IEEE Microwave and Guided Wave Letters*, vol. 5, no. 12, pp. 439–441, Dec. 1995.

[126] A. Bakkali, C. Buisson, L. Mounien, J. F. Landrier, V. Tishkova, and a. P. Sabouroux, "First Microwave Tomography Approach Towards a Truly Noninvasive, Pain-Free and Wearable Blood Glucose Monitoring Device," *Progress In Electromagnetics Research M*, vol. 102, pp. 193–206, 2021.

[127] P. Zwamborn and P. M. van den Berg, "The three dimensional weak form of the conjugate gradient FFT method for solving scattering problems," *IEEE Transactions on Microwave Theory and Techniques*, vol. 40, no. 9, pp. 1757–1766, Sep. 1992.

[128] T. Sarkar, K. Siarkiewicz, and R. Stratton, "Survey of numerical methods for solution of large systems of linear equations for electromagnetic field problems," *IEEE Transactions on Antennas and Propagation*, vol. 29, no. 6, pp. 847–856, Nov. 1981.

[129] C. A. Balanis, *Advanced Engineering Electromagnetics*. New York: Wiley, 1989.

Appendix A

Fast Fourier Transform - Conjugate Gradient Method

The fast Fourier transform conjugate gradient method (FFT-CGM) algorithm for 2D scattering can be found in [73, 78]. The details found therein are clarified here.

The total field can be found from eq. (4.14), repeated here for convenience:

$$E^i_{ij} = E_{ij} + \frac{jk_b^2}{4} \sum_{m=1}^{N_y} \sum_{n=1}^{N_x} \chi_{nm} E_{nm} \cdot \iint_{\mathcal{D}_{nm}} H_0^{(2)}(k_b|r_{ij} - r|)dr$$

For a regular grid, the Green's function can be written as a function of the difference between cell locations:

$$K(r_{ij} - r_{nm}) = K_{ij,nm} = \frac{jk_b^2}{4} \iint_{\mathcal{D}_{nm}} H_0^{(2)}(k_b|r_{ij} - r|)dr \tag{A.1}$$

The total field equation can be written in terms of a linear operator $\boldsymbol{A}$:

$$\boldsymbol{e}^i = \boldsymbol{A}\boldsymbol{e} = e_{ij} + \sum_m \sum_n e_{nm}\chi_{nm}K_{ij,nm} \tag{A.2}$$

with a Hermitian operator defined as:

$$\boldsymbol{A}^H \boldsymbol{e} = e_{ij} + \chi^*_{nm} \sum_m \sum_n e_{nm} K^*_{ij,nm} \tag{A.3}$$

Where $(\cdot)^*$ denotes the complex conjugate.

The Hermitian operator can be verified numerically using the well known identity:

$$\langle \boldsymbol{A}\boldsymbol{x}, \boldsymbol{y} \rangle = \langle \boldsymbol{x}, \boldsymbol{A}^H \boldsymbol{y} \rangle \tag{A.4}$$

Where $\langle \cdot, \cdot \rangle$ is the typical inner product for complex vectors.

The summations in eqs. (A.2), (A.3) can be efficiently calculated by replacing them with convolutions and evaluating using the FFT. Note that if $\boldsymbol{e}$ is an $N \times N$ image the kernel will be of size $N^2 \times N^2$. To avoid aliasing in the convolution the image should be zero padded to at least $2N + 1 \times 2N + 1$ [127].

The conjugate gradient method solution for $\boldsymbol{A}\boldsymbol{x} = \boldsymbol{b}$ can be found step as:

$$\boldsymbol{r}_0 = \boldsymbol{A}\boldsymbol{x}_0 - \boldsymbol{y}$$

$$\boldsymbol{p}_0 = -\boldsymbol{A}^H \boldsymbol{r}_0$$

$$t_k = \frac{\left\| \boldsymbol{A}^H \boldsymbol{r}_k \right\|^2}{\left\| \boldsymbol{A}\boldsymbol{p}_k \right\|^2}$$

$$\boldsymbol{x}_{k+1} = \boldsymbol{x}_k + t_k \boldsymbol{p}_k$$

$$\boldsymbol{r}_{k+1} = \boldsymbol{r}_k + t_k \boldsymbol{A}\boldsymbol{p}_k$$

$$q_k = \frac{\left\| \boldsymbol{A}^H \boldsymbol{r}_{k+1} \right\|^2}{\left\| \boldsymbol{A}^H \boldsymbol{r}_k \right\|^2}$$

$$\boldsymbol{p}_{k+1} = -\boldsymbol{A}^H \boldsymbol{r}_{k+1} + q_k \boldsymbol{p}_k$$

The initial field values $\boldsymbol{x}_0$ can be set to $\boldsymbol{0}$ or the incident field values. $\boldsymbol{r}_k$ and $\boldsymbol{p}_k$ are the residuals and step direction at each iteration, respectively. Applying the linear operator

and its Hermitian is done using the FFT for every step. Once residuals reach a predefined threshold the iterations are terminated. The technique can be expected to converge in a finite number of steps. In [78], there is a typographical error in the last step of the CGM where the r_{k+1} is dropped for r_k. The above CGM algorithm can be found in [128].

Appendix B

Scattered Field from a Dielectric Cylinder

Harrington outlines the derivation for the scattered fields from a PEC cylinder due to both plane waves and line sources in [64]. The extension to a cylinder with arbitrary dielectric properties due to a plane wave is provided in problem 5-34. Based on this solution and ideas outlined in the chapter on cylindrical waves, the scattered fields for a line source are derived here.

Let the background medium have properties $\varepsilon_r = \varepsilon_{r,b}$, $\mu_r = 1$ and wavenumber k_b and the dielectric cylinder properties $\varepsilon_r = \varepsilon_{r,d}$, $\mu_r = 1$ and wavenumber k_d.

The incident field is given by eq. (4.6). This represents a cylindrical wave propagating from the transmitter location. This field can be written in terms of cylindrical waves centered at the origin as:

$$E^i = \frac{-\omega\mu_0 I}{4} \sum_{n=-\infty}^{\infty} H_n^{(2)}(k_b\rho_{tx}) J_n(k_b\rho) e^{jn(\phi-\phi_{tx})} \tag{B.1}$$

Where $\rho = |\boldsymbol{r}|$, $\phi = \angle \boldsymbol{r}$ and $\rho < \rho_{tx}$.

The scattered field outside the cylinder is an outward travelling wave so can be written, within some set of constants determined by the boundary value problem a_n, as:

$$E^s = \frac{-\omega\mu_0 I}{4} \sum_{n=-\infty}^{\infty} a_n H_n^{(2)}(k_b\rho_{tx}) H_n^{(2)}(k_b\rho) e^{jn(\phi-\phi_{tx})} \tag{B.2}$$

So the total field outside the cylinder is:

$$E_{\text{ext}} = \frac{-\omega\mu_0 I}{4} \sum_{n=-\infty}^{\infty} H_n^{(2)}(k_b\rho_{tx}) \left[J_n(k_b\rho) + a_n H_n^{(2)}(k_b\rho)\right] e^{jn(\phi-\phi_{tx})} \tag{B.3}$$

In addition to the total field outside the cylinder, the field inside the cylinder can be found. Using the fact that the fields at the interface and at the center of the cylinder are finite, the total fields inside the cylinder have the form:

$$E_{\text{int}} = \frac{-\omega\mu_0 I}{4} \sum_{n=-\infty}^{\infty} b_n H_n^{(2)}(k_b\rho_{tx}) J_n(k_d\rho) e^{jn(\phi-\phi_{tx})} \tag{B.4}$$

The magnetic field (H-field) can be found by applying applying Faraday's Law [129]:

$$\boldsymbol{H} = -\frac{1}{j\omega\mu_0}\nabla \times \boldsymbol{E} = -\frac{1}{j\omega\mu_0}\left(\frac{1}{\rho}\frac{\partial E_z}{\partial \phi}\hat{a}_\rho - \frac{\partial E_z}{\partial \rho}\hat{a}_\phi\right) \tag{B.5}$$

Eq. (B.5) can be applied to eqs. (B.3) and (B.4) to find the H-field inside and outside of the cylinder. Only the H_ϕ component is required to solve the boundary value problem as it will be tangential to the cylinder boundary.

$$H_{\phi,\text{ext}} = jIk_b \sum_{n=-\infty}^{\infty} H_n^{(2)}(k_b\rho_{tx})[J_n'(k_b\rho) + a_n H_n^{(2)'}(k_b\rho)] e^{jn(\phi-\phi_{tx})} \tag{B.6}$$

$$H_{\phi,\text{int}} = jIk_d \sum_{n=-\infty}^{\infty} b_n H_n^{(2)}(k_b\rho_{tx}) J_n'(k_d\rho) e^{jn(\phi-\phi_{tx})} \tag{B.7}$$

Where the derivatives are with respect to the argument $k\rho$.

The derivatives can be calculated using the well-known recurrence formula which is defined for any arbitrary Bessel function $B_n(x)$:

$$B_n'(x) = \begin{cases} B_{n-1}(x) - \frac{n}{x}B_n(x), & \text{if } n \neq 0 \\ -B_1(x), & \text{if } n = 0 \end{cases} \tag{B.8}$$

Next, the boundary conditions can be applied. First, the tangential component of the E-field must be continuous across the boundary so setting eqs. (B.3) (B.4) equal at $\rho = a$ yields:

$$b_n = \frac{1}{J_n(k_d a)}\left[J_n(k_b a) + a_n H_n^{(2)}(k_b a)\right] \tag{B.9}$$

The tangential component of the H-field must also be continuous across the boundary so setting eqs. (B.6) (B.7) equal at $\rho = a$ yields:

$$a_n = -\frac{J_n(k_b a)}{H_n^{(2)}(k_b a)} \frac{\sqrt{\frac{\varepsilon_{r,d}}{\varepsilon_{r,b}}} J_n'(k_d \rho)/J_n(k_d a) - J_n'(k_b \rho)/J_n(k_b a)}{\sqrt{\frac{\varepsilon_{r,d}}{\varepsilon_{r,b}}} J_n'(k_d \rho)/J_n(k_d a) - H_n^{(2)'}(k_b \rho)/H_n^{(2)}(k_b a)} \tag{B.10}$$

The solution for scattering from a PEC cylinder can be found by letting $\varepsilon_d \to \infty$ in eq. (B.10) which then reduces to the equation provided in [64].

$$a_n = -\frac{J_n(k_b a)}{H_n^{(2)}(k_b a)} \tag{B.11}$$

In practice, the summation over Bessel orders must be finite. It is straightforward to run the summation with various limits to see the marginal impact of increasing the number of orders. In this work the summation was done from 100 to -100.

Appendix C

Forearm Image Segmentation

The complete details of the forearm segmentation technique and examples of its application are provided here.

Consider the permittivity image $\varepsilon_r(x, y)$ the image is sharpened using the kernel:

$$K = \begin{bmatrix} 0 & -1 & 0 \\ -1 & 5 & -1 \\ 0 & -1 & 0 \end{bmatrix} \tag{C.1}$$

which computes the Laplacian $(\nabla^2 \cdot \varepsilon_r(x, y))$ and adds it the image. This sharpened image is then squared to further accentuate the forearm.

The image is then thresholded to produce the segmented image. Pixels above the threshold are set to 1 and pixels below are set to 0. Unless otherwise specified the threshold is set to the mean of the sharpened image. The edges of the images are set to zero as there are some artifacts in the raw images that are not thresholded properly. This is valid if the forearm is in the middle of the reconstructed image which should be the case in simulation and in practice.

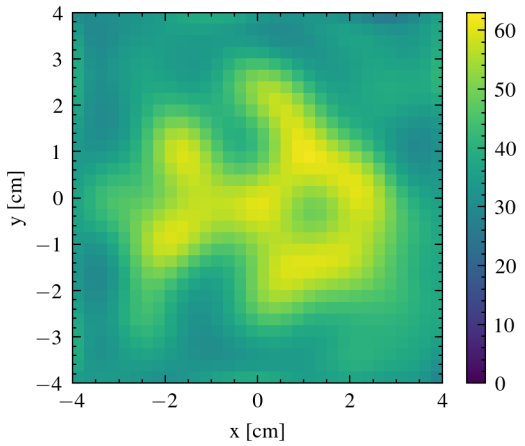

(a) Relative permittivity.

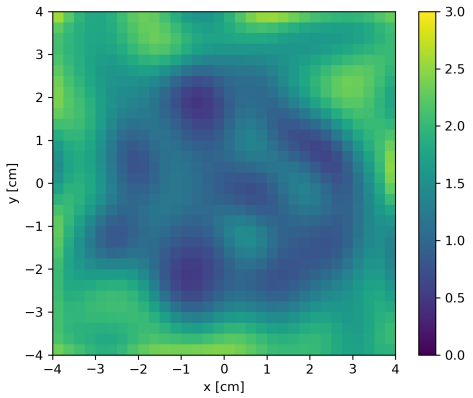

(b) Conductivity.

Figure C.1: Reconstructed Duke forearm model with optimized design and 10% noise.

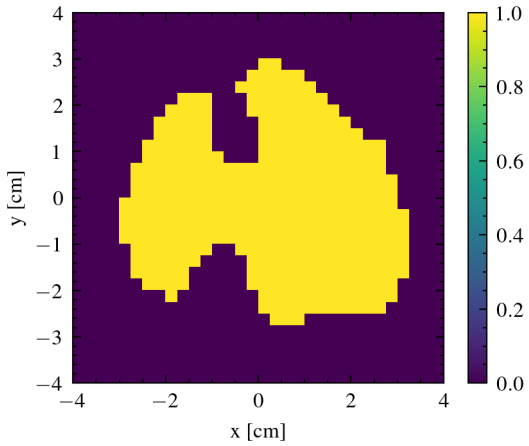

Figure C.2: Segmented image for Duke forearm in optimized design and 10% noise.

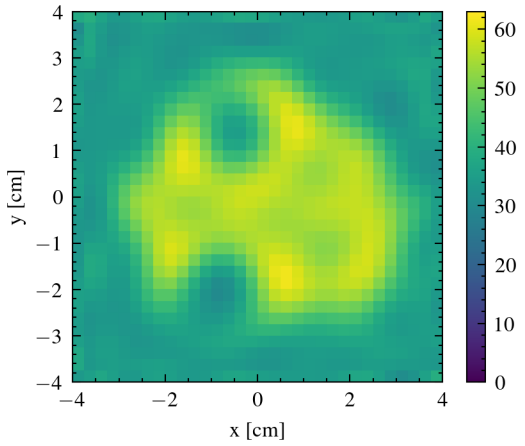

(a) Relative permittivity.

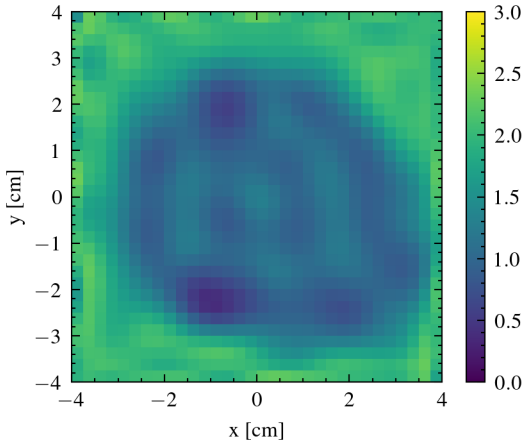

(b) Conductivity.

Figure C.3: Reconstructed Duke forearm model with $N_{rx} = 32$ and 5% noise.

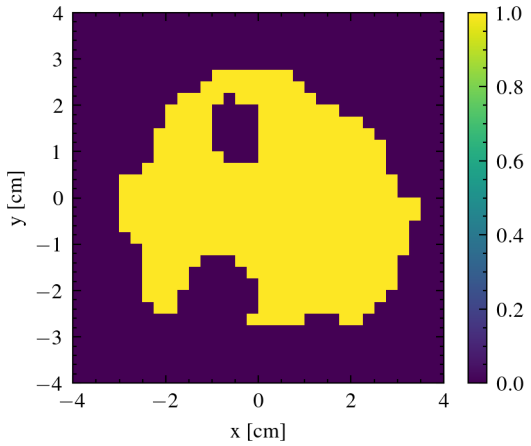

Figure C.4: Segmented image for Duke forearm in $N_{rx} = 32$ and 5% noise.